Relativistic Matter Under Extreme Conditions

by

Xinyang Wang

A Dissertation Presented in Partial Fulfillment
of the Requirements for the Degree
Doctor of Philosophy

Approved July 2013 by the
Graduate Supervisory Committee:

Igor Shovkovy, Chair
Andrei Belitsky
Damien Easson
Xihong Peng
Tanmay Vachaspati

ARIZONA STATE UNIVERSITY

August 2013

ABSTRACT

In this thesis, we present the study of several physical properties of relativistic matters under extreme conditions. We start by deriving the rate of the nonleptonic weak processes and the bulk viscosity in several spin-one color superconducting phases of quark matter. We also calculate the bulk viscosity in the nonlinear and anharmonic regime in the normal phase of strange quark matter. We point out several qualitative effects due to the anharmonicity, although quantitatively they appear to be relatively small. In the corresponding study, we take into account the interplay between the nonleptonic and semileptonic weak processes. The results can be important in order to relate accessible observables of compact stars to their internal composition. We also use quantum field theoretical methods to study the transport properties in monolayer graphene in a strong magnetic field. The corresponding quasi-relativistic system reveals an anomalous quantum Hall effect, whose features are directly connected with the spontaneous flavor symmetry breaking. We study the microscopic origin of Faraday rotation and magneto-optical transmission in graphene and show that their main features are in agreement with the experimental data.

I would like to dedicate this thesis to the memory of my grandfather who passed away 4 years ago. If there is heaven, I hope he can see me getting my Ph.D degree which he expected to see.

TABLE OF CONTENTS

LIST OF TABLES

LIST OF FIGURES

CHAPTER 1

INTRODUCTION

Three of the most important theories in early 20th century physics are electrodynamics, relativity and quantum mechanics. Quantum field theory (QFT) was constructed from combining the key ideas of these theories. At the beginning, the objective of QFT was to study the elementary particle physics, but later, it found many applications to many other fields of physics (e.g., nuclear, atomic and condensed matter physics).

In this thesis, we use the methods of QFT to investigate the properties and dynamics of relativistic matter. By definition, relativistic matter is composed of relativistic particles, i.e., particles whose momenta p are greater than, or comparable to mc (here, m is the mass of the particle). Examples of relativistic matter include electron plasma inside compact stars, nuclear matter in the interior of neutron stars, quark-gluon plasma that existed in the Early Universe and can be created in heavy ion collisions, and possible quark matter inside the inner most parts of compact stars. Another interesting example of a quasi-relativistic matter is found in graphene, whose quasiparticles are Dirac fermions with zero rest mass.

Very often relativistic matter is subject to extreme environments, such as very high temperature, high density and/or the presence of strong external fields. It is of interest, therefore, to study such matter in order to understand its implications on the physical properties of compact starts, the Early Universe and other systems. The corresponding investigations can also improve and enrich our understanding of other fields of physics (e.g., astrophysics, condense matter and atomic physics).

In the rest of this thesis, we will discuss several physics properties of a few kinds of relativistic matter under extreme conditions (i.e., high magnetic fields or high density). For convenience, we use the units with $k_B = c = \hbar = 1$.

1

1.1 Neutron stars

As we know, the interior of neutron stars have the highest density in the Universe (except for the black holes). The corresponding state of matter is necessarily in the relativistic regime. Here we give a brief introduction to such stars.

Neutron stars are compact stellar objects that originate from supernova explosions. They were theoretically predicted by Landau in 1932 after the discovery of the neutron. In 1934, Baade and Zwicky suggested that the supernova process was the result of the transition from a normal star to a neutron star. Later in 1939, Zwicky pointed out that the energy release in supernova is comparable to the gravitational potential energy change due to the stellar collapse from its original size (radius $\approx 10^6$ km) down to the size of a neutron star (radius ≈ 10 km). The first pulsar was observed on November 28, 1967 by Jocelyn Bell Burnell and Antony Hewish [1, 2].[1] By the end of 1968, over 100 pulsar articles were published. There were strong arguments that the pulsar is either a white dwarf, or an oscillating neutron star. It was Gold's idea that pulsars are rotating magnetized neutron stars that eventually prevailed [3]. In 1969, the discovery of the Crab pulsar gave important evidence. The spin period of Crab pulsar is 33 ms, which is too short to be the rotation period of a white dwarf.

While the structure of the outer layers of neutron stars are understood to a certain degree, the inner cores are a great puzzle. This is directly related to the gaps in the current knowledge regarding the equation of state of QCD at the densities of relevance.

In literature, there exist numerous models of the equation of state. By making use of such models, the internal structure of neutron stars can be theoretically predicted by considering the condition of hydrostatic equilibrium. This is equivalent to solving

---

[1] Hewish was awarded the Nobel Prize in physics in 1974. Bell, who made the initial discovery while she was Hewish's Ph.D student, was not.

the Tolman-Oppenheimer-Volkov (TOV) equations [4, 5], i.e.,

$$\frac{dp}{dr} = -\frac{G\varepsilon(r)\mathcal{M}(r)}{c^2 r^2}\left[1 + \frac{p(r)}{\varepsilon(r)}\right]\left[1 + \frac{4\pi r^3 p(r)}{\mathcal{M}(r)c^2}\right]\left[1 - \frac{2G\mathcal{M}(r)}{c^2 r}\right]^{-1} , \quad (1.1)$$

$$\frac{d\mathcal{M}}{dr} = 4\pi r^2 \rho(r) = \frac{4\pi r^2 \varepsilon(r)}{c^2}, \quad (1.2)$$

$$\mathcal{M}(r) = 4\pi \int_0^r r'^2 dr' \rho(r') = 4\pi \int_0^r r'^2 dr' \varepsilon(r')/c^2 . \quad (1.3)$$

Here, $G = 6.673 \times 10^{-8}$ dyne $\cdot$ cm^2/g^2 is Newton's gravitational constant, $\rho(r)$ and

$p(r)$ are the mass density and pressure at the distance r from the center of the star, and

ε is the corresponding energy density. The quantity $\mathcal{M}(r)$ is the total mass inside the

sphere of radius r.

The solutions to the TOV equations for commonly used model equations of

state show that neutron stars have typical radii of about a dozen kilometers and the

maximum values of the masses ranging from about $1.5M_\odot$ to $2.5M_\odot$ [6], where $M_\odot$ is

the Solar mass. The density of matter increases from the surface to the center of the

star. The values of the density at the inner cores can be as high as 5 to 10 times the

normal nuclear density. The temperatures of (proto-)neutron stars are around 10 MeV

when they are just created. After the deleptonization process, the stars cool down and

their temperatures drop below 1 MeV in a matter of a day, and then several orders of

magnitude over the next million years. Therefore, it is possible that the central regions

of old neutron stars are dense and sufficiently cold to support color superconductivity.

Magnetars are a special class of stars. A magnetar is a type of a neutron star with

an extremely strong magnetic field, which emits high-energy electromagnetic radiation

(i.e., X-rays and gamma rays). The rotation periods of magnetars (period $\sim$ 1 - 10 s)

are generally larger than those of other neutron stars. They are the stellar objects with

the strongest magnetic fields in the Universe. The surface magnetic fields of the stars

can reach up to about 10^{15} Gauss [7, 8]. The strong fields of magnetars come as a

result of a magnetohydrodynamic dynamo mechanism inside turbulent hot plasma of a

collapsing star [9, 10]. This can be compared with the magnetic field of the Sun's core, which is around 10^2 Gauss (the field on the surface of the Sun is much smaller and is about a few Gauss). The big difference in the magnetic field of the Sun and a neutron star can be understood by doing a simple toy model calculation. The magnetic field of a neutron star originates from the seed field of the collapsing core of a progenitor star. Because of its high conductivity, the magnetic flux ϕ_B is conserved during the collapse. Then the magnetic field of a newly created neutron star can be estimated by

$$B_{\text{new}} = B_\odot \frac{r_\odot^2}{r_{\text{new}}^2},\qquad(1.4)$$

where $r_\odot$ and r_{new} are the radii of the Sun and a neutron star, respectively, and $B_\odot$ is the magnetic field of the solar core. This corresponds to fields in a range from about 10^9 to about 10^{12} Gauss, which are typical for normal neutron stars. In order to get the fields as large as in magnetars, an additional enhancement is necessary. It can be provided, for example, by the dynamo mechanism mentioned above [9, 10].

1.2   Color superconductivity

As mentioned in Sec. 1.1, the interior of neutron stars are made of very dense matter. The knowledge regarding the actual states of such dense matter is incomplete. One of the common hypotheses states that the densest regions inside neutron stars are made of quark matter, which may even be a color superconductor. So, what is a color superconductor? In this section we will discuss the subtleties of color superconductivity.

1.2.1   Superconductivity

The concept of color superconductivity is analogous to usual superconductivity in solid states physics. It is natural, therefore, to start our discussion in this subsection by introducing the key ideas of ordinary superconductivity.

In 1911 Heike Kamerlingh Onnes was using the earlier discovered liquid helium as a refrigerant to measure the resistance of solid mercury at cryogenic temper-

atures [11]. He observed that the resistance disappeared when the temperature was below 4.3 Kelvin. This phenomenon was called superconductivity. Later, superconductivity was found in other materials. In 1913, lead was found to superconduct below 7 K, and in 1941 niobium nitride was found to be superconducting below 16 K. The Bardeen-Cooper-Schrieffer (BCS) theory [12] gave a successful explanation of superconductivity in 1957. But for a long time, the critical temperature of superconductors remained very low ($T_c < 30$ K). In 1986, the first high-T_c superconductor was found by Bednorz and Müller [13, 14], who succeeded in inducing superconductivity in a barium lanthanum copper oxide (BaLaCuO, also known as LBCO). The oxide's critical temperature was 35 K, which was 12 K higher than the previous record [13, 14]. Later, thousands of high-temperature superconductors have been found. Currently, the highest temperature superconductors are made of a ceramic material consisting of thallium, mercury, copper, barium, calcium, strontium and oxygen, with $T_c = 138$ K. Also, we should mention that the critical temperature of $HgBa_2Ca_2Cu_3O_{8+\delta}$ (Hg-1223) can increase to 150 K under high pressure. This shows that the critical temperature is very sensitive to the structure of a compound [15]. One of the most important properties of the high T_c superconductors is the value of their critical temperature being above the boiling point of liquid nitrogen. Unfortunately we still could not find a successful theoretical explanation of high T_c superconductivity.

In general, a superconductor is a material that is characterized by the following properties: (1) vanishingly small electrical resistance; (2) the expulsion of the magnetic field (known as the Meissner-Ochsenfeld effect [16]); (3) the discontinuity of the electronic specific heat at T_c, which increases at T_c and vanishes exponentially near $T = 0$.

In most cases, superconductivity appears only when the temperature T is below the critical temperature T_c and the magnetic field H is smaller than the critical magnetic

5
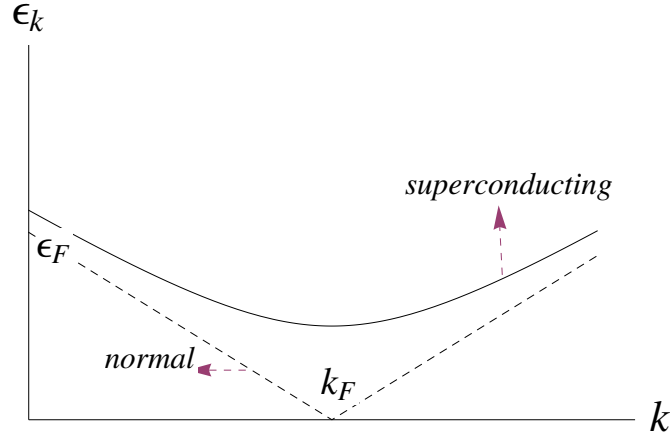
Figure 1.1: Fermionic quasiparticle dispersion relations in the normal and supercon-ducting phases, i.e., $\varepsilon_k = \sqrt{(\varepsilon_{0,k} - \mu)^2 + \phi^2}$ with $\phi = 0$ in the normal phase (dashed line) and $\phi \neq 0$ in the superconducting phase (solid line).

field H_c. The values of the critical temperature and magnetic field vary from material to material.

Superconductivity in metals or alloys is a quantum property of the many-body electron system. Electrons themselves interact repulsively with each other because of the Coulomb force. In the normal phase (i.e., without superconductivity), the electrons occupy all states within the Fermi sphere, but do not behave coherently. The lowest energy excitations in such a state have arbitrarily small energies. In a superconducting phase, the electrons well below the Fermi surface are nearly the same as in the normal phase. As for the electrons in the vicinity of the Fermi surface, they tend to form the so-called Cooper pairs, i.e., pairs of electrons with opposite momenta and spins. Each Cooper pair has spin $S = 0$ and angular momentum $L = 0$. Such pairs become possible because of the phonon attractive interaction that may dominate over the screened repul-sive Coulomb interaction [17]. Also, when the electrons form Cooper pairs, the Fermi sphere becomes unstable. The ground state of a superconductor will be composed of the state of Cooper pairs, and the distribution of electrons will be no longer the normal

Fermi distribution. The corresponding state has an energy gap in its spectrum of quasi-particle excitations, see Fig. 1.1, and is superconducting. The energy of the gap E_{gap} equals 2ϕ, which is the energy needed to break a single Cooper pair into the electron type quasiparticles.

The value of the gap parameter ϕ is an important characteristics of a supercon-ductor. It is usually found by using a variational approach. The corresponding equation for ϕ is called the gap equation. The gap equation in the BCS theory reads

$$1 = g \int \frac{d^3\mathbf{k}}{(2\pi)^3} \frac{1}{2\varepsilon_k} \tanh\left(\frac{\varepsilon_k}{2T}\right) , \qquad (1.5)$$

where, by definition, $\varepsilon_k = \sqrt{(\varepsilon_{0,k} - \mu)^2 + \phi^2}$ is the quasiparticle excitation energy, see Fig 1.1, $\varepsilon_{0,k}$ is the single particle energy, μ is the chemical potential, and T is the temperature. The coupling constant of the attractive electron-electron interaction is given by g.

In Eq. (1.5) we assume that the interaction is a constant when electrons are around the Fermi surface, and is zero when electrons are elsewhere in the momentum space. The BCS solution to the gap equation is given by the following approximate relation:

$$\phi(0) = 2\omega_D \exp\left(-\frac{1}{N(E_f)g}\right) , \tag{1.6}$$

where ω_D is the Debye frequency that limits the maximum phonon energy and $N(E_f)$ is the density of states at the Fermi surface. As seen from Eq. (1.6), the value of the gap grows with increasing $N(E_f)$ and g. This is expected because the attraction between the electrons gets stronger. One of the predictions of the BCS theory that follows from the above gap equation is as follows: the energy gap at $T = 0$ K is proportional to the critical temperature T_c, namely $2\phi(0) = 3.53T_c$, where the constant of proportionality is unambiguously given by the BCS theory. This relation also agrees well with the experimental data, the fact that together with other numerous predictions strongly supports the validity of the BSC theory of low temperature superconductivity.

The following remark is in order here. Because of a very weak attractive force between electrons, the Cooper pair does not resemble a bound state of two electrons localized in coordinate space. To elaborate on this, let us use the Heisenberg's uncertainty principle to estimate the spatial size of a Cooper pair (denoted by ξ below). Let the uncertainty in the electron's momentum be $\triangle p \simeq 1/\xi$, then the uncertainty in the kinetic energy of the electron inside a Cooper pair is

$$\triangle\left(\frac{p^2}{2m}\right) \simeq \frac{p}{m}\triangle p \simeq \frac{p_F}{m\xi} \tag{1.7}$$

The two electrons are paired if the uncertainty in their kinetic energy is comparable or less than the binding energy, which is of order $\phi(0)$. This translates into

$$\xi \gtrsim \frac{p_F}{\phi(0)m} \equiv \xi_0 \tag{1.8}$$
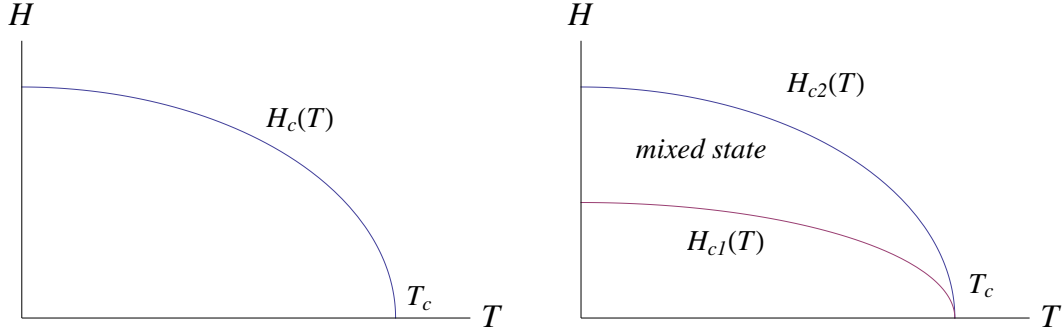
Figure 1.2: Critical magnetic field as a function of temperature for type I superconductors and type II superconductors.

where ξ_0 is called the coherent length. We can estimate that $\xi_0 \simeq 10^{-4}$ cm in a typical low temperature superconductor. This estimate shows that the Cooper pairs are very large compared to the average distance between atoms (as well as electrons) in a metal or an alloy. In other words, there exist many electrons within the typical spatial size of a Cooper pair. Therefore, such a pair cannot be interpreted as a "usual" bound state localized in coordinate space. Instead, it is localized in the reciprocal (momentum) space.

All superconductors are divided into two different types that are determined by the value of the Ginzburg-Landau parameter [18],

$$\kappa \equiv \frac{\lambda_H}{\xi_0}, \tag{1.9}$$

where λ_H is the magnetic field penetration depth. The type I superconductors correspond to $\kappa < \kappa_0 \equiv 1/\sqrt{2}$, while the type II superconductors correspond to $\kappa > \kappa_0$. The type I superconductors, also called "soft" superconductors, are mainly comprised of metals and metalloids that show some conductivity at room temperature. They require very low temperatures in order to slow down molecular vibrations sufficiently to facilitate unimpeded electron flow in accordance with the BCS theory. The type II superconductors are also known as "hard" superconductors. They are comprised of metallic

compounds and alloys. All high-T_c superconductors belong to this type [19, 20, 21]. Magnetic properties also distinguish these two types of superconductors. As shown in figure 1.2, type I superconductors have only one critical magnetic field. When the exterior magnetic field H is less than the critical magnetic field H_c, the Meissner effect is observed and the interior magnetic field vanishes. However, type II superconductors have two critical magnetic fields. Interior magnetic field vanishes when $H < H_{c1}$ and penetrates the system when H is changing in the range from H_{c1} to H_{c2}. The supercon-ducting state transits to a normal state after H reaches H_{c2}.

1.2.2   Helium-3 superfluidity

While spin-zero color superconductors resemble usual electronic superconductors, spin-one color superconductors, which are of our main interest in this thesis, have a lot in common also with superfluidity in helium-3. This is briefly outlined here.

It is well known that helium is the second lightest element after hydrogen. It be-comes liquid when cooled to a very low temperature. Helium is the only substance that remains liquid at absolute 0 K. There are two stable isotopes of helium, ^{3}He and ^{4}He, which behave very differently at temperatures below a few Kelvin. The superfluidity in helium was first observed for helium-4 at $T < T_c \simeq 2.17$ K [22]. Later, the superfluid-ity of the ^{3}He isotope was also observed, but at much lower temperatures below about $T_c = 2.5$ mK [23]. It turns out, in fact, that there are several non-equivalent phases of superfluid ^{3}He, which appear under different conditions. The theoretical explanation of the phase structure of superfluid ^{3}He was proposed by Leggett in 1975 [24].

The main reason for the different behavior of ^{4}He and ^{3}He is quantum me-chanics. While ^{4}He atoms are bosons (composed of 4 nucleons and 2 electrons), the appearance of the superfluid phase in ^{4}He is related to the Bose condensation, in which a macroscopic fraction of the atoms is in the lowest energy one-particle state. In con-trast, the nucleus of a helium-3 atom consists of two protons and one neutron which

means the ^{3}He atoms are fermion particles which cannot occupy the same quantum state because of the Pauli exclusion principle. Therefore, superfluidity in ^{3}He can arise only if the analogs of the Cooper pairs made of ^{3}He atoms are formed. This indeed happens at sufficiently low temperature. Such pairs behave as bosons and can form a coherent quantum state with a macroscopic occupation in the lowest energy state.

There are two different superfluid phases in ^{3}He, called phases A and B. While the A phase is anisotropic, the B phase is isotropic. The phase transition between the superfluid and the normal fluid is a continuous, second-order phase transition. The transition between phases A and B is a first-order phase transition.

The differences between phases A and B can be also understood in terms of the internal symmetries of their ground states. The normal fluid ^{3}He is characterized by the following symmetry group

$$G = SO(3)_L \times SO(3)_S \times U(1)_N, \tag{1.10}$$

where $SO(3)_L$ and $SO(3)_S$ describe rotations in the space of the angular momentum and the spin space, respectively; $U(1)_N$ accounts for the particle number conservation. In a superfluid state, some symmetries are broken. In the two superfluid phases of ^{3}He, the symmetry group is lowered down to

$$U(1)_s \times U(1) \qquad \text{in A phase}, \tag{1.11}$$

$$SO(3)_{L+S} \qquad \text{in B phase}, \tag{1.12}$$

respectively. As we will see, somewhat similar symmetry breaking patterns are realized also in spin-one color superconductors discussed in Subsec. 1.2.5 below.

1.2.3   The origin of color superconductivity

In general, the concept of color superconductivity [25, 26, 27, 28, 29, 30, 31, 32, 33, 34] is very similar to ordinary superconductivity, see Subsec. 1.2.1, but realized in quark matter.

In the ground state of non-interacting quark matter at zero temperature, the quark distribution function is given by

$$f_F(\mathbf{k})|_{T=0} = \Theta(\mu - E_\mathbf{k}), \qquad (1.13)$$

where μ is the quark chemical potential, Θ is the Heaviside step function and $E_\mathbf{k} \equiv \sqrt{k^2 + m^2}$ is the energy of a free quark (with rest mass m) in the quantum state with the momentum $\mathbf{k}$ (by definition, $k \equiv |\mathbf{k}|$). As one can see, $f_F(\mathbf{k}) = 1$ for the states with $k < k_F \equiv \sqrt{\mu^2 - m^2}$, indicating that all states with the momenta less than the Fermi momentum k_F are occupied. The states with the momenta greater than the Fermi momentum k_F are empty, i.e., $f_F(\mathbf{k}) = 0$ for $k > k_F$.

Because of the property of asymptotic freedom in QCD [35, 36, 37], quarks are weakly interacting at sufficiently high density and low temperature of matter. At the same time, the non-interacting ground state described by Eq. (1.13), is not an approximate ground state of interacting quark matter, even if the interaction is arbitrarily weak. Quarks near the Fermi surface form Cooper pairs just like the electrons do in usual superconductors. This then results in color superconductivity because the quark Cooper pairs are bosons and, at zero temperature, they occupy the same lowest energy quantum state.

In QFT language, the quark (Cooper) pair condensate can be identified with the expectation value of the one-particle-irreducible quark-quark two-point function (anomalous self-energy), i.e.,

$$< \psi_{ia}^\alpha \psi_{jb}^\beta > \propto P_{ijab}^{\alpha\beta} \Delta. \qquad (1.14)$$

Here ψ is the quark field operator, α and β are the color indices, i, j and a, b are the flavor indices and the spinor Dirac indices. The color-flavor-spin matrix P represents a particular pairing channel and Δ is the gap parameter. From here we see that we

12
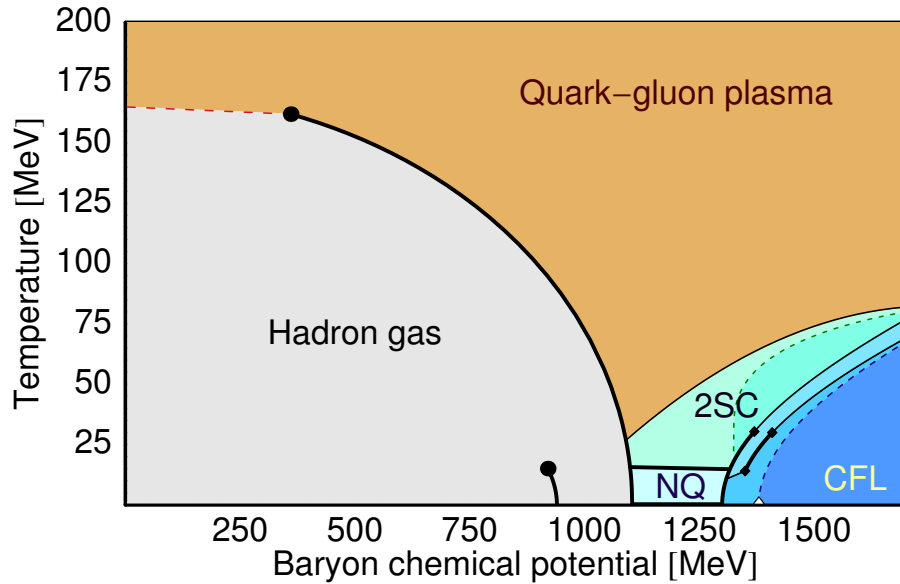
Figure 1.3: Schematic view of the QCD phase diagram, based on the results of Rüster *et al.* [38].

need to know the color-flavor-spin structure for different patterns of pairing and the gap parameters in order to understand the properties of color superconductivity.

An example of a phase diagram of QCD, obtained within a Nambu-Jona-Lasinio (NJL) model [39], is given in Fig. 1.3. This diagram, based on the results of Ref. [38], displays several regions that are relevant for the dynamics of the Early Universe, heavy ion collisions, and stars. One should mention here that the NJL model provides a very crude description of the QCD matter in the regime of large values of the chemical potential. However, in absence of a better model, it can provide some qualitative guidance to the possible phases of matter based on their symmetry properties. (Note that there exist no reliable schemes to study QCD in this nonperturbative regime from first principles because of a strong interaction. Also, one cannot simulate QCD with nonzero chemical potential on a lattice because of the sign problem [40].) The phase diagram in Fig. 1.3, therefore, could be used as a schematic representation of a possible phase diagram. As we see, in accordance with general expectations, at sufficiently high baryon

13

chemical potential and low temperature, there may exist some color superconducting phases.

As present, many phases of quark matter have been studied. From the perspective of spin, we can classify these phases into two kinds: spin-0 color superconductivity and spin-1 color superconductivity which we will discuss in next two subsections.

1.2.4 Spin-0 color superconductivity

In spin-0 color superconductor, the quarks in the Cooper pairs have opposite spin. There are 2 important color superconducting phases, the color-flavor locked (CFL) phase and the two-flavor color superconducting (2SC) phase.

The CFL phase is the color superconducting phase at the highest densities. In this phase, up, down and strange quarks are treated on equal footing and the disruptive effects of the strange quark mass are negligible. The three quark flavors have the same Fermi energies. Around the Fermi surface, all quarks (3 colors times 3 flavors) form Cooper pairs with the zero total momentum and zero total spin. As a result, all quark quasiparticles are gapped, with the estimated value of the gap parameter $\Delta_0 \sim 10 - 100$ MeV [41, 42, 43].

The pairing pattern of the CFL phase is given by

$$< \psi_i^\alpha C \gamma^5 \psi_j^\beta > \propto \Delta_{CFL} \varepsilon^{\alpha\beta A} \varepsilon_{ijA}. \tag{1.15}$$

Color indices α, β and flavor indices i, j run from 1 to 3. C is the Dirac charge-conjugation matrix, Δ_{CFL} is the CFL gap parameter. This is the only possible pattern with all three colors and three flavors participating on equal footing in conventional zero-momentum spinless Cooper pairs at high densities. The masses of all the quarks can be neglected.

14

In the ground state with such a condensate, the color and flavor symmetries are broken down to the diagonal subgroup as follows:

$$SU(3)_c \times SU(3)_L \times SU(3)_R \times U(1)_B \to SU(3)_{c+L+R} \times \mathbb{Z}_2. \qquad (1.16)$$

In the 2SC phase, up and down quarks, which are (approximately) massless and have the same chemical potential, form Cooper pairs with each other. The pairing pattern of the 2SC phase is given by

$$< \psi_i^\alpha C \gamma^5 \psi_j^\beta > \propto \Delta_{2SC} \varepsilon_{ij3} \varepsilon^{\alpha\beta3}. \qquad (1.17)$$

From the structure in Eq. (1.17), we can find that only quarks with two (red and green) out of three colors participate in the Copper pairing of the 2SC phase, while quarks with the third (blue) color are unpaired. In other words, the original six quark states give rise to two doublets of gapped quasiparticles and two unpaired quasiparticles (singlets with respect to the $SU(2)_c$ unbroken gauge group). The Copper pair condensates involve the combinations of u_r-d_g and u_g-d_r only. It should be noted that the color indices in Eq. (1.17) may have an arbitrary orientation in the color space, since it can be changed by the global color transformations. We choose the condensate to point into the third (blue) color direction by convention. Based on the color-flavor structure for the 2SC phase, the corresponding symmetry breaking pattern is

$$SU(3)_c \times U(1)_B \to SU(2)_c \times U(1)_{\tilde{B}}. \qquad (1.18)$$

If the masses of up and down quarks are neglected, the global $SU(2)_L \times SU(2)_R$ chiral symmetry present in two-flavor QCD is not broken in the 2SC phase. As a consequence of the condensate pointing in the antiblue color direction, see Eq. (1.17), the color $SU(3)_c$ gauge symmetry is broken down to the $SU(2)_c$ color gauge subgroup. Therefore, five out of total eight gluons of $SU(3)_c$ gauge group become massive due to the Meissner effect, while the other three gluons, corresponding to the unbroken

15

$SU(2)_c$ gauge group, remain massless. Although the original $U(1)_B$ baryon number symmetry in vacuum is broken in the 2SC phase, a new "rotated" $U(1)_{\tilde{B}}$ baryon number symmetry in medium remains unbroken. This means that the quark matter in the 2SC phase, unlike in the CFL phase, is not superfluid.

1.2.5 Spin-1 color superconductors

In realistic neutral quark matter in β equilibrium, a mismatch between the Fermi momenta of different quark flavors becomes almost inevitable because of the effect of non-equal quark masses [44]. If the strength of diquark pairing is not strong enough to overcome the mismatch, spin-0 color superconductivity cannot occur. In this case, one should consider the possibility of spin-one, same-flavor Cooper pairing [45, 46, 47, 48, 49, 50, 51]. The Pauli principle does not allow the construction of spin-0 Cooper pairs from quarks of the same flavor. Indeed, while same-flavor pairing may formally correspond to a spin-zero, color-symmetric state, this cannot be realized because there is no attractive interaction in the corresponding channel. The color antisymmetric wave function of a pair can only be spin symmetric. This corresponds to a spin-1 state. Cooper pairs in spin-one color superconducting phases are given by diquarks in a color antitriplet (antisymmetric) and spin triplet (symmetric) state. Depending on a specific color-spin structure, which is determined by the alignments of the antitriplet in color space and the triplet in spin (coordinate) space, many inequivalent color superconducting phases may form.

Each phase is unambiguously specified by the structure of the gap matrix, which is commonly written in the following form [52]:

$$\Phi(P)^+ = \sum_{e=\pm} \phi^e(P) \mathscr{M}_{\mathbf{p}} \Lambda_{\mathbf{p}}^e, \tag{1.19}$$

where $\phi^e(P)$ is the gap function. The Dirac matrices $\Lambda_{\mathbf{p}}^e \equiv (1 + e \gamma_0 \boldsymbol{\gamma} \cdot \hat{\mathbf{p}})/2$, with $e = \pm$, are the projectors onto the positive and negative energy states. The color structure of

16

$\Phi(P)^+$ is determined by

$$\mathscr{M}_{\mathbf{p}} = \sum_{i,j=1}^{3} J^i \Delta_{ij} \left[\hat{p}^j \cos\theta + \gamma^j_\perp \sin\theta \right]. \qquad (1.20)$$

where $(J^i)^{jk} = -i\varepsilon^{ijk}$ are the antisymmetric matrices in color space, $\hat{\mathbf{p}} \equiv \mathbf{p}/p$ is the unit vector in the direction of the quasiparticle three-momentum $\mathbf{p}$, and $\gamma^j_\perp \equiv \gamma^j - \hat{p}^j(\boldsymbol{\gamma}\cdot\hat{\mathbf{p}})$. The explicit form of the 3×3 matrix Δ_{ij} and the value of the angular parameter θ determine specific phases of superconducting matter. Among them, there is a number of inert and noninert spin-one phases [53, 54], which are naturally characterized by the continuous and discrete symmetries preserved in the ground state.

In the two special cases, $\theta = 0$ and $\theta = \pi/2$, the corresponding phases are called longitudinal and transverse, respectively. In this thesis we focus on the transverse phases ($\theta = \pi/2$), in which only quarks of the opposite chiralities pair and which have lower free energies than the longitudinal phases [52]. To further constrain the large number of possibilities, we concentrate only on the following four most popular ones: the color-spin locked phase (CSL), the A-phase, the polar phase and the planar phase. The A phase and the CSL phase are analogous to the A and B phases in superfluid ^{3}He, which were discussed in Subsec. 1.2.2.

The structure of the matrices Δ_{ij} and $\mathscr{M}_{\mathbf{p}}$ for the mentioned four phases are quoted in the first two rows of Tab. 1.1 (for more details see Refs. [52]). In the corresponding ground states, the original symmetry $SU(3)_c \times SO(3)_J \times U(1)_{\text{em}}$ of one-flavor quark matter breaks down to [49, 51, 52, 53, 54, 55]

$$\begin{aligned}
&\widetilde{SO}(3)_J && \text{(CSL)}, \\
&SU(2)_c \times \widetilde{SO}(2)_J \times \tilde{U}(1)_{\text{em}} && \text{(A-phase)}, \\
&SU(2)_c \times SO(2)_J \times \tilde{U}(1)_{\text{em}} && \text{(polar)}, \\
&\widetilde{SO}(2)_J \times \tilde{U}(1)_{\text{em}} && \text{(planar)},
\end{aligned}$$

respectively. The rotation symmetry is partially broken in the last three cases. In polar

17

phase, the superconducting phase is invariant under rotations around one fixed axis in real space. In planar phase, the superconducting state is invariant under a special joint rotation in color and real space. And in CSL phase, any rotation in real space leaves the system invariant as long as one simultaneously performs the same rotation in fundamental color space. It is also easy to see that in none of the cases the full color symmetry is preserved. The residual color subgroup $SU(2)_c$ remains unbroken in two of these (A phase and polar phase). This means that only red and green quarks form Cooper pairs. The spontaneously broken symmetry gives rise to massive gauge bosons. For most cases (except CSL phase), there is a Meissner effect for five of the eight gluons. The other three of the gluons do not attain Meissner masses. This proves that no Cooper pairs carry blue color charge. In CSL phase, all eight gluons attain Meissner masses.

It has been argued that the lowest free energy phase is the transverse CSL phase [52]. The value of the spin-1 gap is estimated to be about two or three orders of magnitude smaller than a typical spin-0 gap. It can realistically be about $1\,\mathrm{MeV}$, but may well be less than $0.1\,\mathrm{MeV}$. However, even a very small gap like this can substantially affect the cooling rate of a quark star [56]. Also, as discussed in Ref [51], the electromagnetic Meissner effect present in spin-1 superconductors (in contrast to the case of spin-0 2SC and CFL phases) have observable effects on the magnetic field relaxation in pulsars. The non-zero gaps can also strongly modify the rates of the weak processes in quark matter. As we discuss in the next subsection, such processes affect the viscous properties of matter, which are responsible for the rotational slowdown of stars under certain conditions.

In spin-one color superconductors, there is no cross-flavor pairing and, therefore, the quark propagator is diagonal in flavor space, i.e.,

$$S(P) = \mathrm{diag}[S_u(P), S_d(P), S_s(P)]. \tag{1.21}$$

	CSL phase	planar phase	polar phase	A-phase
Δ_{ij}	δ_{ij}	$\delta_{i1}\delta_{j1}+\delta_{i2}\delta_{j2}$	$\delta_{i3}\delta_{j3}$	$\delta_{i3}(\delta_{j1}+i\,\delta_{j2})$
$\mathscr{M}_{\mathbf{p}}$	$\mathbf{J}\cdot\gamma_{\perp}(\hat{\mathbf{p}})$	$J_1\gamma_{\perp,1}(\hat{\mathbf{p}})+J_2\gamma_{\perp,2}(\hat{\mathbf{p}})$	$J_3\gamma_{\perp,3}(\hat{\mathbf{p}})$	$J_3[\gamma_{\perp,1}(\hat{\mathbf{p}})+i\,\gamma_{\perp,2}(\hat{\mathbf{p}})]$
$\lambda_{\mathbf{p},1}\ (n_1)$	2 (8)	$1+\cos^2\theta_{\mathbf{p}}$ (8)	$\sin^2\theta_{\mathbf{p}}$ (8)	$(1+|\cos\theta_{\mathbf{p}}|)^2$ (4)
$\lambda_{\mathbf{p},2}\ (n_2)$	0 (4)	0 (4)	0 (4)	$(1-|\cos\theta_{\mathbf{p}}|)^2$ (4)
$\lambda_{\mathbf{p},3}\ (n_3)$	—	—	—	0 (4)

Table 1.1: Matrices Δ_{ij} and $\mathscr{M}_{\mathbf{p}}$ as well as the eigenvalues $\lambda_{\mathbf{p},r}$ with the corresponding degeneracies n_r in four spin-one color superconducting phases. The angle between $\mathbf{p}$ and the z-axis is denoted by $\theta_{\mathbf{p}}$.

The Nambu-Gorkov structure of each flavor-diagonal element is given by

$$
S_f^{<,>}(P) = \begin{pmatrix} G_{f,+}^{<,>}(P) & F_{f,-}^{<,>}(P) \\ F_{f,+}^{<,>}(P) & G_{f,-}^{<,>}(P) \end{pmatrix}, \tag{1.22}
$$

where $f = u,d,s$. The normal (diagonal) and anomalous (off-diagonal) components of the Nambu-Gorkov propagator have the following structure [52]:

$$
G_{f,\pm}^{<,>}(P) = \gamma_0\Lambda_{\mathbf{p}}^{\mp}\sum_r \mathscr{P}_{\mathbf{p},r}^{\pm}G_{\pm,r,f}^{<,>}(P), \tag{1.23}
$$

$$
F_{f,+}^{<,>}(P) = -\gamma_0\mathscr{M}_{\mathbf{p}}\gamma_0\sum_{e,r} \mathscr{P}_{\mathbf{p},r}^{+}\Lambda_{\mathbf{p}}^{-e}F_{+,r,f}^{<,>}(P), \tag{1.24}
$$

$$
F_{f,-}^{<,>}(P) = -\mathscr{M}_{\mathbf{p}}^{\dagger}\sum_{e,r} \mathscr{P}_{\mathbf{p},r}^{-}\Lambda_{\mathbf{p}}^{e}F_{-,r,f}^{<,>}(P). \tag{1.25}
$$

Here, r labels different quasiparticle excitations in color-superconducting quark matter. The matrices $\mathscr{P}_{\mathbf{p},r}^{-}$ and $\mathscr{P}_{\mathbf{p},r}^{+}$ are the projectors onto the subspaces spanned by the eigenvectors of $\mathscr{M}_{\mathbf{p}}\mathscr{M}_{\mathbf{p}}^{\dagger}$ and $\gamma^0\mathscr{M}_{\mathbf{p}}^{\dagger}\mathscr{M}_{\mathbf{p}}\gamma^0$, respectively. The explicit form of the projectors for each phase can be found in Ref. [56]. It should be noted that both matrices $\mathscr{M}_{\mathbf{p}}\mathscr{M}_{\mathbf{p}}^{\dagger}$ and $\gamma^0\mathscr{M}_{\mathbf{p}}^{\dagger}\mathscr{M}_{\mathbf{p}}\gamma^0$ have the same set of eigenvalues $\lambda_{\mathbf{p},r}$,

$$
\mathscr{M}_{\mathbf{p}}\mathscr{M}_{\mathbf{p}}^{\dagger} \equiv \sum_r \lambda_{\mathbf{p},r}\mathscr{P}_{\mathbf{p},r}^{-}, \tag{1.26}
$$

$$
\gamma^0\mathscr{M}_{\mathbf{p}}^{\dagger}\mathscr{M}_{\mathbf{p}}\gamma^0 \equiv \sum_r \lambda_{\mathbf{p},r}\mathscr{P}_{\mathbf{p},r}^{+}. \tag{1.27}
$$

The list of all eigenvalues as well as their degeneracies are given in the last three rows of Tab. 1.1. Each of the eigenvalues determines a quark quasiparticle with the following

dispersion relation:

$$\varepsilon_{\mathbf{p},r,f} = \sqrt{(p-\mu_f)^2 + |\phi|^2 \lambda_{\mathbf{p},r,f}}. \tag{1.28}$$

The separate components of the propagators in subspaces spanned by the eigenvectors, see Eqs. (1.23), (1.24) and (1.25), can be conveniently rewritten in terms of the corresponding distribution functions $f(\varepsilon_{p,r,f})$ and the Bogoliubov coefficients $B^{\pm}_{\mathbf{p},r,f}$, i.e.,

$$G^{>}_{\pm,r,f}(P) = -2\pi i \sum_{e=\pm} B^{\pm e}_{\mathbf{p},r,f} f(e\varepsilon_{\mathbf{p},r,f}) \delta(p_0 \pm \mu_f - e\varepsilon_{\mathbf{p},r,f}), \tag{1.29}$$

$$G^{<}_{\pm,r,f}(P) = -2\pi i \sum_{e=\pm} B^{\pm e}_{\mathbf{p},r,f} f(-e\varepsilon_{\mathbf{p},r,f}) \delta(p_0 \pm \mu_f - e\varepsilon_{\mathbf{p},r,f}), \tag{1.30}$$

$$F^{>}_{\pm,r,f}(P) = 2\pi i \frac{\phi}{2\varepsilon_{\mathbf{p},r,f}} \sum_{e=\pm} e f(e\varepsilon_{\mathbf{p},r,f}) \delta(p_0 \mp \mu_f - e\varepsilon_{\mathbf{p},r,f}), \tag{1.31}$$

$$F^{<}_{\pm,r,f}(P) = 2\pi i \frac{\phi}{2\varepsilon_{\mathbf{p},r,f}} \sum_{e=\pm} e f(-e\varepsilon_{\mathbf{p},r,f}) \delta(p_0 \pm \mu_f - e\varepsilon_{\mathbf{p},r,f}). \tag{1.32}$$

The Bogoliubov coefficients and the fermion distribution function are defined as follows:

$$B^e_{\mathbf{p},r,f} = \frac{1}{2} - e \frac{p-\mu_f}{2\varepsilon_{\mathbf{p},r,f}}, \tag{1.33}$$

$$f(\varepsilon) = \frac{1}{\exp(\frac{\varepsilon}{T}) + 1}. \tag{1.34}$$

1.3 Weak processes and viscosity in neutron stars

As we know, there are four fundamental interactions in nature: strong, weak, electromagnetic and gravitational. In the 1960s, Glashow, Weinberg and Salam showed that the electromagnetic and weak interactions can be combined in a unified framework of the electro-weak theory. The weak interaction acts between left-handed leptons and quarks and is due to an exchange of heavy $W^{\pm}$ and Z bosons. The weak interactions have several unique attributes: (i) they are the only types of interaction that affect neutrinos; (ii) they are the only interactions that are capable of changing the quark flavors; (iii) they are the only interactions that violate the parity symmetry P and the CP symmetry [57]; (iv) they are mediated by heavy gauge bosons, which come as an outcome of the so-called Higgs mechanism in the Standard Model [58].

20

u s s u u s s u u d d u

W W W W e W W e

d u u d e ν_e $\overline{\nu}_e$ e ν_e $\overline{\nu}_e$

(a)   *(b)*   *(c)*   *(d)*   *(e)*   *(f)*
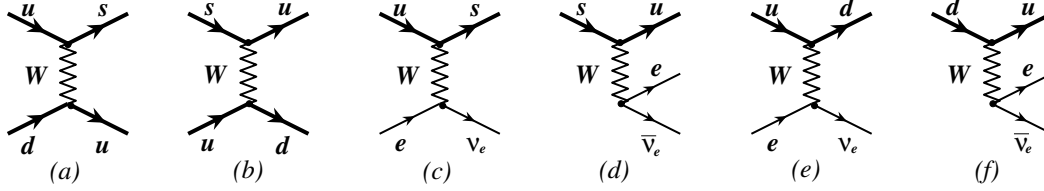
Figure 1.4: Weak processes in dense quark matter.

In the neutron stars, we have two types of weak processes: nonleptonic processes ($u + s \leftrightarrow u + d$) and semileptonic processes (Urca), see Fig. 1.4. They provide the microscopic mechanism for the viscosity of Stellar matter.

When the viscosity of stellar matter is not very high, a star has a tendency to spontaneously develop instabilities by emitting gravitational waves [59, 60, 61, 62] (for reviews on this topic see, e.g., Refs. [63, 64]). Among various types of instabilities, the so-called rotation-dominated (r-mode) instabilities might be the most important to consider. They can develop at a relatively low angular velocity, and therefore may be relevant for a large number of compact stars.

This observation makes it particularly important to study the bulk and shear viscosity of color superconducting matter [65, 66, 67, 68, 69]. The bulk viscosity is a measure of the energy density dissipation during the expansion and compression of a fluid. When the expansion or the compression drives the system out of chemical equilibrium, microscopic (weak) processes will attempt to re-equilibrate the system. As an outcome, the kinetic energy of the macroscopic motion of the fluid is partially converted into the thermal kinetic motion. In essence, this is the mechanism responsible for the bulk viscosity in stellar quark matter at not very low temperatures. It is the shear viscosity that damps the instabilities at low temperatures [70].

The Urca processes are the main weak processes that determine the bulk viscosity in non-strange quark stars. This was analyzed in Ref. [65] in detail. It is commonly

argued that the bulk viscosity in the normal phase of three-flavor quark matter is dominated by the nonleptonic weak processes [71, 72, 73, 74, 75, 76]. Recently it was shown [77] that the interplay between the Urca and the nonleptonic processes may be rather involved. Indeed, because of the resonance-type dynamics that determines the bulk viscosity and because of a subtle interference between the two types of the weak processes, the Urca processes under certain conditions may still contribute a lot to the bulk viscosity [77].

Also we should mention that the common feature of the Urca processes is the emission of neutrinos. Because of this neutrino emission, the Urca processes are of prime importance for cooling of neutron stars during the first million years of their evolution [78, 79, 80, 81].

1.4 Graphene

The first application of carbon materials can be traced back to 3750 BC. Egyptians and Sumerians used charcoal to reduct copper, zinc and tin ores in the manufacture of bronze. The first recorded application of charcoal for medicinal purposes was cited in Egyptian papyri in 1500 BC. The principle use appears to have been the application of charcoal to adsorb odorous vapours from putrefying wounds and from within the intestinal tract. One of the most important carbon materials, graphite was named by Abraham Gottlob Werner in 1789.[2] Since 1940's, carbon materials have been attracting interest from researchers all over the world. In 1946, Wallace started the study of the band structure in graphite [82]. His starting point in the analysis was a single layer of graphite. In 1950s, McClure and his colleagues developed the Slonczewski-Weiss-McClure (SWM) band structure [83]. In 1968, Schroeder determined the position of the current electron and hole pockets in the band structure [84]. In 1984, Semenoff [85], DeVincenzo and Mele [86] pointed out the massless Dirac equation for the 1-layer system (i.e., graphene). But it was not until 2004 when the first graphene sample was made in a lab [87]. After that numerous experiments were performed to verify theoretical predictions of its properties [88]. Among them, one important discovery is that in 2005. Novoselov and Geim found the anomalous integer quantum Hall effect of graphene in their experiment [89]. Since then, graphene research exploded. The property of interest for us is its unusual electronic structure that can be described in terms of massless two-dimensional Dirac particles. As stated earlier, we know that matter made of massless Dirac particles is relativistic matter. Now let us give a brief introduction to graphene and its properties.

Graphene is a single two-dimensional layer of carbon atoms bound in a hexagonal lattice structure. It is one of the strongest materials in nature because of the strength

---

[2]Graphite is the word from the Ancient Greek, means "to draw/write" for its use in pencils.

and specificity of its covalent bonds. The structure of graphene can be treated as a triangular lattice with a basis of two atoms per unit cell. Each carbon atom has a distance $a = 1.42$ Å with its three neighbors. The electronic configuration of carbon atom is $1s^2 2s^2 2p^2$. The 1s electrons do not contribute to the chemical bond. So, the properties of graphene can be described in terms of $2s$ and $2p_x$, $2p_y$ and $2p_z$ orbitals, they hybridize to form three new planar orbitals sp^2. Each of the orbitals contains one electron. These sp^2 orbitals of different atoms combine to σ bonds. The properties of graphene are determined by these bonds. Also there is a fourth orbital p_z. This is the orbital perpendicular to the plane in which the atoms sit. p_z orbitals covalently with neighboring atoms leading to the formation of a π band.

The lattice vectors of graphene are:

$$\mathbf{a_1} = \frac{a}{2}(3, \sqrt{3}), \quad \mathbf{a_2} = \frac{a}{2}(3, -\sqrt{3}), \tag{1.35}$$

and the nearest neighbor vectors are

$$\delta_1 = a(1,0), \quad \delta_2 = \frac{a}{2}(-1, \sqrt{3}), \quad \delta_3 = \frac{a}{2}(-1, -\sqrt{3}). \tag{1.36}$$

The tight-binding Hamiltonian for electrons in graphene can be defined as:

$$H = -t\Sigma_{<i,j>,\sigma}(a_{\sigma,i}^{\dagger}b_{\sigma,j} + h.c.) - t'\Sigma_{<i,j>,\sigma}(a_{\sigma,i}^{\dagger}a_{\sigma,j} + b_{\sigma,i}^{\dagger}b_{\sigma,j} + h.c.). \tag{1.37}$$

Here $a_{\sigma,i}$ ($a_{\sigma,i}^{\dagger}$) is the annihilation (creation) operator for an electron with spin σ (the same for b). t is the nearest neighbor hopping energy and t' is the next nearest neighbor hopping energy. The energy bands derived from this Hamiltonian can be represented as

$$E_{\pm}(\mathbf{k}) = \pm t\sqrt{3 + f(\mathbf{k})} - t'f(\mathbf{k}),$$
$$f(\mathbf{k}) = 2\cos(\sqrt{3}) + 4\cos\left(\frac{\sqrt{3}}{2}k_y a\right)\cos\left(\frac{3}{2}k_x a\right). \tag{1.38}$$

The first Brillouin zone can be represented by the vectors

$$\mathbf{b_1} = \frac{2\pi}{3a}(1, \sqrt{3}), \quad \mathbf{b_2} = \frac{2\pi}{3a}(1, -\sqrt{3}). \tag{1.39}$$

24

The Dirac points are located on

$$\mathbf{K} = \left(\frac{2\pi}{3a}, \quad \pm \frac{2\pi}{3\sqrt{3}a} \right) \tag{1.40}$$

in momentum space. Then, it can be easily shown that near the Dirac points, the dispersion relation can be approximated as

$$E_{\pm}(\mathbf{q}) \approx \pm v_F |\mathbf{q}| + \mathcal{O}((q/K)^2), \tag{1.41}$$

where $\mathbf{q}$ is the momentum relative to the Dirac points and the Fermi velocity is given by $v_F = 3ta/2 \approx 10^6$ m/s. The linear structure is not sufficient to give Dirac fermions, but in graphene the full structure can be proved [85, 86].

1.4.1 Quantum Hall Effect in graphene

The classical Hall effect was discovered by Hall in 1879. He showed that the traverse resistance of a thin metallic plate varies linearly with the strength B of the perpendicular magnetic field,

$$R_H = \frac{B}{qn_{el}}. \tag{1.42}$$

Here q is the carrier charge and $n_e l$ is the two-dimensional carrier density.

The discovery of the integer quantum Hall effect was awarded with a Nobel prize in 1985 to V. Klitzing. In addition, the discovery and theory of the fractal quantum Hall effect was awarded a Nobel prize in 1998 to Tsui, Stormer and Laughlin. The quantum Hall effect is observed in two-dimensional electron systems at low temperatures and in strong magnetic fields. The Hall conductivity is

$$\sigma = \frac{ne^2}{h}. \tag{1.43}$$

Here, n is the filling factor which can take integer or fractional values.

Graphene has an anomalous quantum Hall effect in the presence of a magnetic field. In weak magnetic fields, experimental observation [89, 90] finds that the Hall

25

conductivity is

$$\sigma_{xy} = \pm 4 \left(n + \frac{1}{2} \right) \frac{e^2}{h}.$$ (1.44)

Here, n is the Landau level index. The factor of 4 corresponds to the double valley and double spin degeneracies. The shift of $1/2$ in the Hall conductivity reveals the relativistic-like character of electron motion in graphene [91, 92, 93].

It is also interesting to show the quantum Hall effect in graphene in strong magnetic fields (above 10 Teslas), the Hall conductivity at $\sigma_{xy} = \nu e^2/h$ with $\nu = 0, \pm 1, \pm 3, \pm 4$ and the fractional quantum Hall effect with $\nu = 1/3$ were observed by several groups [94, 95, 96]. For example, the integer quantum Hall effect at $\nu = 0, \pm 4$ can be explained by a dynamical enhancement of Zeeman splitting (or dynamical Dirac mass generation), when the $U(4)$ flavor group is reduced down to a $U_{\uparrow}(2) \times U_{\downarrow}(2)$. Here $U_{\uparrow,\downarrow}(2)$ is the sublattice-valley symmetry at a fixed spin (up or down). The states at $\nu = \pm 1, \pm 3$ can appear only when there are both dynamical enhancement of Zeeman splitting and Dirac mass generation.

When there is no enhancement of Zeeman splitting and no Dirac mass generation, however, the $U(4)$ flavor group is a good symmetry at all realistic fields, and then the Hall conductivity Eq. (1.44) appears. The anomalous quantization of Hall conductivity played a key role to empirically confirm that charge carriers in graphene are described by massless Dirac quasiparticles [85].

1.4.2   Optical conductivity of graphene

The double Dirac cone band structure in graphene affects the optical transmission. While photons are absorbed, a quasiparticle is promoted from an occupied valence state below the Fermi energy to an empty state above Fermi energy. The optical conductivity tensor is given by the Kubo formula [97]

$$\sigma_{ij}(\mathbf{q}, \omega) = \frac{1}{\omega v} \int_{-\infty}^{t} dt' e^{i\omega(t-t')} < \psi|[j_i^{\dagger}(\mathbf{q},t), j_j(\mathbf{q},t')]|\psi > + i \frac{n_0 e^2}{m\omega} \delta_{ij}.$$ (1.45)

Here j_s is the current operator, v is the overall volume, n_0 is the density of particle, m is the mass of particle and ω is the energy of particle.

The current-current correlation function is defined as

$$\Pi_{ij}(\mathbf{q}, t - t') = -\frac{i}{v}\Theta(t - t') < \psi|[j_i^\dagger(\mathbf{q}, t), j_j(\mathbf{q}, t')]|\psi> . \tag{1.46}$$

The Fourier transform is

$$\Pi_{ij}(\mathbf{q}, t - t') = -\frac{i}{v} \int_\infty^{-\infty} dt e^{i\omega(t-t')}\Theta(t - t') < \psi|[j_i^\dagger(\mathbf{q}, t), j_j(\mathbf{q}, t')]|\psi> . \tag{1.47}$$

Then one can find

$$\sigma_{ij}(\mathbf{q}, \omega) = \frac{i}{\omega}\left[\Pi_{ij}(\mathbf{q}, \omega) + \frac{n_0 e^2}{m}\delta_{ij}\right] . \tag{1.48}$$

27

CHAPTER 2

NON-LEPTONIC WEAK PROCESSES IN SPIN-ONE COLOR

SUPERCONDUCTING QUARK MATTER

As we discussed in the previous chapter, the bulk viscosity in quark matter is determined by the rates of weak (Urca and non-leptonic) processes. The rates of Urca processes in spin-one color superconducting quark matter have been calculated in Ref. [65]. In this chapter we will discuss the rates of non-leptonic processes in spin-one color superconducting matter.

2.1 Formalism

In order to calculate the rates of the non-leptonic processes, see Fig. 1.4 (a) and (b), we use the same approach as in Refs. [56, 65, 77, 98, 101]. It is based on the Kadanoff-Baym formalism [102]. The starting point of the analysis is the general Kadanoff-Baym equation for the Green functions (propagators) of the down (or strange) quarks. After applying the conventional gradient expansion close to equilibrium, we derive the following kinetic equation for the d-quark Green function:

$$i\frac{\partial}{\partial t}\text{Tr}[\gamma_0 S_d^<(P_1)] = -\text{Tr}[S_d^>(P_1)\Sigma^<(P_1) - \Sigma^>(P_1)S_d^<(P_1)]. \qquad (2.1)$$

Here we denote the quark four-momenta by capital letters, e.g., $P = (p_0, \mathbf{p})$, where p_0 is the energy and $\mathbf{p}$ is the three-momentum. The structure of the quark Green's functions $S^<(P_1)$ and $S^>(P_1)$ in spin-one color superconducting phases will be discussed in the next subsection. To leading order, the quark self-energies $\Sigma^<(P_1)$ and $\Sigma^>(P_1)$ are given by the Feynman diagram in Fig. 2.1. This translates into the following explicit expression:

$$\Sigma^{<,>}(P_1) = \frac{i}{M_W^4} \int \frac{d^4 P_4}{(2\pi)^4} \Gamma_{ud,-}^\mu S_u^{<,>}(P_4)\Gamma_{ud,+}^\nu \Pi_{\mu\nu}^{>,<}(Q), \qquad (2.2)$$

where, by definition, M_W and $Q = P_1 - P_4$ are the mass and the four-momentum of the W-boson, respectively. (Note that the large hierarchy between the W-boson mass

28
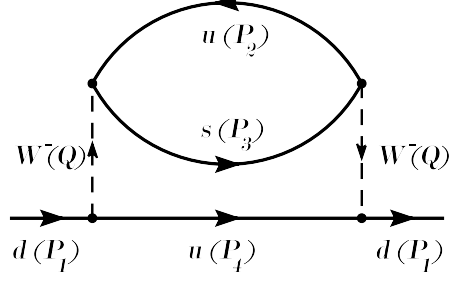
Figure 2.1: Feynman diagram for the d-quark self-energy. The particle four-momenta are shown in parenthesis next to the particle names.

and a typical momentum transfer $Q \lesssim 1$ MeV justifies the approximation in which the W-boson propagator is replaced by $1/M_W^2$.) As seen from the diagram in Fig. 2.1, the expression for the polarization tensor of the W-boson is given by

$$\Pi_{\mu\nu}^{<,>}(Q) = -i \int \frac{d^4 P_2}{(2\pi)^4} \text{Tr}\left[\Gamma_{us,+}^{\mu} S_s^{>,<}(P_2 + Q)\Gamma_{us,-}^{\nu} S_u^{<,>}(P_2)\right]. \tag{2.3}$$

In the Nambu-Gorkov notation used here, the explicit form of the (tree-level) vertices for the weak processes $d \leftrightarrow u + W^-$ and $s \leftrightarrow u + W^-$ reads [101]

$$\Gamma_{ud/us,\pm}^{\mu} = \frac{e\, V_{ud/us}}{2\sqrt{2}\sin\theta_W}\begin{pmatrix} \gamma^{\mu}(1-\gamma^5)\,\tau_{ud/us,\pm} & 0 \\ 0 & -\gamma^{\mu}(1+\gamma^5)\,\tau_{ud/us,\mp} \end{pmatrix}. \tag{2.4}$$

These are given in terms of the elements of the Cabibbo-Kobayashi-Maskawa matrix V_{ud} and V_{us}, and the weak mixing angle θ_W. By construction, the τ-matrices operate in flavor space (u,d,s) and have the following form:

$$\tau_{ud,+} \equiv \begin{pmatrix} 0 & 1 & 0 \\ 0 & 0 & 0 \\ 0 & 0 & 0 \end{pmatrix}, \quad \tau_{ud,-} \equiv \begin{pmatrix} 0 & 0 & 0 \\ 1 & 0 & 0 \\ 0 & 0 & 0 \end{pmatrix},$$

$$\tau_{us,+} \equiv \begin{pmatrix} 0 & 0 & 1 \\ 0 & 0 & 0 \\ 0 & 0 & 0 \end{pmatrix}, \quad \tau_{us,-} \equiv \begin{pmatrix} 0 & 0 & 0 \\ 0 & 0 & 0 \\ 1 & 0 & 0 \end{pmatrix}. \tag{2.5}$$

29

By making use of Eqs. (2.1) and (2.2), the kinetic equation takes the following form:

$$
i\frac{\partial}{\partial t}\mathrm{Tr}[\gamma_0 S_d^<(P_1)] = -\frac{i}{M_W^4}\int\frac{d^4P_4}{(2\pi)^4}\mathrm{Tr}\Big[S_d^>(P_1)\Gamma_{ud,-}^\mu S_u^<(P_4)\Gamma_{ud,+}^\nu\Pi_{\mu\nu}^>(Q)
$$
$$
-\Gamma_{ud,-}^\mu S_u^>(P_4)\Gamma_{ud,+}^\nu S_d^<(P_1)\Pi_{\mu\nu}^<(Q)\Big]. \tag{2.6}
$$

The physical meaning of the expression on the left hand side of this equation is the time derivative of the d-quark distribution function. By integrating this over the complete phase space, we obtain the net rate of the d-quark production:

$$
\Gamma_d \equiv -\frac{i}{4}\frac{\partial}{\partial t}\int\frac{d^4P_1}{(2\pi)^4}\mathrm{Tr}[\gamma_0 S_d^<(P_1)]. \tag{2.7}
$$

Then, by making use of the kinetic equation (2.1), we derive

$$
\Gamma_d = \frac{i}{4M_W^4}\int\frac{d^4P_1}{(2\pi)^4}\int\frac{d^4P_4}{(2\pi)^4}\Big[\mathrm{Tr}\Big(S_d^>(P_1)\Gamma_{ud,-}^\mu S_u^<(P_4)\Gamma_{ud,+}^\nu\Big)\Pi_{\mu\nu}^>(Q)
$$
$$
- \mathrm{Tr}\Big(\Gamma_{ud,-}^\mu S_u^>(P_4)\Gamma_{ud,+}^\nu S_d^<(P_1)\Big)\Pi_{\mu\nu}^<(Q)\Big]. \tag{2.8}
$$

This rate should be non-vanishing only if the rates of the two non-leptonic weak processes $u+s\to d+u$ and $d+u\to u+s$ differ. In β-equilibrium, in particular, the latter two should be equal and the net rate of the d-quark production should vanish. The corresponding state of equilibrium in dense quark matter is reached when the chemical potentials of all three quark flavors are equal, i.e., $\mu_u=\mu_d=\mu_s$. (For simplicity, here it is assumed that all three quark flavors are approximately massless and, therefore, that the electrical neutrality of quark matter is achieved without the need for the electrons.)

When the system is forced out of equilibrium, e.g., during the density oscillations caused by the collective modes of stellar matter, small deviations from β-equilibrium are induced. For our purposes, the corresponding state can be described by the following set of the chemical potentials: $\mu_u=\mu_d=\mu$ and $\mu_s=\mu+\delta\mu$, where $\delta\mu$ is a small parameter that characterizes the magnitude of the departure from the equilibrium state. Out of equilibrium, the net production of d-quarks may be nonzero.

For example, if $\delta\mu > 0$ ($\delta\mu < 0$) the system has a deficit (an excess) of the down quarks and an excess (a deficit) of the strange quarks. Then, one of the weak processes, i.e., $u + s \rightarrow d + u$ ($d + u \rightarrow u + s$), will start to dominate over the other in order to restore the equilibrium. The net rate of the d-quark (or equivalently s-quark) production characterizes how quickly this happens.

In order to calculate the net rate of d-quark production, we need to use the explicit structure of the quark propagators in the specific spin-one color superconducting phases. The quark propagators in Eq. (1.22) can now be used to derive the general expressions for $\Pi_{\mu\nu}^{<}(Q)$ and $\Pi_{\mu\nu}^{>}(Q)$. This is done in the next subsection. The results are then used to calculate the rate Γ_d in Eq. (2.8).

The W-boson polarization tensor is given in terms of the quark propagators in Eq. (2.3). By taking into account the Nambu-Gorkov and flavor structure of the weak interaction vertices in Eq. (2.4), as well as the quark propagator in Eq. (1.22), we derive

$$\Pi_{\mu\nu}^{<,>}(Q) = -\frac{ie^2 V_{us}^2}{8\sin^2\theta_W} \int \frac{d^4 P_2}{(2\pi)^4} \mathrm{Tr}\left[\gamma^\mu(1-\gamma^5)G_{s,+}^{>,<}(P_3)\gamma^\nu(1-\gamma^5)G_{u,+}^{<,>}(P_2)\right.$$
$$\left. +\gamma^\mu(1+\gamma^5)G_{u,-}^{>,<}(P_3)\gamma^\nu(1+\gamma^5)G_{s,-}^{<,>}(P_2)\right], \tag{2.9}$$

where we introduced the notation $P_3 \equiv P_2 + Q$. Note that the anomalous (off-diagonal) elements of the Nambu-Gorkov propagators dropped out from the result. This is the consequence of the electric charge conservation. In calculations, this comes about as a result of the specific flavor structure of the weak interaction vertices in Eq. (2.4). One can further simplify the result for the polarization tensor in Eq. (2.9) by noticing that the two terms on the right hand side are equal. From physical viewpoint, this is related to the fact that the two terms are the charge-conjugate contributions of each other. After taking this into, we arrive at the following expression for the polarization tensor:

$$\Pi_{\mu\nu}^{<,>}(Q) = -\frac{ie^2 V_{us}^2}{4\sin^2\theta_W} \int \frac{d^4 P_2}{(2\pi)^4} \mathrm{Tr}\left[\gamma^\mu(1-\gamma^5)G_{s,+}^{>,<}(P_3)\gamma^\nu(1-\gamma^5)G_{u,+}^{<,>}(P_2)\right]. \tag{2.10}$$

Then, by using the explicit structure of the normal components of the u- and s-quark

31

propagators, defined in Eq. (1.23), we obtain

$$
\begin{aligned}
\Pi_{\mu\nu}^{<,>}(Q) &= -\frac{ie^2 V_{us}^2}{4\sin^2\theta_W}\int\frac{d^4 P_2}{(2\pi)^4}\mathrm{Tr}\Big[\gamma^\mu(1-\gamma^5)\gamma_0\Lambda_{\mathbf{p}_3}^-\sum_{r_3}\mathscr{P}_{\mathbf{p}_3,r_3}^+ G_{+,r_3,s}^{>,<}(P_3)\gamma^\nu \\
&\times\ (1-\gamma^5)\gamma_0\Lambda_{\mathbf{p}_2}^-\sum_{r_2}\mathscr{P}_{\mathbf{p}_2,r_2}^+ G_{+,r_2,u}^{<,>}(P_2)\Big].
\end{aligned}
\tag{2.11}
$$

This can be rewritten in an equivalent form as

$$
\Pi_{\mu\nu}^{<,>} = -\frac{ie^2 V_{us}^2}{4\sin^2\theta_W}\int\frac{d^4 P_2}{(2\pi)^4}\sum_{r_2,r_3}\mathscr{T}_{\mu\nu}^{r_3 r_2}(\hat{\mathbf{p}}_3,\hat{\mathbf{p}}_2)G_{+,r_3,s}^{>,<}(P_3)G_{+,r_2,u}^{<,>}(P_2).
\tag{2.12}
$$

where, by definition, the tensor $\mathscr{T}_{\mu\nu}^{rr'}(\hat{\mathbf{p}},\hat{\mathbf{p}}')$ is given by the following trace (in color and Dirac spaces):

$$
\mathscr{T}_{\mu\nu}^{rr'}(\hat{\mathbf{p}},\hat{\mathbf{p}}') = \mathrm{Tr}[\gamma^\mu(1-\gamma^5)\gamma_0\Lambda_{\mathbf{p}}^-\mathscr{P}_{\mathbf{p},r}^+\gamma^\nu(1-\gamma^5)\gamma_0\Lambda_{\mathbf{p}'}^-\mathscr{P}_{\mathbf{p}',r'}^+].
\tag{2.13}
$$

This trace was calculated for each of the four spin-one color superconducting phases in Ref. [56]. For convenience, the corresponding results are also quoted in Appendix A.1.

Finally, by making use of Eqs. (1.29) and (1.30), we arrive at the following expression for the W-boson polarization tensor:

$$
\begin{aligned}
\Pi_{\mu\nu}^{<,>} &= \frac{i\pi e^2 V_{us}^2}{2\sin^2\theta_W}\int\frac{d^3\mathbf{p}_2}{(2\pi)^3}\sum_{r_2,r_3,e_1,e_2}\mathscr{T}_{\mu\nu}^{r_3 r_2}(\hat{\mathbf{p}}_3,\hat{\mathbf{p}}_2)B_{\mathbf{p}_3,r_3,s}^{e_1}B_{\mathbf{p}_2,r_2,u}^{e_2} \\
&\times\ f(\pm e_1\varepsilon_{\mathbf{p}_3,r_3,s})f(\mp e_2\varepsilon_{\mathbf{p}_2,r_2,u})\delta(q_0+\delta\mu-e_1\varepsilon_{\mathbf{p}_3,r_3,s}+e_2\varepsilon_{\mathbf{p}_2,r_2,u}).
\end{aligned}
\tag{2.14}
$$

Here we denote $\delta\mu \equiv \mu_s - \mu_d$ and assume that the upper (lower) sign corresponds to $\Pi^<$ ($\Pi^>$). It should be mentioned that one of the δ-functions was used to perform the integration over $p_{2,0}$.

2.2   Calculation of the rate

In this section we derive a general expression for the net rate of the d-quark production in spin-one color superconducting quark matter close to chemical equilibrium. The corresponding rate is formally defined by Eq. (2.8). By making use of the quark prop-

agators and the W-boson polarization tensor, derived in the previous section, we obtain

$$
\begin{aligned}
\Gamma_d &= \frac{ie^2 V_{ud}^2}{16 M_W^4 \sin^2\theta_W} \int \frac{d^4 P_1}{(2\pi)^4} \int \frac{d^4 P_4}{(2\pi)^4} \sum_{r_1,r_4} \mathscr{T}_{r_4 r_1}^{\mu\nu}(\hat{\mathbf{p}}_4, \hat{\mathbf{p}}_1) \\
&\times \left[G_{+,r_1,d}^{>}(P_1) G_{+,r_4,u}^{<}(P_4) \Pi_{\mu\nu}^{>}(Q) - G_{+,r_4,u}^{>}(P_4) G_{+,r_1,d}^{<}(P_1) \Pi_{\mu\nu}^{<}(Q) \right] (2.15)
\end{aligned}
$$

where we used the following results for the traces:

$$
\mathrm{Tr}\left(S_d^{>}(P_1) \Gamma_{ud,-}^{\mu} S_u^{<}(P_4) \Gamma_{ud,+}^{\nu} \right) = \frac{e^2 V_{ud}^2}{4\sin^2\theta_W} \sum_{r_1,r_4} \mathscr{T}_{r_4 r_1}^{\mu\nu}(\hat{\mathbf{p}}_4, \hat{\mathbf{p}}_1) G_{+,r_1,d}^{>}(P_1) G_{+,r_4,u}^{<}(P_4),
$$

$$(2.16)$$

$$
\mathrm{Tr}\left(\Gamma_{ud,-}^{\mu} S_u^{>}(P_4) \Gamma_{ud,+}^{\nu} S_d^{<}(P_1) \right) = \frac{e^2 V_{ud}^2}{4\sin^2\theta_W} \sum_{r_1,r_4} \mathscr{T}_{r_4 r_1}^{\mu\nu}(\hat{\mathbf{p}}_4, \hat{\mathbf{p}}_1) G_{+,r_4,u}^{>}(P_4) G_{+,r_1,d}^{<}(P_1).
$$

$$(2.17)$$

As in the calculation of the polarization tensor, the anomalous (off-diagonal) Nambu-Gorkov components of quark propagators did not contribute to these traces. This is the consequence of the specific flavor structure of the weak interaction vertices (2.4).

After making use of Eqs. (1.29), (1.30) and (2.14), we obtain

$$
\begin{aligned}
\Gamma_d &= 2^7 \pi^4 G_F^2 V_{ud}^2 V_{us}^2 \sum_{r_1 r_2 r_3 r_4} \sum_{e_1 e_2 e_3 e_4} \int \frac{d^3\mathbf{p}_1}{(2\pi)^3} \frac{d^3\mathbf{p}_2}{(2\pi)^3} \frac{d^3\mathbf{p}_3}{(2\pi)^3} \frac{d^3\mathbf{p}_4}{(2\pi)^3} (1 - \hat{\mathbf{p}}_1 \cdot \hat{\mathbf{p}}_2) \\
&\times (1 - \hat{\mathbf{p}}_3 \cdot \hat{\mathbf{p}}_4) \omega_{r_4 r_1}(\hat{\mathbf{p}}_4, \hat{\mathbf{p}}_1) \omega_{r_3 r_2}(\hat{\mathbf{p}}_3, \hat{\mathbf{p}}_2) B_{\mathbf{p}_1,r_1,d}^{e_1} B_{\mathbf{p}_2,r_2,u}^{e_2} B_{\mathbf{p}_3,r_3,s}^{e_3} B_{\mathbf{p}_4,r_4,u}^{e_4} \\
&\times \delta(\mathbf{p}_1 + \mathbf{p}_2 - \mathbf{p}_3 - \mathbf{p}_4) \delta(e_1 \varepsilon_{\mathbf{p}_1,r_1,d} + e_2 \varepsilon_{\mathbf{p}_2,r_2,u} - e_3 \varepsilon_{\mathbf{p}_3,r_3,s} - e_4 \varepsilon_{\mathbf{p}_4,r_4,u} + \delta\mu) \\
&\times \left[f(e_1 \varepsilon_{\mathbf{p}_1,r_1,d}) f(e_2 \varepsilon_{\mathbf{p}_2,r_2,u}) f(-e_3 \varepsilon_{\mathbf{p}_3,r_3,s}) f(-e_4 \varepsilon_{\mathbf{p}_4,r_4,u}) - f(-e_1 \varepsilon_{\mathbf{p}_1,r_1,d}) \right. \\
&\times \left. f(-e_2 \varepsilon_{\mathbf{p}_2,r_2,u}) f(e_3 \varepsilon_{\mathbf{p}_3,r_3,s}) f(e_4 \varepsilon_{\mathbf{p}_4,r_4,u}) \right].
\end{aligned}
$$

$$(2.18)$$

In derivation, we used the definition of the Fermi constant in terms of the W-boson mass,

$$
G_F = \frac{e^2}{4\sqrt{2}\sin^2\theta_W M_W^2} \tag{2.19}
$$

and the following Lorentz contraction:

$$
\mathscr{T}_{r_4 r_1}^{\mu\nu}(\hat{\mathbf{p}}_4, \hat{\mathbf{p}}_1) \mathscr{T}_{\mu\nu}^{r_3 r_2}(\hat{\mathbf{p}}_3, \hat{\mathbf{p}}_2) = 16(1 - \hat{\mathbf{p}}_1 \cdot \hat{\mathbf{p}}_2)(1 - \hat{\mathbf{p}}_3 \cdot \hat{\mathbf{p}}_4) \omega_{r_4 r_1}(\hat{\mathbf{p}}_4, \hat{\mathbf{p}}_1) \omega_{r_3 r_2}(\hat{\mathbf{p}}_3, \hat{\mathbf{p}}_2), \quad (2.20)
$$

where $\omega_{rr'}(\hat{\mathbf{p}}, \hat{\mathbf{p}}')$ denotes a color trace that involves a pair of quasiparticles (r and r') with the given directions of their three-momenta ($\hat{\mathbf{p}}$ and $\hat{\mathbf{p}}'$) in a specific spin-one color superconducting phase. The corresponding traces for all four phases are listed in Appendix A.1.

Formally, the expression in Eq. (2.18) gives the net rate of the d-quark production in quark matter away from chemical equilibrium. The first term in the brackets describes the production of d-quarks due to $s + u \to u + d$, while the second one describes the annihilation of d-quarks due to $u + d \to s + u$.

Here it might be instructive to note that the above expression for the rate Γ_d resembles the general result for the net rate of the d-quark production in the normal phase of strange quark matter [103]. The key difference comes from the presence of the Bogoliubov coefficients $B_{\mathbf{p}, r, f}$ and the $\omega_{rr'}(\hat{\mathbf{p}}, \hat{\mathbf{p}}')$ functions that account for a non-trivial quark structure of the quasiparticles in spin-one color superconductors. Naturally, when such quasiparticles are the asymptotic states for the weak processes, the amplitude is not the same as in the normal phase.

The degree of departure from β-equilibrium and, thus, the net rate is controlled by the parameter $\delta\mu = \mu_s - \mu_d$. When $\delta\mu = 0$, the expression in the square brackets of Eq. (2.18) vanishes and $\Gamma_d = 0$. When $\delta\mu \neq 0$, on the other hand, one has

$$\Gamma_d \simeq \lambda \delta\mu \tag{2.21}$$

to leading order in small $\delta\mu$. Note that the overall sign was chosen so that λ is positive definite. (Recall that a positive $\delta\mu$ means an excess of strange quarks, which should drive a net production of d-quarks, while a negative $\delta\mu$ means a deficit of strange quarks, which will be produced by annihilating some d-quarks.)

From the general expression in Eq. (2.18), we derive

$$
\begin{aligned}
\lambda \;=\; & \frac{5\lambda_0}{2^{11}\pi^5\mu^5 T^3} \sum_{r_1 r_2 r_3 r_4} \sum_{e_1 e_2 e_3 e_4} \int d^3\mathbf{p}_1 d^3\mathbf{p}_2 d^3\mathbf{p}_3 d^3\mathbf{p}_4 (1-\hat{\mathbf{p}}_1\cdot\hat{\mathbf{p}}_2)(1-\hat{\mathbf{p}}_3\cdot\hat{\mathbf{p}}_4) \\
\times \;& \omega_{r_4 r_1}(\hat{\mathbf{p}}_4,\hat{\mathbf{p}}_1)\omega_{r_3 r_2}(\hat{\mathbf{p}}_3,\hat{\mathbf{p}}_2)B^{e_1}_{\mathbf{p}_1,r_1,d}B^{e_2}_{\mathbf{p}_2,r_2,u}B^{e_3}_{\mathbf{p}_3,r_3,s}B^{e_4}_{\mathbf{p}_4,r_4,u}\delta(\mathbf{p}_1+\mathbf{p}_2-\mathbf{p}_3-\mathbf{p}_4) \\
\times \;& \delta(e_1\varepsilon_{\mathbf{p}_1,r_1,d}+e_2\varepsilon_{\mathbf{p}_2,r_2,u}-e_3\varepsilon_{\mathbf{p}_3,r_3,s}-e_4\varepsilon_{\mathbf{p}_4,r_4,u}) \\
\times \;& f(-e_1\varepsilon_{\mathbf{p}_1,r_1,d})f(-e_2\varepsilon_{\mathbf{p}_2,r_2,u})f(e_3\varepsilon_{\mathbf{p}_3,r_3,s})f(e_4\varepsilon_{\mathbf{p}_4,r_4,u}).
\end{aligned} \tag{2.22}
$$

where

$$
\lambda_0 = \frac{64 G_F^2 V_{ud}^2 V_{us}^2}{5\pi^3}\mu^5 T^2 \tag{2.23}
$$

is the corresponding λ-rate in the normal phase of strange quark matter [103].

2.2.1 Analysis of the rate in CSL phase

Out of the four spin-one color superconducting phases studied in this thesis, the CSL phase is special. This is the only phase in which the dispersion relations of quasiparticles are isotropic. As a result, the corresponding rate is the easiest to calculate. In this subsection, we analyze the λ-rate in the CSL phase in detail.

Let us start by noting that the explicit form of the $\omega_{rr'}(\hat{\mathbf{p}},\hat{\mathbf{p}}')$-functions in the CSL phase is given by

$$
\omega_{11}(\hat{\mathbf{p}},\hat{\mathbf{p}}') = 1 + \frac{1}{4}(1+\hat{\mathbf{p}}\cdot\hat{\mathbf{p}}')^2, \tag{2.24}
$$

$$
\omega_{12}(\hat{\mathbf{p}},\hat{\mathbf{p}}') = \omega_{21}(\hat{\mathbf{p}},\hat{\mathbf{p}}') = 1 - \frac{1}{4}(1+\hat{\mathbf{p}}\cdot\hat{\mathbf{p}}')^2, \tag{2.25}
$$

$$
\omega_{22}(\hat{\mathbf{p}},\hat{\mathbf{p}}') = \frac{1}{4}(1+\hat{\mathbf{p}}\cdot\hat{\mathbf{p}}')^2. \tag{2.26}
$$

(See Appendix A.1 and Ref. [56].) By making use of these expressions and introducing the following notation for the angular integrals:

$$
\begin{aligned}
F_{r_1 r_2 r_3 r_4} \;=\; & \int d\Omega_1 \int d\Omega_2 \int d\Omega_3 \int d\Omega_4 \,(1-\hat{\mathbf{p}}_3\cdot\hat{\mathbf{p}}_4)(1-\hat{\mathbf{p}}_1\cdot\hat{\mathbf{p}}_2)\omega_{r_4 r_1}(\hat{\mathbf{p}}_4,\hat{\mathbf{p}}_1) \\
\times \;& \omega_{r_3 r_2}(\hat{\mathbf{p}}_3,\hat{\mathbf{p}}_2)\delta(\mathbf{p}_1+\mathbf{p}_2-\mathbf{p}_3-\mathbf{p}_4),
\end{aligned} \tag{2.27}
$$

35

we arrive at the following representation for the λ-rate in the CSL phase:

$$
\begin{aligned}
\lambda^{(\text{CSL})} \;=\; & \frac{5\lambda_0\mu^3}{2^{11}\pi^5 T^3} \sum_{r_1 r_2 r_3 r_4} \sum_{e_1 e_2 e_3 e_4} \int_0^\infty dp_1 \int_0^\infty dp_2 \int_0^\infty dp_3 \int_0^\infty dp_4 \, F_{r_1 r_2 r_3 r_4} \\
& \times \; B_{\mathbf{p}_1,r_1,d}^{e_1} B_{\mathbf{p}_2,r_2,u}^{e_2} B_{\mathbf{p}_3,r_3,s}^{e_3} B_{\mathbf{p}_4,r_4,u}^{e_4} f(-e_1\varepsilon_{\mathbf{p}_1,r_1,d}) f(-e_2\varepsilon_{\mathbf{p}_2,r_2,u}) f(e_3\varepsilon_{\mathbf{p}_3,r_3,s}) \\
& \times \; f(e_4\varepsilon_{\mathbf{p}_4,r_4,u}) \delta(e_1\varepsilon_{\mathbf{p}_1,r_1,d} + e_2\varepsilon_{\mathbf{p}_2,r_2,u} - e_3\varepsilon_{\mathbf{p}_3,r_3,s} - e_4\varepsilon_{\mathbf{p}_4,r_4,u}). \quad (2.28)
\end{aligned}
$$

Here we took into account that, to leading order in inverse powers of μ, the absolute values of the quark three-momenta can be approximated by μ. In the same approximation, the explicit form of functions $F_{r_1 r_2 r_3 r_4}$ are given in Appendix A.2. All of them are proportional to $1/\mu^3$. This factor cancels out with the overall μ^3 in Eq. (2.28). In order to perform the remaining numerical integrations, it is convenient to introduce new dimensionless integration variables $x_i = (p_i - \mu)/T$ instead of p_i ($i = 1,2,3,4$). The integration over x_4 is done explicitly by making use of the δ-function. The remaining three-dimensional integration is done numerically, using a Monte-Carlo method. One finds that the ratio $\lambda^{(\text{CSL})}/\lambda_0$ is a function of a single dimensionless ratio, ϕ/T.

Before proceeding to the numerical results, it is instructive to analyze the limiting case of low temperatures (or alternatively very large ϕ/T). In this limit, only the ungapped $r = 2$ quasiparticle modes should contribute to the rate. The corresponding contribution is easy to obtain analytically, i.e.,

$$
\lambda^{(\text{CSL})} \;\simeq\; \frac{\lambda_0 F_{2222}}{\sum_{r_1 r_2 r_3 r_4} F_{r_1 r_2 r_3 r_4}} = \frac{928}{27027}\lambda_0 \approx 0.034\lambda_0, \quad \text{for} \quad \frac{\phi}{T} \to \infty. \quad (2.29)
$$

The subleading correction to this result is suppressed by an exponentially small factor $\exp(-\sqrt{2}\phi/T)$. (Note that $\sqrt{2}$ in the exponent is connected with the conventional choice of the CSL gap, which is $\sqrt{2}\phi$ rather than ϕ.)

It might be instructive to mention that the asymptotic value in Eq. (2.29) is substantially smaller than $\lambda_0/9$, which is the corresponding contribution of a single ungapped mode in the normal phase. The additional suppression comes from the functions $\omega_{22}(\hat{\mathbf{p}}_4,\hat{\mathbf{p}}_1)$ and $\omega_{22}(\hat{\mathbf{p}}_3,\hat{\mathbf{p}}_2)$ which modify the amplitude of the weak processes

with respect to the normal phase. Except for the special case of collinear processes (i.e., $\hat{\mathbf{p}}_4$ parallel to $\hat{\mathbf{p}}_1$ and $\hat{\mathbf{p}}_3$ parallel to $\hat{\mathbf{p}}_2$), the corresponding ω-functions are less than 1, see Eq. (2.26). Interestingly, this kind of suppression is a unique property of the non-leptonic rates and is not seen in analogous Urca rates because the latter are dominated by the collinear processes [56, 65].

All our numerical results for the λ-rates as a function of ϕ/T are shown in Fig. 2.2 [104]. In the case of the CSL phase (black points and the interpolating line in Fig. 2.2), we used the Mathematica's adaptive quasi-Monte-Carlo method to calculate the λ-rate. In order to improve the efficiency of the method, we partitioned the range of integration for each of the three dimensionless integration variables $x_i = (p_i - \mu)/T$ into several (up to 6) non-overlapping regions. This approach insures that the main contribution, coming from a close neighborhood of the Fermi sphere, is not lost in the integration over a formally very large phase space.

As seen from Fig. 2.2, the numerical results smoothly interpolate between the value of the rate in the normal phase λ_0 and the asymptotic value of the rate due to the CSL ungapped modes, given by Eq. (2.29).

2.2.2   Analysis of the rate in polar phase

Unlike the CSL phase, the polar phase is not isotropic. However, it is the simplest one among the other three phases. While the dispersions relations of its quasiparticles depend on the angle $\theta_{\mathbf{p}}$ between the momentum $\mathbf{p}$ and a fixed z-drection, its $\omega_{rr'}(\hat{\mathbf{p}}, \hat{\mathbf{p}}')$-functions are independent of the quasiparticle momenta, i.e.,

$$\omega_{rr'}(\hat{\mathbf{p}}, \hat{\mathbf{p}}') = n_r \delta_{rr'}, \tag{2.30}$$
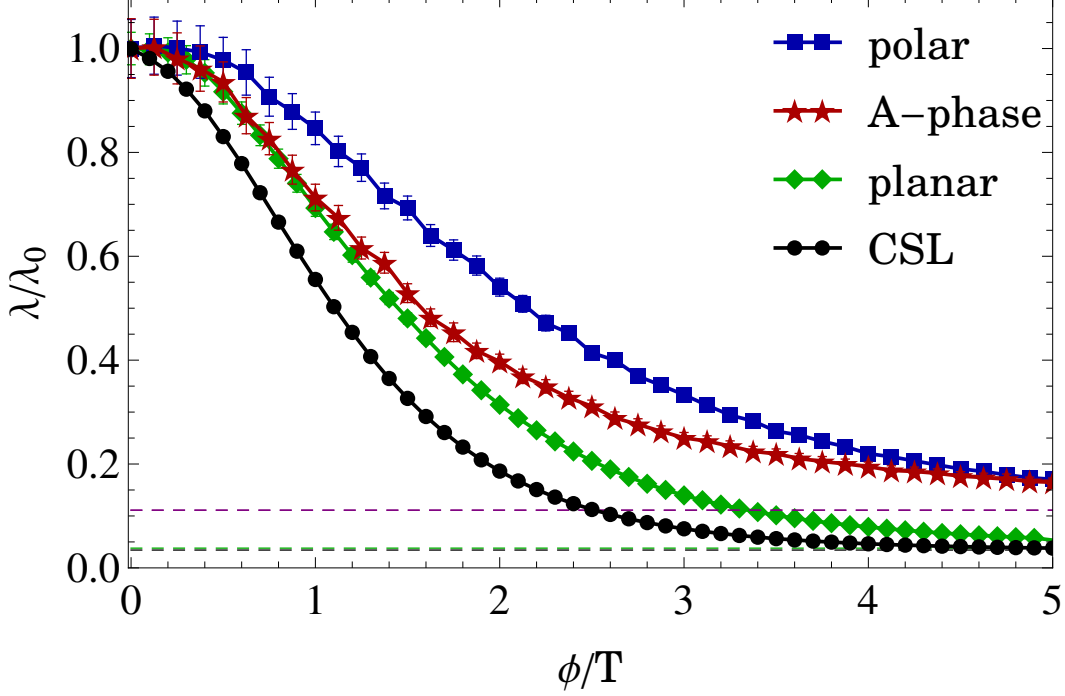
Figure 2.2: Numerical results for the λ-rate in four different phases of spin-one color superconducting strange quark matter [104]. The error bars show the statistical error estimates in the Monte-Carlo calculation of the rates. The horizontal dashed lines correspond to the contributions of the ungapped modes in the limit of large ϕ/T (or equivalently the limit of low temperatures).

with $n_1 = 2$ and $n_2 = 1$, see Appendix A.1. Taking this into account, the corresponding λ-rate takes a simple form:

$$
\begin{aligned}
\lambda^{\text{(polar)}} &= \frac{5\lambda_0}{2^{11}\pi^5\mu^5 T^3} \sum_{r_1 r_2} n_{r_1} n_{r_2} \sum_{e_1 e_2 e_3 e_4} \int d^3\mathbf{p}_1 d^3\mathbf{p}_2 d^3\mathbf{p}_3 d^3\mathbf{p}_4 (1 - \hat{\mathbf{p}}_1 \cdot \hat{\mathbf{p}}_2) \\
&\times \quad (1 - \hat{\mathbf{p}}_3 \cdot \hat{\mathbf{p}}_4)\delta(\mathbf{p}_1 + \mathbf{p}_2 - \mathbf{p}_3 - \mathbf{p}_4)B^{e_1}_{\mathbf{p}_1,r_1,d}B^{e_2}_{\mathbf{p}_2,r_2,u}B^{e_3}_{\mathbf{p}_3,r_2,s}B^{e_4}_{\mathbf{p}_4,r_1,u} \\
&\times \quad f(-e_1\varepsilon_{\mathbf{p}_1,r_1,d})f(-e_2\varepsilon_{\mathbf{p}_2,r_2,u})f(e_3\varepsilon_{\mathbf{p}_3,r_2,s})f(e_4\varepsilon_{\mathbf{p}_4,r_1,u}) \\
&\times \quad \delta(e_1\varepsilon_{\mathbf{p}_1,r_1,d} + e_2\varepsilon_{\mathbf{p}_2,r_2,u} - e_3\varepsilon_{\mathbf{p}_3,r_2,s} - e_4\varepsilon_{\mathbf{p}_4,r_1,u}).
\end{aligned}
\tag{2.31}
$$

By making use of the first δ-function, we easily perform the integration over $\mathbf{p}_4$. We can also perform the integration over one of the remaining polar coordinates. This is possible because the integrand depends only on the two independent combinations of the polar angles, i.e., $\tilde{\varphi}_1 = \varphi_1 - \varphi_3$ and $\tilde{\varphi}_2 = \varphi_2 - \varphi_3$. By using $\tilde{\varphi}_1$ and $\tilde{\varphi}_2$ as new in-

38

tegration variables (for simplicity of notation, the tildes are dropped in the following), we see that the integrand is independent of the variable φ_3. Finally, by approximating $p_1^2 p_2^2 p_3^2 \simeq \mu^6$ in the integration measure, we rewrite the expression for the rate as follows:

$$
\begin{aligned}
\lambda^{(\text{polar})} \simeq \ & \frac{5\lambda_0 \mu}{2^{18} \pi^4 T} \sum_{r_1 r_2} n_{r_1} n_{r_2} \int_{-\infty}^{\infty} dx_1 \int_{-\infty}^{\infty} dx_2 \int_{-\infty}^{\infty} dx_3 \int_{-1}^{1} d\xi_1 \int_{-1}^{1} d\xi_2 \int_{-1}^{1} d\xi_3 \\
& \int_0^{2\pi} d\varphi_1 \int_0^{2\pi} d\varphi_2 \sum_{e_1 e_2 e_3 e_4} B^{e_1}_{x_1,\xi_1,r_1} B^{e_2}_{x_2,\xi_2,r_2} B^{e_3}_{x_3,\xi_3,r_2} B^{e_4}_{x_4,\xi_4,r_1} \\
& \times \frac{(1 - \cos\theta_{12})(1 - \cos\theta_{34})}{\cosh(\frac{1}{2}\varepsilon_{x_1,\xi_1,r_1})\cosh(\frac{1}{2}\varepsilon_{x_2,\xi_2,r_2})\cosh(\frac{1}{2}\varepsilon_{x_3,\xi_3,r_2})\cosh(\frac{1}{2}\varepsilon_{x_4,\xi_4,r_1})} \\
& \times \ \delta(e_1 \varepsilon_{x_1,\xi_1,r_1} + e_2 \varepsilon_{x_2,\xi_2,r_2} - e_3 \varepsilon_{x_3,\xi_3,r_2} - e_4 \varepsilon_{x_4,\xi_4,r_1}),
\end{aligned}
\tag{2.32}
$$

where the new integration variables are $x_i = (p_i - \mu)/T$ and $\xi_i = \cos\theta_{\mathbf{p}_i}$. By definition, the dimensionless energy is

$$
\varepsilon_{x,\xi,r} = \sqrt{x^2 + |\phi/T|^2 \lambda_{\xi,r}},
\tag{2.33}
$$

with $\lambda_{\xi,1} = 1 - \xi^2$ and $\lambda_{\xi,2} = 0$, and the new Bogoliubov coefficients are

$$
B^e_{x,\xi,r} = \frac{1}{2}\left(1 - e\frac{x}{\varepsilon_{x,\xi,r}}\right).
\tag{2.34}
$$

Note that the expressions for x_4, ξ_4 and $\cos\theta_{34}$ in Eq. (2.32) are given by

$$
\begin{aligned}
x_4 &= \frac{p_4 - \mu}{T}, \\
\xi_4 &= \frac{p_1 \xi_1 + p_2 \xi_2 - p_3 \xi_3}{p_4}, \\
\cos\theta_{34} &= \frac{p_1 \cos\theta_{13} + p_2 \cos\theta_{23} - p_3}{p_4},
\end{aligned}
\tag{2.35}
$$

where $p_4 = |\mathbf{p}_1 + \mathbf{p}_2 - \mathbf{p}_3|$ is a function of x_i ($i = 1, 2, 3$) and the three cosine functions,

$$
\begin{aligned}
\cos\theta_{12} &= \xi_1 \xi_2 + \sqrt{1 - \xi_1^2}\sqrt{1 - \xi_2^2}\cos(\varphi_1 - \varphi_2), \\
\cos\theta_{13} &= \xi_1 \xi_3 + \sqrt{1 - \xi_1^2}\sqrt{1 - \xi_3^2}\cos(\varphi_1), \\
\cos\theta_{23} &= \xi_2 \xi_3 + \sqrt{1 - \xi_2^2}\sqrt{1 - \xi_3^2}\cos(\varphi_2).
\end{aligned}
\tag{2.36}
$$

In the calculation, we used a customized Monte-Carlo method in order to improve the statistical error of the integration over x_i (with $i = 1,2,3$). To this end, we used a special type of importance sampling, which is motivated by the fact that the main contribution to the rate should come from the region near the Fermi surface. In order to implement this, we utilized random variables distributed according to the Gaussian distribution [105]:

$$P(x) = \frac{1}{\sqrt{2\pi\sigma^2}} \exp\left(-\frac{(x-x_0)^2}{2\sigma^2}\right), \tag{2.37}$$

where x_0 and σ are the mean and the width of the distribution, respectively. This was applied to the numerical integration over the dimensionless variables $x_i = (p_i - \mu)/T$ ($i = 1,2,3$), in which case we took $x_0 = 0$ and $\sigma = 3$. In order to generate independent variables (e.g., x_1 and x_2), distributed according to Eq. (2.37), we applied the Box-Muller transform,

$$x_1 = x_0 + \sigma\sqrt{-2\ln u_1}\cos(2\pi u_2), \tag{2.38}$$

$$x_2 = x_0 + \sigma\sqrt{-2\ln u_1}\sin(2\pi u_2), \tag{2.39}$$

where u_1 and u_2 are two independent variables, uniformly distributed in the range from 0 to 1.

In our numerical calculation, we also used a Gaussian function to approximate the δ-function responsible for the energy conservation in the expression for the rate (2.32). For this purpose, we used the width of the distribution $\sigma_0 = 0.2$. This appeared to be sufficiently small to avoid strong violations of the energy conservation in the weak processes and, at the same time, sufficiently large to use in a Monte-Carlo integration with the number of (eight-dimensional) random points on the order of 10^6 (in a Mathematica code) or 10^7 (in a Fortran/C++ code).

The numerical results for the λ-rate in the polar phase are shown by squares (and the interpolating line) in Fig. 2.2. At vanishing ϕ/T, the rate coincides with

that in the normal phase. At asymptotically large value of ϕ/T, on the other hand, the rate approaches $\lambda_0/9$. This value is marked by the purple dashed line in the figure. Theoretically, the rate is dominated by the ungapped modes ($r_1 = r_2 = 2$) in the $\phi/T \to \infty$ limit. The corresponding contribution can be obtained by analytical methods as follows. We start by pointing that the Bogoliubov coefficients for the ungapped modes are equal to the unit step functions: $B^{e_i}_{x_i, \xi_i, 2} \equiv \Theta(-e_i x_i)$, where by definition $\Theta(x) = 1$ for $x \geq 0$ and $\Theta(x) = 0$ otherwise. Since these Bogoliubov coefficients are nonzero only for $e_i = \text{sign}(-x_i)$, each sums over e_i effectively reduces to a single contribution. By taking this into account and making use of the result for the angular integration, K_0, defined in Appendix A.2, we derive

$$
\begin{aligned}
\lambda^{(\text{polar})}_{\text{unpaired}} &\simeq \frac{\lambda_0}{6\pi^2} \int_{-\infty}^{\infty} dx_1 \int_{-\infty}^{\infty} dx_2 \int_{-\infty}^{\infty} dx_3 \int_{-\infty}^{\infty} dx_4 \\
&\times \frac{\delta(-x_1 - x_2 + x_3 + x_4)}{(e^{x_1} + 1)(e^{x_2} + 1)(e^{-x_3} + 1)(e^{-x_4} + 1)} \\
&= \frac{1}{9}\lambda_0.
\end{aligned}
\tag{2.40}
$$

It should be noted that the numerical results for the polar phase in Fig. 2.2 approach this asymptotic value very slowly. We can speculate that this indicates a weak (probably, power-law) suppression of the contribution of the gapped (mixed with ungapped) modes to the rate. The key feature responsible for this behavior in the polar phase is the presence of gapless nodes at $\theta_\mathbf{p} = 0$ and $\theta_\mathbf{p} = \pi$ in the dispersion relation of the gapped modes. As we shall see below, the same qualitative property is shared by the A-phase, whose gapped modes also have a node at $\theta_\mathbf{p} = \pi$. In contrast, the rates in the CSL and planar phases, whose gapped modes have no gapless nodes, show asymptotes that are consistent with the rapid, exponential approach to their asymptotic values.

2.2.3 Analysis of the rate in A-phase

The analysis in the A-phase of spin-one color superconducting matter can be performed along the same lines as in the polar phase. The apparent complication of the A-phase

41

is the existence of three, rather than two distinct quasiparticle excitations. However, it appears that the contributions of the two gapped modes ($r = 1, 2$) can be replaced by a single contribution of a modified mode with the energy $\varepsilon_{\mathbf{p}} = \sqrt{(p - \mu)^2 + |\phi|^2 \lambda_{\mathbf{p}}}$ where $\lambda_{\mathbf{p}} \equiv (1 + \cos \theta_{\mathbf{p}})^2$ (cf. the dispersion relations of the modes $r = 1, 2$ in Tab. 1.1). This alternative representation is possible because of the special, separable structure of the corresponding $\omega_{rr'}(\hat{\mathbf{p}}, \hat{\mathbf{p}}')$ functions in the A-phase. As seen from the expressions in Eq. (A.7), the mode $r = 1$ contributes only when $\cos \theta_{\mathbf{p}}$ of the corresponding quasiparticle is positive, while the mode $r = 2$ contributes only when $\cos \theta_{\mathbf{p}}$ is negative. Then, when the contributions are nonvanishing, one always gets $\omega_{rr'}(\hat{\mathbf{p}}, \hat{\mathbf{p}}') = 2$. By also noting that the corresponding eigenvalues

$$\lambda_{\mathbf{p},1} = (1 + |\cos \theta_{\mathbf{p}}|)^2 \quad \text{for} \quad \cos \theta_{\mathbf{p}} > 0 \tag{2.41}$$

and

$$\lambda_{\mathbf{p},2} = (1 - |\cos \theta_{\mathbf{p}}|)^2 \quad \text{for} \quad \cos \theta_{\mathbf{p}} < 0 \tag{2.42}$$

formally take the same form, i.e., $\lambda_{\mathbf{p}} \equiv (1 + \cos \theta_{\mathbf{p}})^2$, we conclude that the sum over the original modes $r = 1, 2$ in the rate can indeed be replaced by a single contribution of the modified mode as defined above. By making use of this observation, the general expression for the rate in the A-phase takes the form, which is similar to that in the polar phase, see Eq. (2.31), but with a different dispersion relation of the (modified) gapped mode.

By using a Monte-Carlo algorithm as in the previous case, we perform a numerical calculation of the λ-rate in the A-phase. The corresponding results are shown by stars (and the interpolating line) in Fig. 2.2. In the limit of large ϕ/T, the rate is saturated by the contribution of ungapped modes, which is the same as in the polar phase, namely $\lambda_0/9$. The derivation of this asymptotic expression is the same as in the polar phase. The corresponding value is marked by the dashed line in the figure. A slow (probably, power-law) approach of the asymptotic value at $\phi/T \to \infty$ is again

42

associated with the presence of a gapless node (at $\theta_{\mathbf{p}} = \pi$) in the dispersion relation of the (modified) gapped quasiparticles.

2.2.4 Analysis of the rate in planar phase

The calculation of the rate in the planar case requires the largest amount of computer time. One of the main reasons for that is the much more complicated expressions for the $\omega_{rr'}(\hat{\mathbf{p}}, \hat{\mathbf{p}}')$-functions (see Appendix A.1). The numerical results for the λ-rate in the planar phase are shown by diamonds (and the interpolating line) in Fig. 2.2. The asymptotic value of the rate at large ϕ/T was extracted only numerically. By taking into account possible systematic errors (e.g., due to the overall normalization of the rate that may differ by up to 15% from the analytical estimate (2.23) in the normal phase), we estimate $\lambda^{(\mathrm{planar})} \simeq (0.038 \pm 0.003)\lambda_0$ for $\phi/T \to \infty$. Note that this is smaller than $\lambda_0/9$, which is the contribution of a single mode in the normal phase. As in the CSL phase, in the planar phase the additional suppression comes from the ω-functions for the ungapped modes.

2.3 Discussion

In this chapter we derived the near-equilibrium rates of the net d-quark production (or equivalently the λ-rates) due to the non-leptonic weak processes (i.e., the difference of the rates of $u + d \to u + s$ and $u + s \to u + d$) in spin-one color-superconducting strange quark matter at high density [106]. The main numerical results are presented in Fig. 2.2.

In the limit of $\phi/T = 0$, which is same as the normal (unpaired) phase of strange quark matter, our results reproduce the known result of Ref. [103]. The effect of color superconductivity is to suppress these rates. The degree of the suppression depends on the details of the specific spin-one phases. To large extent, this is controlled by the value of the energy gap (more precisely, ϕ/T) as well as its functional dependence on the direction of the quasiparticle momentum. At very large ϕ/T (or equivalently in the

limit of low temperatures), the λ-rates approach fixed values, which are determined by the contribution of the ungapped modes alone. The corresponding limiting value is the smallest in the CSL phase. It is less than a third of the "canonical" value $\lambda_0/9$ due to a single ungapped mode in the normal phase of matter. The additional suppression comes from the modification of the quasiparticles due to color superconductivity. A similar observation applies to the planar phase. The rates in the other two phases, i.e., the polar and A-phase, approach the asymptotic values equal to $\lambda_0/9$.

The numerical results for the λ-rates in Fig. 2.2 also indicate that the asymptotic approach to the limiting values can be qualitatively different in spin-one color super-conducting phases. In the case of the polar and A-phase, the approach follows a power law. In contrast, the approach appears to be exponential in the case of the CSL and planar phase. This qualitative difference can be easily understood. The power law is the consequence of the presence of gapless nodes in the dispersion relations of the gapped quasiparticles in the polar and A-phase (the nodes are located at $\theta_{\mathbf{p}} = 0$ and $\theta_{\mathbf{p}} = \pi$ in the polar phase, and at $\theta_{\mathbf{p}} = \pi$ in the A-phase). In the CSL and planar phase, the approach to the asymptotic value at $\phi/T \to \infty$ is exponential because no gapless nodes are found in their gapped quasiparticles. (Note that a similar observation regarding the rates of the semi-leptonic processes was made in Ref. [56, 65].)

The results for the rates of non-leptonic weak processes, presented here, is an important ingredient for the calculation of the bulk viscosity of spin-one color-superconducting strange quark matter, which we will discuss in the next chapter.

CHAPTER 3

BULK VISCOSITY OF SPIN-ONE COLOR SUPERCONDUCTING STRANGE

QUARK MATTER

In this chapter we calculate the bulk viscosity of spin-one color superconducting strange quark matter. The interplay of Urca and non-leptonic processes will be considered here.

3.1 Formalism

In order to calculate the bulk viscosity in the presence of several types of active weak processes, we follow the general formalism of Ref. [77]. We assume that small oscillations of the quark matter density are described by $\delta n = \delta n_0 \operatorname{Re}(e^{i\omega t})$ where δn_0 is the magnitude of the oscillations. For such a periodic process, the bulk viscosity ζ is defined as the coefficient in the expression for the energy-density dissipation averaged over one period, $\tau = 2\pi/\omega$,

$$\langle \dot{\mathscr{E}}_{\mathrm{diss}} \rangle = -\frac{\zeta}{\tau} \int_0^\tau dt \, (\nabla \cdot \vec{v})^2 , \tag{3.1}$$

where $\vec{v}$ is the hydrodynamic velocity associated with the density oscillations. By making use of the continuity equation, $\dot{n} + n\nabla \cdot \vec{v} = 0$, we derive

$$\langle \dot{\mathscr{E}}_{\mathrm{diss}} \rangle = -\frac{\zeta \omega^2}{2} \left(\frac{\delta n_0}{n} \right)^2 . \tag{3.2}$$

Such an energy-density dissipation of a pulsating hydrodynamic flow is the outcome of a net work done on a macroscopic volume over a period of the oscillation,

$$\langle \dot{\mathscr{E}}_{\mathrm{diss}} \rangle = \frac{n}{\tau} \int_0^\tau P\dot{V} dt, \tag{3.3}$$

where $V \equiv 1/n$ is the specific volume. By matching the hydrodynamic definition in Eq. (3.2) with the relation in Eq. (4.2), we derive the expression for the bulk viscosity,

$$\zeta = -\frac{2}{\omega^2} \left(\frac{n}{\delta n_0} \right)^2 \frac{n}{\tau} \int_0^\tau P\dot{V} dt. \tag{3.4}$$

The dominant mechanism behind the bulk viscosity is related to weak processes [71, 72, 73, 107]. A periodic oscillation of the density is responsible for an instantaneous

45

departure from β-equilibrium in the system. As a result, the forward and backward weak processes (e.g., $u + d \rightarrow s + u$ and $s + u \rightarrow u + d$), which have equal rates in equilibrium, become unbalanced. Their net effect is to restore the equilibrium composition. However, since the weak rates are relatively slow, a substantial time lag between the oscillations of the fermion number density (and, thus, the specific volume) and the chemical composition (and, thus, the pressure) develops. If the resulting relative phase shift of the two oscillations is $\Delta\phi$, one finds from Eqs. (4.2) and (4.6) that the corresponding energy dissipation and the bulk viscosity are proportional to $\sin\Delta\phi$. (Note that the departure from the thermal equilibrium is negligible because it is restored by strong forces on much shorter time scales.)

It should be clear that the instantaneous flavor composition in oscillating quark matter and the rate difference of the forward and backward weak processes in Fig. 1.4 are related to each other. The difference of the rates changes the composition, while the composition in turn influences the difference of rates. The corresponding dynamics can be conveniently described in terms of the time dependent deviations of the chemical potentials from their equilibrium values.

In β equilibrium, the chemical potentials of the three lightest quarks are related as follows: $\mu_s = \mu_d = \mu_u + \mu_e$. Here μ_u, μ_d and μ_s are the chemical potentials of up, down and strange quarks, while μ_e is the electron chemical potential. In pulsating matter, the instantaneous departure from equilibrium is described by the following two independent parameters:

$$\delta\mu_1 \;\equiv\; \mu_s - \mu_d = \delta\mu_s - \delta\mu_d, \tag{3.5a}$$

$$\delta\mu_2 \;\equiv\; \mu_s - \mu_u - \mu_e = \delta\mu_s - \delta\mu_u - \delta\mu_e, \tag{3.5b}$$

where $\delta\mu_i$ denotes the deviation of the chemical potential μ_i from its equilibrium value. (Note that $\delta\mu_3 \equiv \mu_d - \mu_u - \mu_e = \delta\mu_2 - \delta\mu_1$ is not independent.) When $\delta\mu_i$ are non-

zero, the corresponding pairs of forward and backward weak processes in Fig. 1.4 have
different rates. To leading order, the rate differences are linear in $\delta \mu_i$,

$$\Gamma_{(a)} - \Gamma_{(b)} = -\lambda_1 \delta \mu_1, \tag{3.6a}$$

$$\Gamma_{(c)} - \Gamma_{(d)} = -\lambda_2 \delta \mu_2, \tag{3.6b}$$

$$\Gamma_{(e)} - \Gamma_{(f)} = -\lambda_3 \left(\delta \mu_2 - \delta \mu_1\right). \tag{3.6c}$$

The corresponding λ-rates have been calculated for the normal phase [71, 72, 103, 108]
as well as several color superconducting phases of quark matter [65, 101, 106]. The
results for the normal phase, in particular, read

$$\lambda_1^{(0)} \simeq \frac{64}{5\pi^3} G_F^2 \cos^2 \theta_C \sin^2 \theta_C \mu_d^5 T^2, \tag{3.7a}$$

$$\lambda_2^{(0)} \simeq \frac{17}{40\pi} G_F^2 \sin^2 \theta_C \mu_s m_s^2 T^4, \tag{3.7b}$$

$$\lambda_3^{(0)} \simeq \frac{17}{15\pi^2} G_F^2 \cos^2 \theta_C \alpha_s \mu_d \mu_u \mu_e T^4. \tag{3.7c}$$

These will be used below as a benchmark for the rates in spin-one color-superconducting
phases.

The semi-leptonic rate λ_3 is determined by the Urca processes $u + e^- \to d + \nu_e$
and $d \to u + e^- + \bar{\nu}_e$, shown in diagrams (e) and (f) in Fig. 1.4. It was calculated in
Ref. [65] for four different spin-one color-superconducting phases of quark matter. The
result has a form of the product of the rate in the normal phase $\lambda_3^{(0)}$ and a phase-specific
suppression factor,

$$\lambda_3 = \lambda_3^{(0)} \left[\frac{1}{3} + \frac{2}{3} H\left(\frac{\phi}{T}\right)\right], \tag{3.8}$$

where ϕ is the spin-one color-superconducting gap parameter, and $H(\phi/T)$ is a sup-
pression factor for the processes involving gapped quasiparticles. (The first term in
square brackets is the contribution of ungapped quasiparticles.) When $\phi \to 0$, the sup-
pression factor $H(\phi/T)$ approaches 1 and the normal phase result is restored. A simple
fit to the numerical data of Ref. [65] for $H(\phi/T)$ is presented in Appendix B.1.

Because of similar kinematics and phase space constraints for the other pair of semi-leptonic processes, $u + e^- \rightarrow s + v_e$ and $s \rightarrow u + e^- + \bar{v}_e$, shown in diagrams (c) and (d) in Fig. 1.4, the dependence of the rate λ_2 on the color-superconducting gap should take the same form as λ_3 in Eq. (3.8), i.e.,

$$\lambda_2 = \lambda_2^{(0)} \left[\frac{1}{3} + \frac{2}{3} H \left(\frac{\phi}{T} \right) \right]. \tag{3.9}$$

In contrast, the rate λ_1 is determined by the nonleptonic processes $u + d \rightarrow s + u$ and $s + u \rightarrow u + d$, see diagrams (a) and (b) in Fig. 1.4, which have a qualitatively different kinematics. In spin-one color-superconducting phases of quark matter, this was recently calculated in Ref. [106]. The numerical result can be conveniently summarized by the following expression:

$$\lambda_1 = \lambda_1^{(0)} \left[\mathcal{N} + (1 - \mathcal{N}) \tilde{H} \left(\frac{\phi}{T} \right) \right], \tag{3.10}$$

where, in addition to the suppression factor $\tilde{H}(\phi/T)$, we also introduced a constant $\mathcal{N}$, which determines a relative contribution of the ungapped quasiparticles to the corresponding rate. In the four spin-one phases studied in Ref. [106], the constant takes the following values: $\mathcal{N}^A = \mathcal{N}^{\text{polar}} = 1/9$, $\mathcal{N}^{\text{planar}} \approx 0.0393$, and $\mathcal{N}^{\text{CSL}} = 928/27027 \approx 0.0343$. A simple fit to the numerical data for $\tilde{H}(\phi/T)$ is given in Appendix B.2.

When the rates (3.8), (3.9) and (3.10) are known, the calculation of the instantaneous pressure and, thus, the bulk viscosity from Eq. (4.6) is straightforward [77]. Here we quote only the final expression for the viscosity,

$$\zeta = \zeta_1 + \zeta_2 + \zeta_3, \tag{3.11}$$

where

$$\zeta_1 = \frac{n}{\omega} \frac{\alpha_2 \alpha_3}{g_1^2 + g_2^2} \left[\alpha_1 \alpha_2 \alpha_3 C_1^2 + (\alpha_1 + \alpha_2 + \alpha_3) (A_1 C_2 - A_2 C_1)^2 \right], \tag{3.12a}$$

$$\zeta_2 = \frac{n}{\omega} \frac{\alpha_1 \alpha_3}{g_1^2 + g_2^2} \left[\alpha_1 \alpha_2 \alpha_3 C_2^2 + (\alpha_1 + \alpha_2 + \alpha_3) [(A_2 - B_2) C_1 - A_2 C_2]^2 \right], \tag{3.12b}$$

$$\zeta_3 = \frac{n}{\omega} \frac{\alpha_1 \alpha_2}{g_1^2 + g_2^2} \left[\alpha_1 \alpha_2 \alpha_3 (C_1 - C_2)^2 + (\alpha_1 + \alpha_2 + \alpha_3) (B_1 C_2 - B_2 C_1)^2 \right], \tag{3.12c}$$

and

$$g_1 = -\alpha_1 \alpha_2 \alpha_3 + (\alpha_1 + \alpha_2 + \alpha_3)(B_1 A_2 - A_1 B_2), \tag{3.13a}$$

$$g_2 = \alpha_1 \alpha_2 (B_1 - B_2) + \alpha_1 \alpha_3 (A_2 - B_2) + \alpha_2 \alpha_3 A_1. \tag{3.13b}$$

Here $\alpha_i \equiv n\omega/\lambda_i$ $(i = 1, 2)$ and n is the baryon density of quark matter. The quantities A_i, B_i and C_i are susceptibility-like functions, see Ref. [77] for the definition. To leading order in ϕ/μ_i, they are the same as in the normal phase.

For comparison, let us also note that the bulk viscosity in the limit of the vanishing semi-leptonic rates reads

$$\zeta_{\text{non}} = \frac{n}{\omega} \frac{\alpha_1 C_1^2}{\alpha_1^2 + A_1^2}. \tag{3.14}$$

3.2 Numerical results for bulk viscosity

In our calculation of the bulk viscosity in spin-one color-superconducting quark matter below, we choose the same two representative sets of model parameters as in Ref. [77]:

Set A	Set B
$n = 5\rho_0$	$n = 10\rho_0$
$m_s = 300$ MeV	$m_s = 140$ MeV
$\alpha_s = 0.2$	$\alpha_s = 0.1$

In both cases, the masses of light quarks are the same: $m_u = 5$ MeV and $m_d = 9$ MeV. In accordance with general expectations, the values of the strange quark mass m_s and the strong coupling constant α_s should be larger (smaller) in the case of lower (higher) density. This qualitative property is reflected in the model parameters in Set A (Set B). The values of all chemical potentials as well as the coefficient functions A_i, B_i and C_i for each set of parameters are quoted in Table 3.1.

It may be appropriate to briefly comment about the choice of the strong coupling constant α_s in the model at hand. The values of α_s in both sets of parameters may seem abnormally small. Indeed, the running coupling in QCD is about 0.12 at the scale of M_Z (mass of Z boson) and about 0.32 at $\sqrt{3}$ GeV [109]. However, here we use the model parameter α_s only in order to capture several qualitative (Fermi liquid) effects in quark matter. Its nonzero value allows (i) to avoid the underestimation of the rate of semi-leptonic processes due to a limited phase space [110] and (ii) to mimic the modification of the quark equation of state due to strong interactions, see Ref. [77] for details. The naive extension of the corresponding leading order corrections to the regime of strong coupling is problematic. Not only would this imply the use of the perturbative results beyond the range of their validity, but it would also lead to very large and seemingly unphysical effects on the equation of state, used to determine the susceptibility functions A_i, B_i and C_i. (Notably, if the equation of state is kept unchanged, the increase

Table 3.1: Two sets of parameters used in the calculation of the bulk viscosity.

model	μ_e [MeV]	μ_u [MeV]	$\mu_d = \mu_s$ [MeV]	A_1 [MeV]	A_2 [MeV]
Set A	39.139	402.463	441.602	239.432	127.937
Set B	7.396	495.275	502.671	324.556	164.288

model	B_1 [MeV]	B_2 [MeV]	C_1 [MeV]	C_2 [MeV]
Set A	111.386	-3.726×10^4	-60.463	-60.460
Set B	160.268	-2.080×10^6	-10.692	-10.709

of α_s in the $\lambda_3^{(0)}$-rate, even by an order of magnitude, has little effect on the viscosity.)
This dilemma could be resolved by properly accounting the non-perturbative dynamics of QCD. At present, however, such a task seems insurmountable at the low energy scales relevant for neutron stars. For the purposes of this study, therefore, we treat α_s as a small independent parameter that captures only some qualitative properties of quark matter.

Here the critical temperature of the spin-one color-superconducting phase transition is assumed to be $T_c = 2$ MeV. This may be a somewhat high, but still reasonable value for T_c. Indeed, in QCD the spin-one gap is estimated to be about two orders of magnitude smaller than the spin-zero gap [52, 112, 55], and the latter is naturally of order 100 MeV [26, 27, 28, 32, 33, 34]. Even higher values of the spin-one gap have been reported in Ref. [114]. The effect of varying the critical temperature is easy to understand and will be briefly discussed below. As in Ref. [65], we use the following model temperature dependence of the gap parameter:

$$\phi(T) = \phi_0 \sqrt{1 - \left(\frac{T}{T_c}\right)^2}, \quad \text{for} \quad T < T_c \tag{3.15}$$

with ϕ_0 being the value of the gap parameter at $T = 0$. Note that the ratio T_c/ϕ_0 depends on the choice of the phase [52]. The approximate values of this ratio are 0.8 (CSL), 0.66 (planar), 0.49 (polar), and 0.81 (A-phase).
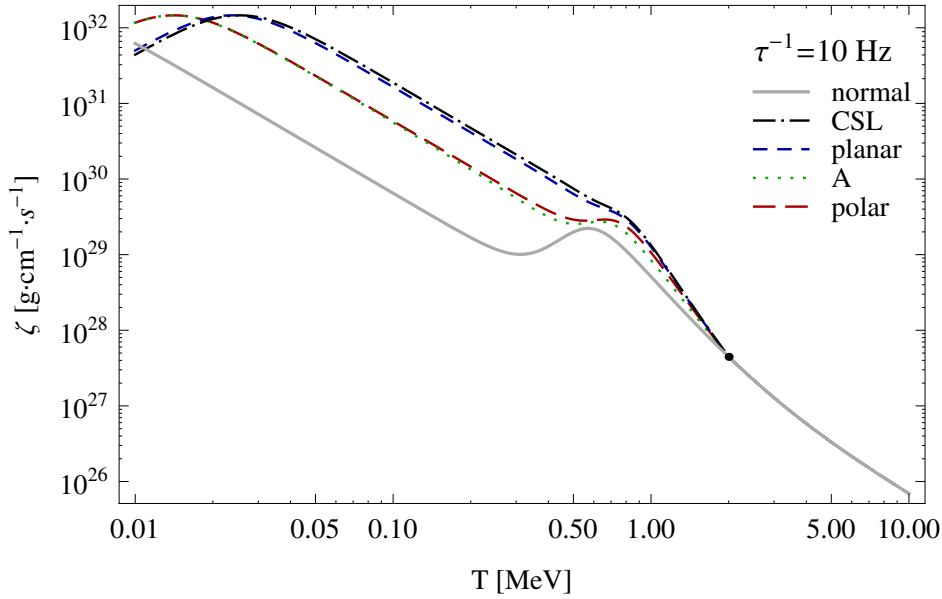
Figure 3.1: Temperature dependence of bulk viscosity ζ for the model parameters in Set A, the color-superconducting critical temperature $T_c = 2$ MeV, and the frequency of density oscillations $\tau^{-1} = 10$ Hz.

For model parameters in Set A, the numerical results are presented in Fig. 3.1-Fig. 3.4. As we can see, the value of T_c determines the point where the bulk viscosity starts to deviate from the benchmark result in the normal phase (shown by the gray solid line). Fig. 3.1 and Fig. 3.2 show the dependence of the bulk viscosity ζ on temperature for two representative values of the oscillation frequency, $\tau^{-1} = 10$ Hz and $\tau^{-1} = 1000$ Hz. Fig. 3.3 and Fig. 3.4 show the temperature dependence of the ratio ζ/ζ_{non}, where ζ is the bulk viscosity that takes into account all weak processes, while ζ_{non} is an approximate result, see Eq. (3.14), in which only the nonleptonic processes are included and the semi-leptonic processes are not. When the ratio ζ/ζ_{non} is substantially larger than 1, it is an indication that the semi-leptonic processes play an important role and, thus, cannot be neglected.

Compared to the normal phase result, the main features of the temperature dependences in spin-one color-superconducting phases (see Fig. 3.3) are (i) a smoothed

52
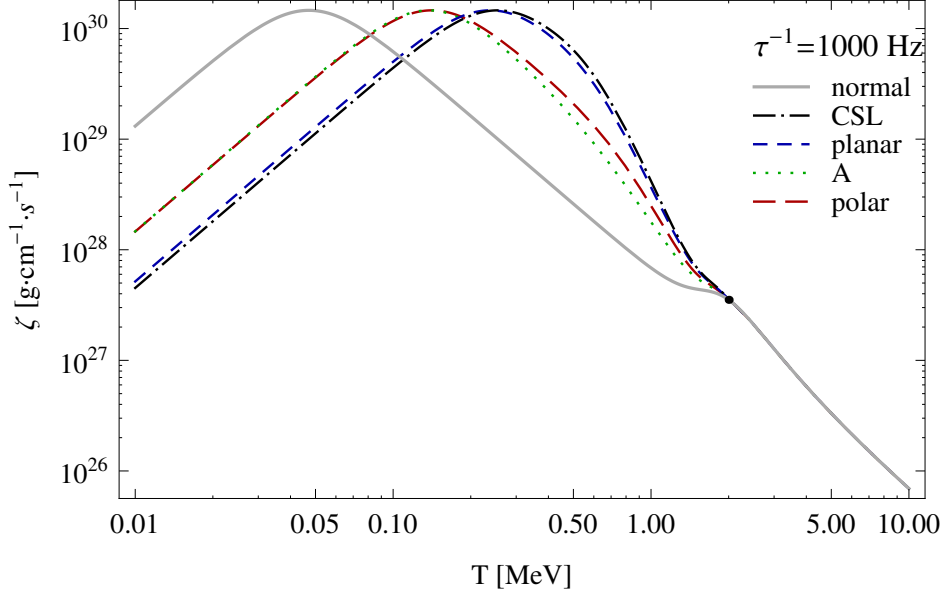
Figure 3.2: Temperature dependence of bulk viscosity ζ for the model parameters in Set A, the color-superconducting critical temperature $T_c = 2$ MeV, and the frequency of density oscillations $\tau^{-1} = 1000$ Hz.

shape of the semi-leptonic "hump" and (ii) an overall enhancement of the bulk viscosity due to color superconductivity for a substantial range of temperatures below T_c.

As in the case of the normal phase, the semi-leptonic processes are responsible for an increase ("hump") of the bulk viscosity in a region of temperatures around T_{hump}, where

$$T_{\text{hump}}^{(\text{Set A})} \simeq 2.1 \text{ MeV} \left(\frac{1 \text{ ms}}{\tau} \right)^{1/4}, \tag{3.16a}$$

$$T_{\text{hump}}^{(\text{Set B})} \simeq 1.4 \text{ MeV} \left(\frac{1 \text{ ms}}{\tau} \right)^{1/4} \tag{3.16b}$$

are the approximate positions of the peak of the hump in the normal phase in the case of the model parameters in Set A and Set B, respectively. In order to derive these results, we used an approximate expression for the bulk viscosity in Eq. (24) of Ref. [77], which is valid when the nonleptonic rate is infinitely large while the semi-leptonic rates are finite. The maximum of that expression corresponds to $\lambda_2 + \lambda_3 =$

53

Figure 3.3: Temperature dependence of the ratio $\zeta/\zeta_{\mathrm{non}}$ for the model parameters in Set A, the color-superconducting critical temperature $T_c = 2$ MeV, and the frequency of density oscillations $\tau^{-1} = 10$ Hz.

$n\omega A_1/(B_1 A_2 - B_2 A_1)$, whose solution determines an approximate value for T_{hump}. Two remarks are in order here: (i) the scaling law $T_{\mathrm{hump}} \propto 1/\tau^{1/4}$ follows from the power-law temperature dependence of the semi-leptonic rates $\lambda_2, \lambda_3 \propto T^4$ and (ii) the overall value in Eq. (3.16) is slightly corrected to match the actual numerical results in the case of a finite nonleptonic rate.

Figure 3.4: Temperature dependence of the ratio ζ/ζ_{non} for the model parameters in Set A, the color-superconducting critical temperature $T_c = 2$ MeV, and the frequency of density oscillations $\tau^{-1} = 1000$ Hz.

When $T_c \gtrsim T_{\text{hump}}$ the semi-leptonic hump is partially washed out by the presence of color superconductivity. This is most clearly seen from the ratio of the bulk viscosities ζ/ζ_{non} in Fig. 3.3 and Fig. 3.4. While the inclusion of the semi-leptonic processes leads to an increase of the viscosity, the effect is not as large as in the normal phase. Of course, this conclusion is sensitive to the choice of the color-superconducting critical temperature T_c. In general, two qualitatively different regimes can be realized. When $T_c \lesssim T_{\text{hump}}$, the hump occurs in the normal phase and, therefore, its shape is almost unaffected by color superconductivity. In the opposite case, $T_c \gtrsim T_{\text{hump}}$, the effect is present and gets stronger as T_c increases relative to T_{hump}.
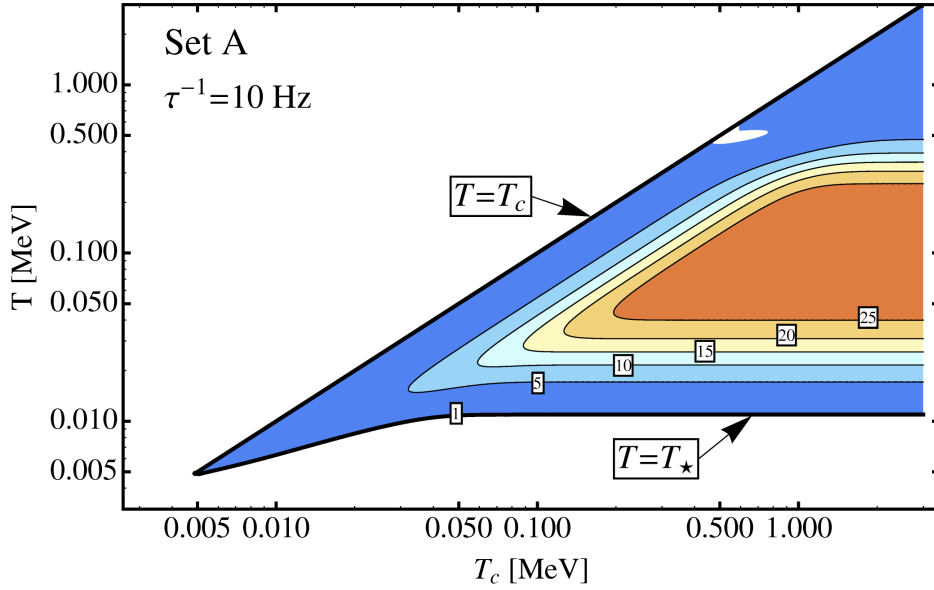
Figure 3.5: The contour plot of the bulk viscosity enhancement factor due to spin-one color superconductivity. The results are for the CSL phase in a model with the parameters in Set A. The frequency of the density oscillations is $\tau^{-1} = 10$ Hz.

Now, let us turn to an overall enhancement of the bulk viscosity due to color superconductivity below T_c. This is observed almost for the whole range of temperatures $T_{0,\text{max}} \lesssim T \leq T_c$, where $T_{0,\text{max}}$ is the temperature at which the bulk viscosity of the normal phase has a global maximum. The value of $T_{0,\text{max}}$ can be easily estimated by considering an approximate expression for the bulk viscosity (3.14) when only the nonleptonic processes are taken into account. The maximum of Eq. (3.14) corresponds to $\alpha_1 = A_1$. After solving this for the temperature, we obtain

$$T_{0,\text{max}}^{(\text{Set A})} \simeq 47 \text{ keV} \sqrt{\frac{1 \text{ ms}}{\tau}}, \tag{3.17a}$$

$$T_{0,\text{max}}^{(\text{Set B})} \simeq 41 \text{ keV} \sqrt{\frac{1 \text{ ms}}{\tau}}, \tag{3.17b}$$

where τ is the period of oscillations measured in milliseconds. Notably, the location of the maximum is almost the same for both sets of model parameters. Because of the superconductivity, the location of the maximum is shifted to a higher temperature, $T_{\phi,\text{max}} \simeq T_{0,\text{max}}/\sqrt{\mathcal{N}}$, where $\mathcal{N}$ is the same parameter that appears in Eq. (3.10). Tak-

56
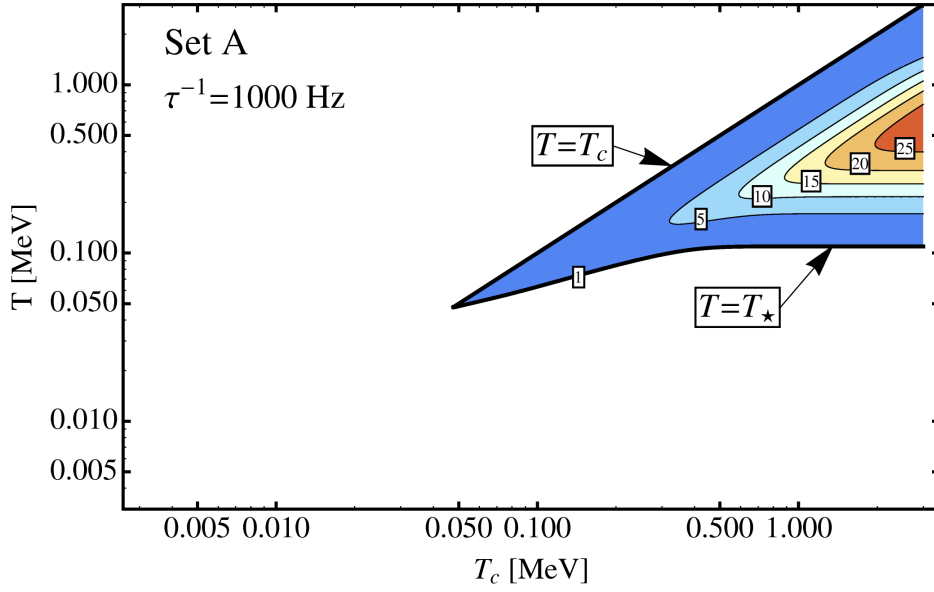
Figure 3.6: The contour plot of the bulk viscosity enhancement factor due to spin-one color superconductivity. The results are for the CSL phase in a model with the parameters in Set A. The frequency of the density oscillations is $\tau^{-1} = 1000$ Hz.

ing the shift of the maximum into account, we find that the enhancement relative to the normal phase is observed for $T_\star \leq T \leq T_c$ with $T_\star \simeq T_{0,\mathrm{max}}/\mathscr{N}^{1/4}$ being the point between $T_{0,\mathrm{max}}$ and $T_{\phi,\mathrm{max}}$, at which the bulk viscosities for the normal and superconducting phases cross. At lower temperatures, $T < T_\star$, the effect of color superconductivity is opposite: it reduces the bulk viscosity.
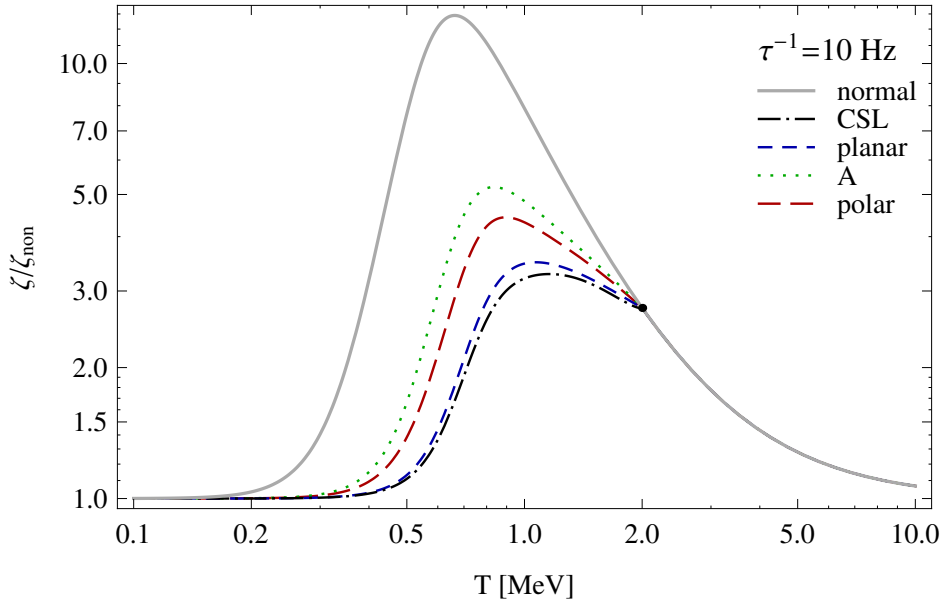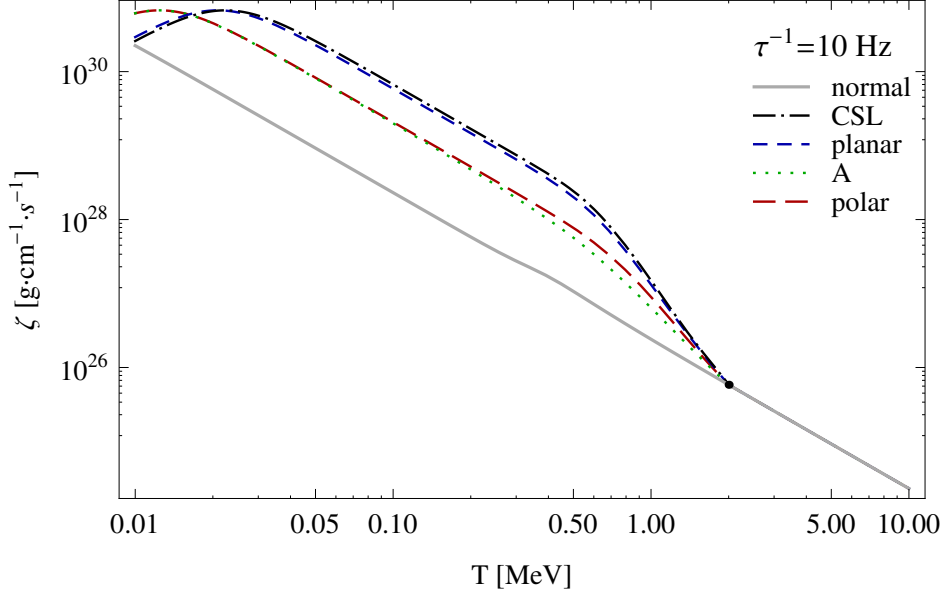
Figure 3.7: Temperature dependence of bulk viscosity ζ for the model parameters in Set B, the color-superconducting critical temperature $T_c = 2$ MeV, and the frequency of density oscillations $\tau^{-1} = 10$ Hz.

The range of temperatures, in which the bulk viscosity increases relative to the normal phase of quark matter, depends on the value of the critical temperature T_c and the frequency of oscillations. While the actual enhancement of the viscosity also depends on the specific pattern of spin-one pairing, the qualitative features in all four phases studied here are similar. As an example, let us consider the CSL phase in more detail. In Fig. 3.5 and Fig. 3.6, we show the contour plot for the bulk viscosity enhancement factor due to color superconductivity. The ratio $\zeta_{CSL}/\zeta_{normal}$ is larger than 1 only in the shaded regions in Fig. 3.5 and Fig. 3.6. In white regions, it is either 1 (when $T > T_c$) or less than 1 (otherwise).

As evident from Fig. 3.5 and Fig. 3.6, the enhancement of the bulk viscosity by spin-one color superconductivity occurs in a rather wide range of temperatures, especially when the frequency of density oscillations is not too large and the value of T_c is not too small. At $\tau^{-1} = 10$ Hz, for example, it extends over an order of magnitude
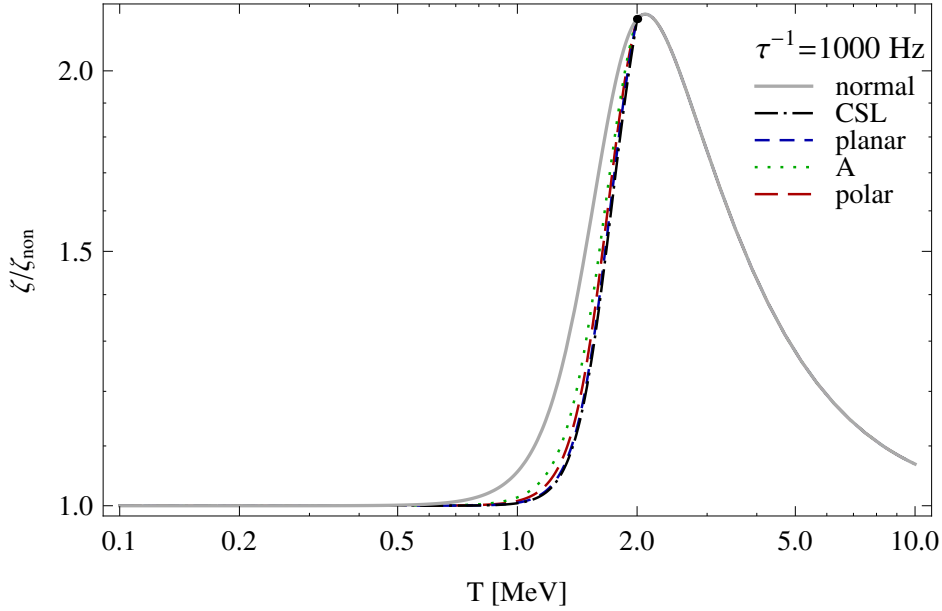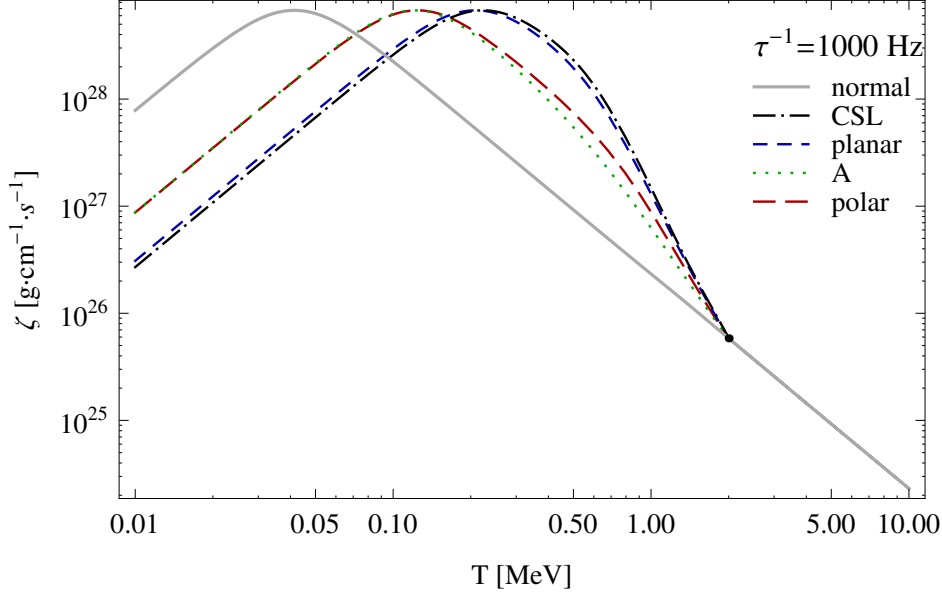
Figure 3.8: Temperature dependence of bulk viscosity ζ for the model parameters in Set B, the color-superconducting critical temperature $T_c = 2$ MeV, and the frequency of density oscillations $\tau^{-1} = 1000$ Hz.

or more in temperature, provided $T_c \gtrsim 100$ keV. At $\tau^{-1} = 1000$ Hz, in contrast, an order of magnitude or wider temperature range for the enhancement is seen only if $T_c \gtrsim 1$ MeV. (It should be noted that, in the case $\tau^{-1} = 10$ Hz shown in Fig. 3.5, the ratio $\zeta_{\text{CSL}}/\zeta_{\text{normal}}$ is truly less than 1 in a small white region just below the $T = T_c$ line. This "abnormality" is due to a subtle interplay between the semi-leptonic and nonleptonic processes when the value of T_c is fine-tuned to be near T_{hump}.)

By ignoring the subtle complications due to the semi-leptonic hump around T_{hump}, we find that the enhancement of the bulk viscosity in the window of temperatures $T_\star \leq T \leq T_c$ (as well as the suppression at lower temperatures, $T < T_\star$) is primarily due to the reduction of the nonleptonic rate λ_1 in color-superconducting phases. At temperatures below T_c, when all gapped quasiparticles effectively cease to contribute, the corresponding reduction factor for the rate is approximately given by the value of $\mathcal{N}$. This means that the enhancement factor for the viscosity approaches its inverse value,
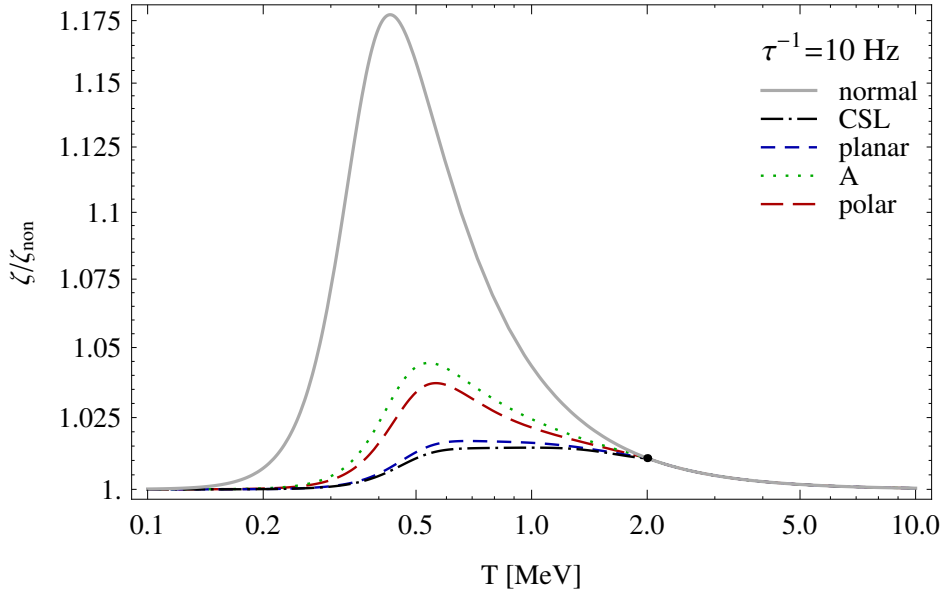
Figure 3.9: Temperature dependence of the ratio ζ/ζ_{non} for the model parameters in Set B, the color-superconducting critical temperature $T_c = 2$ MeV, and the frequency of density oscillations $\tau^{-1} = 10$ Hz.

$\mathcal{N}^{-1}$. By making use of the numerical results for $\mathcal{N}$, we find that the enhancement factor for the bulk viscosity reaches up to about 9 in the A- and polar phases, 25 in the planar phase and 29 in the CSL phase. (The suppression factors at $T < T_\star$ approach the same values.) In the region of the hump, of course, the behavior is more complicated, but the overall effect of superconductivity is still mainly to increase the bulk viscosity.

The numerical results in the case of the model parameters in Set B are shown in Fig. 3.7, Fig. 3.8, Fig. 3.9 and Fig. 3.10. The qualitative features are similar to those obtained for Set A. However, the effect of the semi-leptonic processes is less pronounced: the corresponding hump is almost non-existent and the ratio ζ/ζ_{non} does not much deviate from 1. At the same time, the effect of color superconductivity is very well pronounced. Compared to the normal phase result, an enhancement of the bulk viscosity by a factor of about $\mathcal{N}^{-1}$ is seen in a relatively wide window of temperatures from $T_\star$ to T_c.
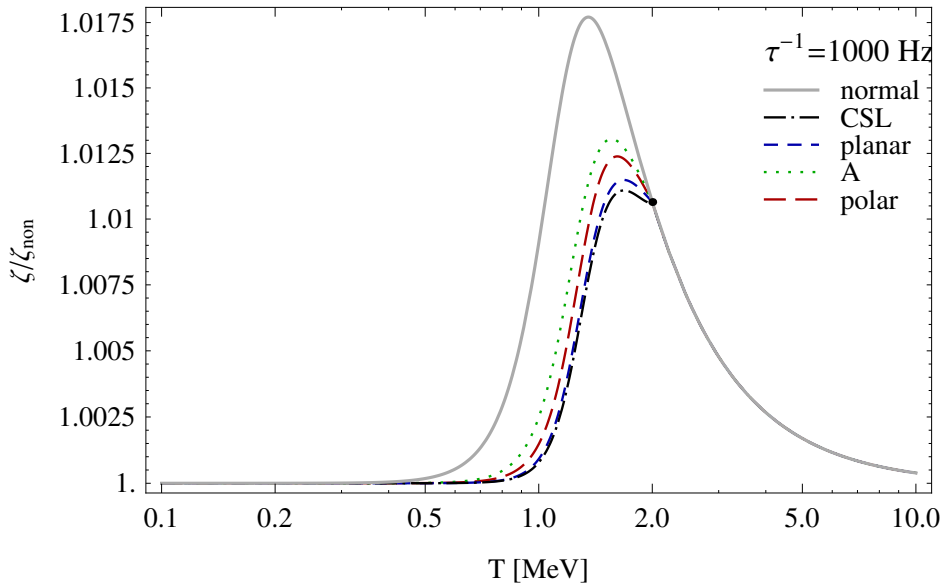
Figure 3.10: Temperature dependence of the ratio $\zeta/\zeta_{\mathrm{non}}$ for the model parameters in Set B, the color-superconducting critical temperature $T_c = 2$ MeV, and the frequency of density oscillations $\tau^{-1} = 1000$ Hz.

3.3   Disscusion

In this chapter, we calculated the bulk viscosity in spin-one color-superconducting strange quark matter by carefully taking into account the interplay between the non-leptonic and semi-leptonic week processes [111].

As expected, the nonleptonic processes give the dominant contribution to the viscosity in a wide range of parameters. Yet, as in the normal phase [77], the semi-leptonic processes may also lead to a substantial correction in a window of temperatures around T_{hump}, see Eq. (3.16). The value of T_{hump} scales as $1/\tau^{1/4}$ and happens to be of order 1 MeV for millisecond pulsars. The size and the relative importance of the hump can be conveniently measured by the ratio $\zeta/\zeta_{\mathrm{non}}$ when it is noticeably larger than 1. For millisecond pulsars, however, this ratio remains close to 1. The effect is more pronounced when the period is a few orders of magnitude longer. We also find that

the corresponding hump in the temperature dependence of the bulk viscosity of color superconductors is partially washed out compared to the normal phase. The higher is T_c relative to T_{hump}, the larger wash out of the hump is seen.

In this study we assumed that the critical temperature of the spin-one color-superconducting phase transition T_c is considerably larger than $T_{0,\text{max}}$, see Eq. (3.17). Then, the main effect of color superconductivity is an overall increase of the bulk viscosity in a wide range of temperatures, $T_{0,\text{max}}/\mathcal{N}^{1/4} \leq T \leq T_c$. (At lower temperatures, $T < T_{0,\text{max}}/\mathcal{N}^{1/4}$, color superconductivity leads to a suppression of the bulk viscosity.) This is primarily due to the suppression effect that color superconductivity has on the nonleptonic rate. At sufficiently low temperatures far from T_c, the rate is dominated by the ungapped quasiparticles, whose relative contribution is scaled by the factor $\mathcal{N}$ with respect to the normal phase (note that $\mathcal{N} < 1$). Therefore, the actual enhancement of the bulk viscosity is determined by the inverse value $\mathcal{N}^{-1}$. It is equal to 9 in the A- and polar phases, about 25 in the planar phase and about 29 in the CSL phase.

In relation to this result, it might be appropriate to note that a similar enhancement mechanism was previously observed for spin-zero color superconductors at $T \gtrsim T_{0,\text{max}}$ [101]. A special feature of spin-one color superconductivity is that the maximum enhancement factor can be much larger.

In our analysis, we utilized the same spin-one pairing pattern as in Refs. [52, 55, 112, 113]. In the case of zero quark masses, the main signature of the corresponding phases is the presence of ungapped quasiparticles. When quarks have small masses, the gaps of the corresponding modes are of order $\phi m/\mu$. These may be still too small to significantly affect our main results. However, if the spin-one gaps are larger, as some studies suggest [114], the suppression of the nonleptonic rates and, therefore, the enhancement of the bulk viscosity in color superconducting matter may turn out to be even stronger.

In application to compact stars, we may speculate that the transition to a spin-one color superconducting phase in a stellar core can have a stabilizing effect against the r-modes driven by the gravitational radiation [115]. If the critical temperature of the corresponding phase transition is on the order of or above 1 MeV, the corresponding dynamics can affect even relatively young stars.

CHAPTER 4

BULK VISCOSITY IN THE NONLINEAR AND ANHARMONIC REGIME OF

STRANGE QUARK MATTER

In the previous chapter, we only considered the bulk viscosity for the harmonic density

oscillations and linear terms of the rates. As discussed in Refs. [116, 117, 118, 119, 120,

121], the nonlinear regime in compact stars may be responsible for several qualitatively

new features in the dynamics. In this chapter we will discuss the bulk viscosity in the

nonlinear and anharmonic regime of normal strange quark matter.

4.1 Formalism

One can calculate the bulk viscosity ζ under conditions realized in stars by comparing

the hydrodynamic relation for the energy dissipation, averaged over one period τ,

$$\langle \dot{\mathscr{E}}_{\text{diss}} \rangle = -\frac{\zeta}{\tau} \int_0^\tau (\nabla \cdot \vec{v})^2 \, dt \simeq -\frac{\zeta}{n_0^2 \tau} \int_0^\tau (\delta \dot{n})^2 \, dt. \tag{4.1}$$

with the thermodynamic relation for the mechanical work, counteracting the hydrody-

namic flow,

$$\langle \dot{\mathscr{E}}_{\text{diss}} \rangle = \frac{n}{\tau} \int_0^\tau P \dot{V} \, dt \simeq -\frac{1}{n_0 \tau} \int_0^\tau P \delta \dot{n} \, dt. \tag{4.2}$$

The latter is given in terms of the instantaneous pressure P and the specific volume

$V \equiv 1/n$. In the above expressions, n_0 is the equilibrium density and $\delta n = n - n_0$ is

the density deviation from the equilibrium value. (Even when the magnitude of density

oscillations is not vanishingly small, we will assume that $|\delta n| \ll n_0$.)

If the magnitude of the density oscillations δn_0 is vanishingly small, one may

simulate the collective motion as a harmonic oscillation, $\delta n(t) = \delta n_0 \cos(\omega t)$. How-

ever, in a resonance regime, when large density oscillations develop, nonlinear effects

may start to play an important role. In this thesis, we study this possibility by simulat-

ing two different types of anharmonic density oscillations. The two types correspond

to oscillators with cubic and quartic terms in the potential energy, which have different

symmetry properties under $\delta n \to -\delta n$. The corresponding equations of motion read:

$$\delta \ddot{n} + \omega_0^2 \delta n (1 + \alpha \delta n) = 0, \qquad \text{(Type I)}, \qquad (4.3)$$

$$\delta \ddot{n} + \omega_0^2 \delta n \left(1 + \beta \delta n^2\right) = 0, \qquad \text{(Type II)}. \qquad (4.4)$$

Note that the coupling constants α and β have the dimensions of an inverse density and an inverse density squared, respectively. It is convenient, therefore, to introduce the dimensionless parameters $\alpha^* \equiv \alpha \delta n_0$ and $\beta^* \equiv \beta (\delta n_0)^2$, which are given in terms of the amplitude of density oscillations δn_0. [For asymmetric oscillations, described by Eq. (4.3), we assume that the amplitude is the maximum deviation from the equilibrium point.] Note that the parameters α^* and β^* can be either positive or negative. General periodic solutions for both types of anharmonic oscillators can be given in terms of the Jacobi elliptic functions. The corresponding solutions are presented in Appendix C. By substituting these exact solutions into Eq. (4.1) and making use of the result in Eq. (C.4), we derive

$$\langle \dot{\mathcal{E}}_{\text{diss}} \rangle = -\frac{\zeta \omega_0^2}{2} \left(\frac{\delta n_0}{n_0}\right)^2 \mathcal{F}, \qquad (4.5)$$

where the constant $\mathcal{F}$ for each type of solution is determined in terms of α^* and β^*, see Eqs. (C.5) and (C.9), respectively. As is easy to check, $\mathcal{F} \to 1$ in the harmonic limit $\alpha^* \to 0$ (Type I) or $\beta^* \to 0$ (Type II).

By comparing Eqs. (4.2) and (4.5), we obtain the following expression for the bulk viscosity:

$$\zeta = \frac{2n_0}{\omega_0^2 (\delta n_0)^2 \mathcal{F}} \frac{1}{\tau} \int_0^\tau P \delta \dot{n} \, dt. \qquad (4.6)$$

When there is a departure from β equilibrium, the pressure can be given in terms of the instantaneous composition,

$$P = \bar{P} + \frac{\partial P}{\partial n} \delta n + n(C_1 - C_2) \delta X_e + n C_1 \delta X_s, \qquad (4.7)$$

where $X_e \equiv n_e/n$ and $X_s \equiv n_s/n$ is the electron and strangeness fractions, and $\bar{P}$ is the pressure in equilibrium. The susceptibility functions C_1 and C_2 were defined in

65

Ref. [77]. By taking into account that δn is a periodic function, one finds that only the last two terms in the pressure (4.7) contribute to the bulk viscosity (4.6),

$$\zeta = \frac{2n_0^2}{\omega_0^2(\delta n_0)^2 \mathscr{F}} \frac{1}{\tau} \int_0^\tau [(C_1 - C_2)\delta X_e + C_1 \delta X_s] \delta \dot{n} \, dt. \tag{4.8}$$

The instantaneous composition of quark matter is determined by the weak processes, shown in Fig. 1.4. Taking all of them into account, we derive the following set of nonlinear differential equations for the electron and strangeness fractions:

$$n\frac{d(\delta X_e)}{dt} = (\Gamma_d - \Gamma_c) + (\Gamma_f - \Gamma_e) = \lambda_2 \delta \mu_2 \sum_{j=0}^{2} \chi_j \left(\frac{\delta \mu_2}{T}\right)^{2j}$$

$$+ \lambda_3 (\delta \mu_2 - \delta \mu_1) \sum_{j=0}^{2} \chi_j \left(\frac{\delta \mu_2 - \delta \mu_1}{T}\right)^{2j}, \tag{4.9}$$

$$n\frac{d(\delta X_s)}{dt} = (\Gamma_a - \Gamma_b) + (\Gamma_c - \Gamma_d)$$

$$= -\lambda_1 \delta \mu_1 \sum_{j=0}^{1} \Upsilon_j \left(\frac{\delta \mu_1}{T}\right)^{2j} - \lambda_2 \delta \mu_2 \sum_{j=0}^{2} \chi_j \left(\frac{\delta \mu_2}{T}\right)^{2j} \tag{4.10}$$

where $\delta \mu_1 \equiv \mu_s - \mu_d$, $\delta \mu_2 \equiv \mu_s - \mu_u - \mu_e$, and the notation for the λ-rates are the same as in Refs. [77, 111],

$$\lambda_1 = \frac{64}{5\pi^3} G_F^2 \sin^2 \theta_c \cos^2 \theta_c \mu_d^5 T^2, \tag{4.11}$$

$$\lambda_2 = \frac{17}{40\pi} G_F^2 \sin^2 \theta_c \mu_s m_s^2 T^4, \tag{4.12}$$

$$\lambda_3 = \frac{17}{15\pi^2} G_F^2 \cos^2 \theta_c \alpha_s \mu_d \mu_e \mu_u T^4. \tag{4.13}$$

In Eqs. (4.9) and (4.10), all higher order corrections in powers of $\delta \mu_i/T$ were taken into account, while higher order corrections in powers of $\delta \mu_i/\mu$ were neglected. This is the same approximation that was used in Ref. [122]. By calculating the semileptonic rates using the approach of Ref. [65], it is easy to check that the coefficients of the nonlinear terms are the same as in the nucleon direct Urca process [123, 124]: $\chi_0 = 1$, $\chi_1 = \frac{10}{17\pi^2}$, and $\chi_2 = \frac{1}{17\pi^4}$. The corresponding coefficients in the nonleptonic rates are $\Upsilon_0 = 1$ and $\Upsilon_1 = \frac{1}{4\pi^2}$ [103, 122, 125].

The functions that describe the deviation from equilibrium, $\delta\mu_i$, can be equivalently rewritten in terms of the electron and strangeness fractions: $\delta\mu_i = C_i\frac{\delta n}{n} + B_i\delta X_e + A_i\delta X_s$, where coefficient functions A_i, B_i and C_i were defined in Ref. [77]. By making use of these relations and Eqs. (4.9) and (4.10), we derive the following self-consistent set of equations for the dimensionless quantities $v_i \equiv \delta\mu_i/T$ (for $i = 1,2$),

$$
\begin{aligned}
n_0\frac{dv_i}{dt} &= \frac{C_i}{T}\delta\dot{n} - \lambda_1 A_i \sum_{j=0}^{1}\Upsilon_j(v_1)^{2j+1} - \lambda_2(A_i - B_i)\sum_{j=0}^{2}\chi_j(v_2)^{2j+1} \\
&\quad + \lambda_3 B_i\sum_{j=0}^{2}\chi_j(v_2 - v_1)^{2j+1}.
\end{aligned}
\tag{4.14}
$$

In this study, δn is a periodic function that describes anharmonic oscillations of either Type I or Type II, see Eqs. (4.3) and (4.4). We make use of the analytical results in Appendix C and solve Eq. (4.14) numerically. When the solutions for v_i (with $i = 1,2$) are available, one can invert the relations for $\delta\mu_i$ in terms of δn, δX_e and δX_s in order to determine the deviation of the electron and strangeness fractions,

$$
\delta X_e = G_e\frac{\delta n}{n_0} + H_e v_1 + J_e v_2,
\tag{4.15}
$$

$$
\delta X_s = G_s\frac{\delta n}{n_0} + H_s v_1 + J_s v_2.
\tag{4.16}
$$

where

$$
G_e = \frac{A_1 C_2 - A_2 C_1}{A_2 B_1 - A_1 B_2}, \qquad\qquad G_s = \frac{B_2 C_1 - B_1 C_2}{A_2 B_1 - A_1 B_2},
\tag{4.17}
$$

$$
H_e = \frac{TA_2}{A_2 B_1 - A_1 B_2}, \qquad\qquad H_s = -\frac{TB_2}{A_2 B_1 - A_1 B_2},
\tag{4.18}
$$

$$
J_e = -\frac{TA_1}{A_2 B_1 - A_1 B_2}, \qquad\qquad J_s = \frac{TB_1}{A_2 B_1 - A_1 B_2}.
\tag{4.19}
$$

Finally, by making use of these results in Eq. (4.8), we can calculate the bulk viscosity,

$$
\begin{aligned}
\zeta &= \frac{2Tn_0^2}{\omega_0^2(\delta n_0)^2\mathscr{F}}\frac{A_2(C_1 - C_2) - B_2 C_1}{A_2 B_1 - A_1 B_2}\frac{1}{\tau}\int_0^{\tau} v_1\,\delta\dot{n}\,dt \\
&\quad + \frac{2Tn_0^2}{\omega_0^2(\delta n_0)^2\mathscr{F}}\frac{B_1 C_1 - A_1(C_1 - C_2)}{A_2 B_1 - A_1 B_2}\frac{1}{\tau}\int_0^{\tau} v_2\,\delta\dot{n}\,dt.
\end{aligned}
\tag{4.20}
$$

4.2 Harmonic oscillations

In the limiting case of harmonic oscillations, the density deviations are described by $\delta n = \delta n_0 \sin(\omega_0 t)$ and the constant $\mathscr{F}$ in Eq. (4.5) is equal to 1. The numerical results for the bulk viscosity as a function of $\delta n_0/n_0$ for several fixed values of temperature are shown in Fig. 4.1. The linear regime corresponds to small values of $\delta n_0/n_0$, where the bulk viscosity saturates. It is also interesting to present the temperature dependence of the bulk viscosity. The corresponding plots for several fixed values of $\delta n_0/n_0$ are shown in Fig. 4.2. As we see, with decreasing the temperature, the bulk viscosity eventually levels off. This is the outcome of reaching the nonlinear regime, and it would be absent if the linear approximation were used instead. In both Fig. 4.1 and Fig. 4.2, the results for two representative values of the period of oscillations, $\tau = 0.1$ s and $\tau = 10^{-3}$ s, are shown. (In all calculations, we used the model parameters from Ref. [77] at $n = 5\rho_0$, where $\rho_0 \simeq 0.15$ fm^{-3} is the nuclear saturation density.) In most regions of the parameter space, our results qualitatively agree with earlier findings in Refs. [71, 72, 76, 74, 122, 125, 126, 127]. The only notable difference occurs in Fig. 4.2 around the "semileptonic" hump ($T \sim 1$ MeV). This comes from the interplay of semileptonic weak processes with the more dominant nonleptonic ones [77, 111]. In most of the studies, this is neglected because of a smallness of the semileptonic rates.

Here it is appropriate to mention that, in application to stellar quark matter, the bulk viscosity may not be the only, or even the dominant mechanism responsible for damping of the r-mode instabilities. For example, at sufficiently low temperatures, the corresponding dissipative dynamics is known to be dominated by the shear viscosity [128, 129]. (For several representative studies of the shear viscosity in dense quark matter see, for example, Refs. [66, 130, 131].) In this connection, our low-temperature results in Figs. 4.1 and 4.2 should be used only for the purpose of determining where exactly the damping by the shear viscosity takes over.

In order to better understand the role of nonlinear terms in the weak rates, see Eqs. (4.9) and (4.10), as well as their effect on the bulk viscosity, it is instructive to study the linear approximation. In this case, the expression for the viscosity can be derived analytically. As we shall see, this will be also helpful to elucidate the role of induced oscillations of $\delta\mu_2 = \mu_s - \mu_u - \mu_e$ when the semileptonic processes are formally switched off.

4.2.1 Harmonic oscillations: linear approximation

In the linear regime, Eqs. (4.9) and (4.10) for dimensionless functions v_i simplify down to

$$\frac{dv_1}{d\vartheta} = d_1 \cos\vartheta - f_1 v_1 - f_2 v_2 + f_3(v_2 - v_1), \tag{4.21}$$

$$\frac{dv_2}{d\vartheta} = d_2 \cos\vartheta - h_1 v_1 - h_2 v_2 + h_3(v_2 - v_1), \tag{4.22}$$

where $\vartheta = 2\pi t/\tau$ is the dimensionless time variable, $d_i = C_i \delta n_0/(T n_0)$ is the magnitude of the "driving force", and the other coefficient functions are

$$f_1 = \lambda_1 \frac{A_1}{\omega_0 n_0}, \qquad\qquad h_1 = \lambda_1 \frac{A_2}{\omega_0 n_0}, \tag{4.23}$$

$$f_2 = \lambda_2 \frac{A_1 - B_1}{\omega_0 n_0}, \qquad\qquad h_2 = \lambda_2 \frac{A_2 - B_2}{\omega_0 n_0}, \tag{4.24}$$

$$f_3 = \lambda_3 \frac{B_1}{\omega_0 n_0}, \qquad\qquad h_3 = \lambda_3 \frac{B_2}{\omega_0 n_0}. \tag{4.25}$$

The general solution to this set of equations in the steady state regime is given by

$$v_1 = x_1 \cos\vartheta + y_1 \sin\vartheta, \tag{4.26}$$

$$v_2 = x_2 \cos\vartheta + y_2 \sin\vartheta, \tag{4.27}$$

where the coefficients satisfy the following set of algebraic equations:

$$(f_1 + f_3)x_1 + (f_2 - f_3)x_2 + y_1 = d_1, \tag{4.28}$$

$$-x_1 + (f_1 + f_3)y_1 + (f_2 - f_3)y_2 = 0, \tag{4.29}$$

$$(h_1 + h_3)x_1 + (h_2 - h_3)x_2 + y_2 = d_2, \tag{4.30}$$

$$-x_2 + (h_1 + h_3)y_1 + (h_2 - h_3)y_2 = 0. \tag{4.31}$$

It is straightforward, although tedious to solve this set of equations. When the solution is available, the result for the bulk viscosity will follow from Eq. (4.20), i.e.

$$\zeta = \frac{Tn_0^2}{\omega\delta n_0}\frac{A_2(C_1-C_2)-B_2C_1}{A_2B_1-A_1B_2}x_1 + \frac{Tn_0^2}{\omega\delta n_0}\frac{B_1C_1-A_1(C_1-C_2)}{A_2B_1-A_1B_2}x_2. \quad (4.32)$$

It can be shown that this expression (with the appropriate solutions for x_1 and x_2) coincides exactly with the result for the bulk viscosity, obtained in Ref. [77].

4.2.2 Harmonic oscillations: nonleptonic contribution in linear approximation

If one ignores the semileptonic processes (i.e. if one formally takes $\lambda_2 = \lambda_3 = 0$), the linearized equations (4.21) and (4.22) for v_i's take the following form:

$$\frac{dv_1}{d\vartheta} = d_1\cos\vartheta - f_1 v_1, \quad (4.33)$$

$$\frac{dv_2}{d\vartheta} = d_2\cos\vartheta - h_1 v_1. \quad (4.34)$$

The explicit solution to this set of equations in the steady state regime is given by

$$v_1 = \frac{d_1}{1+f_1^2}(f_1\cos\vartheta + \sin\vartheta), \quad (4.35)$$

$$v_2 = d_2\sin\vartheta + \frac{d_1 h_1}{1+f_1^2}(\cos\vartheta - f_1\sin\vartheta), \quad (4.36)$$

and the corresponding expression for the bulk viscosity reads

$$\begin{aligned}\zeta_{\mathrm{non}} &= \frac{Tn_0^2}{\omega\delta n_0}\frac{A_2(C_1-C_2)-B_2C_1}{A_2B_1-A_1B_2}\frac{d_1 f_1}{1+f_1^2} \\ &+ \frac{Tn_0^2}{\omega\delta n_0}\frac{B_1C_1-A_1(C_1-C_2)}{A_2B_1-A_1B_2}\frac{d_1 h_1}{1+f_1^2} = \frac{\lambda_1 C_1^2}{\omega^2 + (\lambda_1 A_1/n_0)^2},\end{aligned} \quad (4.37)$$

where we used the relation $f_1/h_1 = A_1/A_2$ to arrive at the final result. As expected, this agrees with the known result [72, 77, 122, 125].

It is interesting to notice that the final result for the bulk viscosity receives a nonzero contribution due to the oscillation of $v_2 \equiv \delta\mu_2/T$. Since $\delta\mu_2 \equiv \mu_s - \mu_u - \mu_e$ controls the imbalance of the rates in the semileptonic processes, shown in Figs. 1.4 (c)

and (d), which are formally switched off in the approximation at hand, one might wonder why there should be such a contribution at all. The answer is quite simple. In absence of the semileptonic processes the electron fraction in quark matter cannot change. However, when the nonleptonic processes drive the oscillations of the strangeness composition, they inevitably induce the oscillations of $\delta\mu_2 \equiv \mu_s - \mu_u - \mu_e$. Then, the latter contributes to the instantaneous pressure and, in turn, to the bulk viscosity. Interestingly, such a contribution due to the induced oscillation of $\nu_2 \equiv \delta\mu_2/T$ were ignored in all previous studies [71, 72, 76, 74, 122, 125, 126, 127]. Fortunately, the corresponding correction is quantitatively small. The reason for its smallness seems to be rooted in the "accidental" fact that one of the susceptibility functions, B_2, is inversely proportional to the square of the chemical potential of electrons (rather than quarks) and, thus, is considerably larger than all others [77].

4.3 Bulk viscosity in anharmonic regime

In this section we study the effect that anharmonic oscillations of the density have on the bulk viscosity of dense quark matter.

4.3.1 Anharmonic oscillations of Type I

Let us start by modeling the density oscillations of quark matter $\delta n(t)$ by a time dependent anharmonic function of Type I, which is a solution to Eq. (4.3) with a fixed anharmonicity parameter α^*. Before we proceed to the numerical results, it is important to notice that the corresponding oscillations are asymmetric with respect to the equilibrium point $\delta n_{\text{eq}} = 0$. For $\alpha^* < 0$, the density oscillations are larger in the direction of positive δn, while for $\alpha^* > 0$, the oscillations are larger in the direction of negative δn, see also Fig. C.1. The cases of the positive and negative anharmonicity parameters are physically equivalent, however. Indeed, they are related by the following sign reversal symmetry: $\alpha \to -\alpha$ and $\delta n \to -\delta n$. Therefore, it is sufficient to study only one of them. For technical reasons, we choose $\alpha^* < 0$.

Typical results for the bulk viscosity as a function of anharmonicity parameter α^* are shown in the upper panel of Fig. 4.3 for the whole range of negative α^*, i.e. $-1 < \alpha^* < 0$, for which physically meaningful periodic solutions exist. We used the following values of the period and the amplitude of density oscillations: $\tau = 10^{-3}$ s and $\delta n_0/n_0 = 10^{-3}$, and plotted the results for several representative values of temperature. [It should be emphasized that the period τ is related to the "bare" frequency ω_0 by a modified relation, see Eq. (C.3).] In general, we find that the bulk viscosity decreases with increasing the degree of anharmonicity. This qualitative behavior may be understood as the result of an effective increase of the frequency of oscillations due to an admixture of higher harmonics. Quantitatively, however, the effect is rather small. Only a very large anharmonicity ($\alpha^* \approx -1$) leads to a substantial decrease of the bulk viscosity.

4.3.2 *Anharmonic oscillations of Type II*

Anharmonic density oscillations of Type II are modeled by a function $\delta n(t)$, which is a solution to Eq. (4.4) with a fixed anharmonicity parameter β^*. Conceptually, this is a simpler case because the oscillations are symmetric about the equilibrium point $\delta n_{\mathrm{eq}} = 0$. Unlike the case of Type I oscillations, there is no reversal symmetry here. As in the previous case, however, periodic solution exist only for a range of values of the the anharmonicity parameter, $\beta^* > -1$.

Numerical results for the bulk viscosity as a function of anharmonicity parameter β^* are shown in the lower panel of Fig. 4.3. The qualitative dependence of the viscosity on the parameter β^* is somewhat different. While it decreases at large values of parameter β^*, there is a range of small negative values of β^*, where it slightly grows with increasing anharmonicity. Moreover, this feature seems to be rather general and especially pronounced in the nonlinear regime (small temperature). Just like in the case of Type I oscillations, the effects appear to be rather small.

4.4 Disscusion

In this chapter we studied the bulk viscosity of dense quark matter by taking into account the nonlinear dependence of the nonleptonic and semileptonic weak rates on the parameter $\delta\mu_i/T$, where $\delta\mu_i$ are the chemical potentials that control the departure of strange quark matter from β equilibrium [132]. We reproduce the earlier observed interplay of the nonleptonic and semileptonic processes, leading to an increase ("hump") of the viscosity in a narrow temperature range around 1 MeV. The nonlinear corrections have a small effect on the corresponding shape of the "hump". The reason for this is a relatively high temperature ($T \sim 1$ MeV), at which the corresponding effects can be observed. At such moderately high temperatures, the interplay between the two types of weak processes is substantially affected only if the nonlinearity (measured by $\delta n_0/n_0$) is well above 10%.

We also found that the anharmonicity of density oscillations has an effect on the bulk viscosity, even though the effect was not large in the cases that we studied. For a strong anharmonicity, the bulk viscosity showed a substantial decrease. We also saw that different types of anharmonicity have slightly different qualitative as well as quantitative outcomes. This finding may suggest that some types of anharmonicity may be more efficient and, thus, lead to larger corrections to the bulk viscosity.
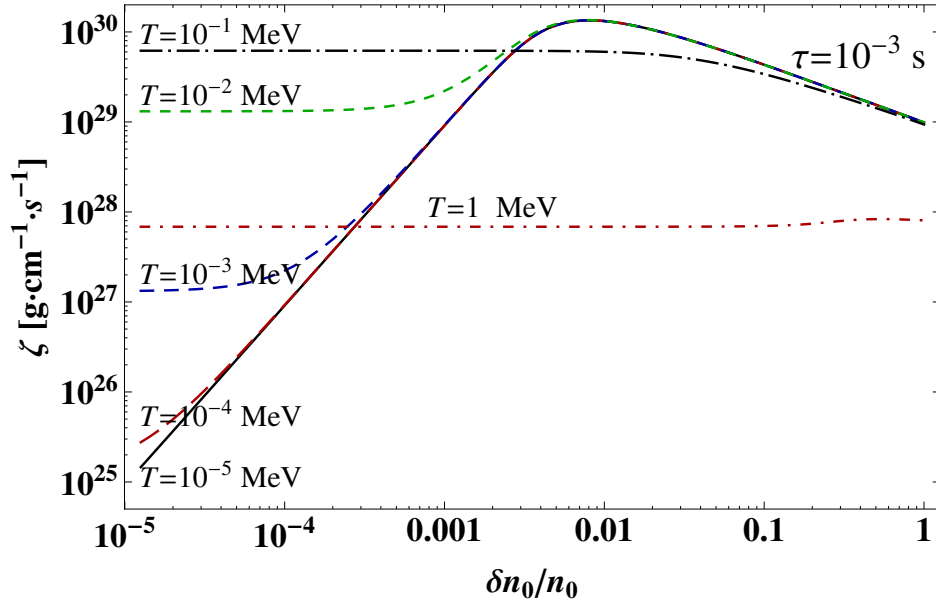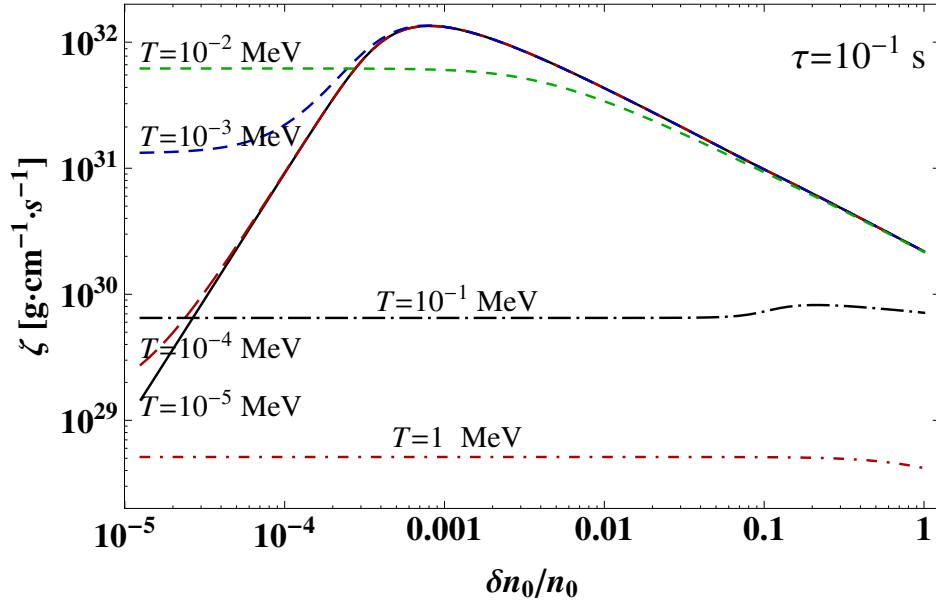
Figure 4.1: Bulk viscosity as a function of $\delta n_0/n_0$ for several fixed values of temperature, i.e. $T = 10^{-5}$ MeV (black solid line), $T = 10^{-4}$ MeV (red long-dashed line), $T = 10^{-3}$ MeV (blue dashed line), $T = 10^{-2}$ MeV (green short-dashed line), $T = 10^{-1}$ MeV (black dash-dotted line) and $T = 1$ MeV (red dash-dotted line line).
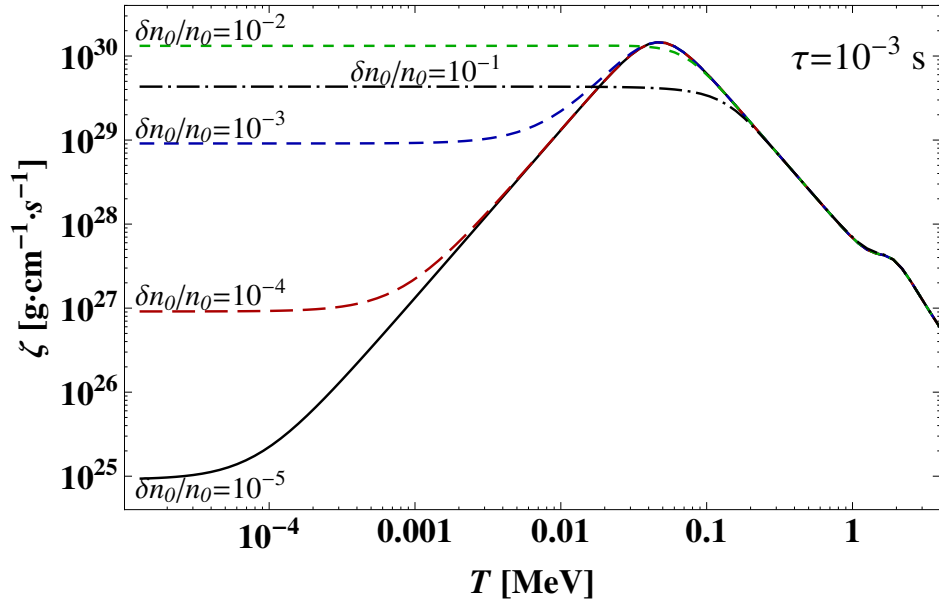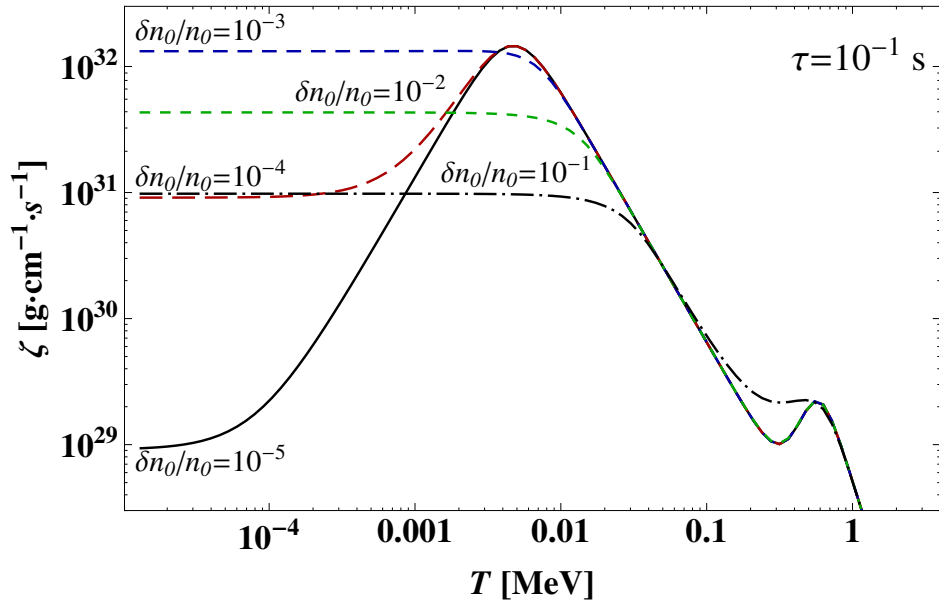
Figure 4.2: Bulk viscosity as a function of temperature for several fixed values of the amplitude of density oscillations, i.e. $\delta n_0/n_0 = 10^{-5}$ (black solid line), $\delta n_0/n_0 = 10^{-4}$ (red long-dashed line), $\delta n_0/n_0 = 10^{-3}$ (blue dashed line), $\delta n_0/n_0 = 10^{-2}$ (green short-dashed line), and $\delta n_0/n_0 = 10^{-1}$ (black dash-dotted line).
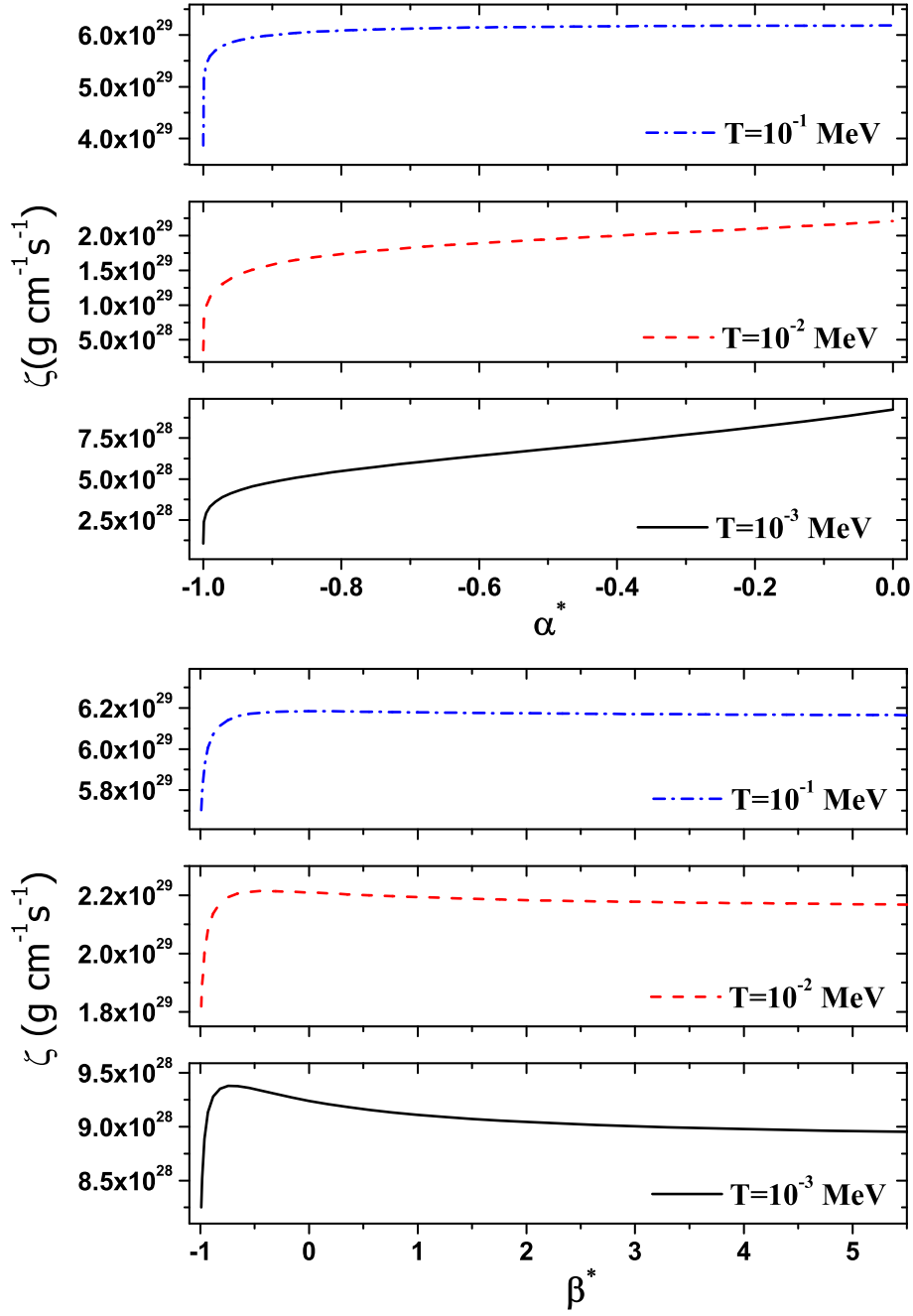
Figure 4.3: Bulk viscosity as a function of anharmonicity parameter of Type I (upper panel) and Type II (lower panel) for $\tau = 10^{-3}$ s, $\delta n_0/n_0 = 10^{-3}$ and several representative values of temperature.

CHAPTER 5

ANALYSIS OF FARADAY ROTATION AND MEGNETO-OPTICAL
TRANSMISSION IN MONOLAYER GRAPHENE

In this chapter, we calculate the Faraday rotation effect and magneto-optical transmission associated with the quantum Hall ferromagnetism and magnetic catalysis in monolayer graphene. The experimental setup is schematically shown in Fig. 5.1.

5.1   Formalism

The Faraday rotation angle θ and the magneto-optical transmission T are given by the following expressions [133]:

$$\theta(\Omega) = \frac{1}{2}\arg\left[\frac{t_+(\Omega)}{t_-(\Omega)}\right], \tag{5.1}$$

$$T(\Omega) = \frac{1}{2}\left[|t_+(\Omega)|^2 + |t_-(\Omega)|^2\right], \tag{5.2}$$
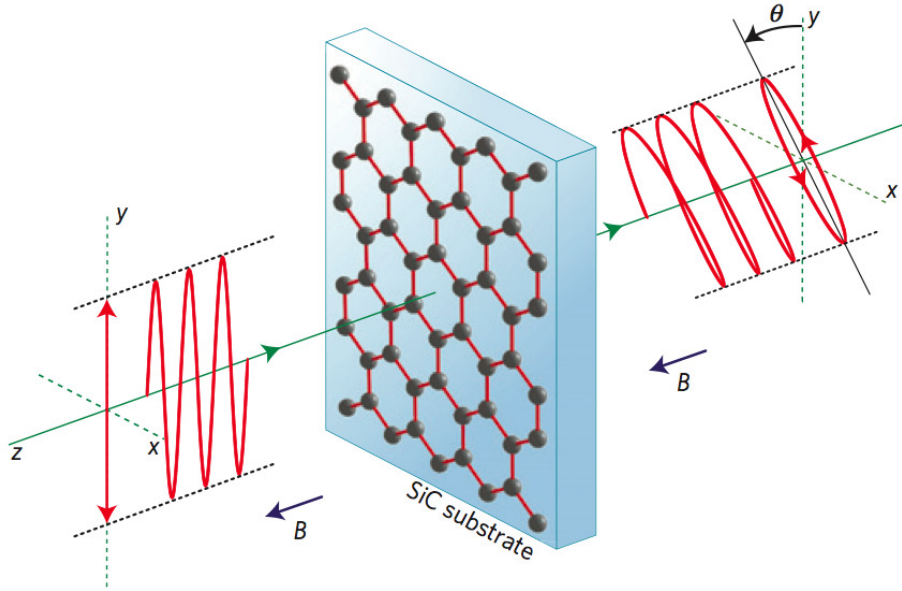
Figure 5.1: Schematic setup of the Faraday rotation experiment. The plane of polarization is rotated after passing through a monolayer of graphene with a perpendicular magnetic field. The figure is taken from Ref. [134].

which are written in terms of the transmission coefficients for circularly polarized light [135],

$$t_{\pm} = \frac{2n_0}{n_0 + n_s(\Omega) + (4\pi/c)\sigma_{\pm}(\Omega)}, \tag{5.3}$$

where n_0 and $n_s(\Omega)$ are the refractive indices of vacuum and substrate, respectively. The complex optical conductivities, $\sigma_{\pm}(\Omega)$, are defined in terms of the diagonal and off-diagonal elements of the conductivity tensor, i.e.,

$$\sigma_{\pm}(\Omega) = \sigma_{xx}(\Omega) \pm i\sigma_{xy}(\Omega). \tag{5.4}$$

By making use of the Kubo formalism, see (1.48), we rewrite the expression for the optical conductivity,

$$\sigma_{ij}(\Omega) = \frac{\operatorname{Im}\Pi_{ij}(\Omega + i0; 0)}{\Omega}, \tag{5.5}$$

in terms of the Fourier transform of the current-current correlation function,

$$\Pi_{ij}(\Omega; \mathbf{k}) = \int dt \int d^3\mathbf{r}\, e^{-i\Omega t + i\mathbf{k}\cdot\mathbf{r}} \Pi_{ij}(t; \mathbf{r}), \tag{5.6}$$

where the coordinate space function is given by

$$\Pi_{ij}(t; \mathbf{r}) = -ie^2 v_F^2 \operatorname{Tr}\left[\gamma^j \widetilde{G}(t; \mathbf{r}) \gamma^j \widetilde{G}(-t; -\mathbf{r})\right]. \tag{5.7}$$

Note that this expression is written in terms of function $\widetilde{G}(t; \mathbf{r})$, which is a translationally invariant part of the full quasiparticle Green's function, defined by

$$G(t - t'; \mathbf{r}, \mathbf{r}') = e^{i\Phi(\mathbf{r}, \mathbf{r}')}\widetilde{G}(t - t'; \mathbf{r} - \mathbf{r}'), \tag{5.8}$$

where $e^{i\Phi(\mathbf{r}, \mathbf{r}')}$ is the so-called Schwinger phase. The latter spoils translational invariance of the quasiparticle Green's function. Such a phase, however, does not affect the result for the current-current correlation function. For a detailed derivation of the quasiparticle Green's function and the explicit form of the Schwinger phase, see for example Appendix A in Ref. [136].

For our purposes below, it is convenient to use the ω-r representation of the Green's function[136] to arrive at the following form of the current-current correlation function:

$$\Pi_{ij}(i\Omega_r;0) = e^2 v_F^2 T \sum_{m=-\infty}^{\infty} \int d^2\mathbf{r}\, \text{tr}\left[\gamma^i \widetilde{G}(i\omega_m;\mathbf{r})\gamma^j \widetilde{G}(i\omega_m - i\Omega_r; -\mathbf{r})\right], \quad (5.9)$$

where we used the Matsubara formalism to introduce a nonzero temperature. By definition, the fermionic and bosonic Matsubara frequencies are $\omega_m = (2m+1)\pi T$ and $\Omega_r = 2r\pi T$, respectively. The explicit expression for the current-current correlation function $\Pi_{ij}(i\Omega_r;0)$ will be derived in Sec. 5.3. The corresponding function for real values of frequency will then be obtained by the analytical continuation $i\Omega_r \to \Omega + i0$. Before proceeding to the current-current correlation function, however, we first need to discuss the structure of the quasiparticle Green's function, used in the calculation.

5.2 Quasiparticle Green's function

Suppressing spin indices, we can write the inverse Green's function in the following general form [136]:

$$iG^{-1}(\omega;\mathbf{r},\mathbf{r}') = \left\{\gamma^0\omega + v_F \hat{F}^+ (\boldsymbol{\pi} \cdot \boldsymbol{\gamma}) + \hat{\Sigma}^+\right\}\delta(\mathbf{r} - \mathbf{r}'), \quad (5.10)$$

where $\hat{F}^+$ and $\hat{\Sigma}^+$ are generalized wave-function renormalization and self-energy operators, respectively. The (bare) Fermi velocity is $v_F = c/300$, where c is the speed of light in vacuum. By definition, the canonical momentum is $\boldsymbol{\pi} \equiv (\pi_x, \pi_y) = -i\hbar\nabla + e\mathbf{A}/c$. Here the vector potential $\mathbf{A}$ is chosen in the Landau gauge and corresponds to a magnetic field $\mathbf{B}$ orthogonal to the plane of graphene.

In the case of the bare Green's function, the corresponding wave-function renormalization and self-energy operators read $\hat{F}^+_{\text{bare}} = 1$ and $\hat{\Sigma}^+_{\text{bare}} = (\mu - \mu_B B\sigma^3)\gamma^0$. In general, $\hat{F}^+$ and $\hat{\Sigma}^+$ are functions of energy ω and the three mutually commuting dimensionless operators: $-(\boldsymbol{\pi}\cdot\boldsymbol{\gamma})^2\ell^2$, γ^0 and $is_\perp\gamma^1\gamma^2$, where $s_\perp = \text{sgn}(eB)$ and $\ell = \sqrt{\hbar c/|eB|}$ is the magnetic length.

Taking into account that $(\gamma^0)^2 = 1$ and $(is_\perp \gamma^1 \gamma^2)^2 = 1$, the operators $\hat{F}^+$ and $\hat{\Sigma}^+$ can be equivalently written in the following form:

$$\hat{F}^+ = f + \gamma^0 g + is_\perp \gamma^1 \gamma^2 \tilde{g} + is_\perp \gamma^0 \gamma^1 \gamma^2 \tilde{f}, \tag{5.11}$$

$$\hat{\Sigma}^+ = \tilde{\Delta} + \gamma^0 \mu + is_\perp \gamma^1 \gamma^2 \tilde{\mu} + is_\perp \gamma^0 \gamma^1 \gamma^2 \Delta, \tag{5.12}$$

where f, $\tilde{f}$, g, $\tilde{g}$, $\tilde{\Delta}$, Δ, μ, and $\tilde{\mu}$ are functions of only one operator, $(\pi \cdot \gamma)^2 \ell^2$. In addition to $\hat{F}^+$ and $\hat{\Sigma}^+$, it is convenient to introduce also functions $\hat{F}^-$ and $\hat{\Sigma}^-$,

$$\hat{F}^- = f - \gamma^0 g - is_\perp \gamma^1 \gamma^2 \tilde{g} + is_\perp \gamma^0 \gamma^1 \gamma^2 \tilde{f}, \tag{5.13}$$

$$\hat{\Sigma}^- = \tilde{\Delta} - \gamma^0 \mu - is_\perp \gamma^1 \gamma^2 \tilde{\mu} + is_\perp \gamma^0 \gamma^1 \gamma^2 \Delta, \tag{5.14}$$

which are related to $\hat{F}^+$ and $\hat{\Sigma}^+$ through the following commutation relations:

$$\hat{F}^+ (\pi \cdot \gamma) = (\pi \cdot \gamma) \hat{F}^-, \tag{5.15}$$

$$\hat{\Sigma}^+ (\pi \cdot \gamma) = (\pi \cdot \gamma) \hat{\Sigma}^-. \tag{5.16}$$

The physical meaning of functions f, $\tilde{f}$, g, $\tilde{g}$, $\tilde{\Delta}$, Δ, μ, and $\tilde{\mu}$ can be understood in part from the corresponding Dirac structures that they come with. For example, functions $\tilde{\Delta}$ and Δ are the Dirac (time-reversal even) and Haldane (time-reversal odd) mass functions, respectively. Functions μ and $\tilde{\mu}$ play the roles of chemical potentials controlling the charge density and the charge density imbalance between the two valleys in the Brillouin zone. The other functions (f, $\tilde{f}$, g, and $\tilde{g}$), appearing in the definition of $\hat{F}^\pm$, are several possible types of the wave function renormalization.

In general, all dynamical parameters (f, $\tilde{f}$, g, $\tilde{g}$, $\tilde{\Delta}$, Δ, μ, and $\tilde{\mu}$) are functions of the operator $-(\pi \cdot \gamma)^2 \ell^2$. The eigenvalues of $-(\pi \cdot \gamma)^2 \ell^2$ are nonnegative even integers: $2n \equiv -(2N + 1 + s_\perp s_{12})$, where $N = 0, 1, 2, \ldots$ is the orbital quantum number and $s_{12} = \pm 1$ is the sign of the pseudospin projection. Taking this into account, we can

80

write the eigenvalues of $\hat{F}^{\pm}$ and $\hat{\Sigma}^{\pm}$ as follows:

$$F_n^{s_0,s_{12}} \equiv f_n + s_0 g_n + s_{12}\tilde{g}_n + s_0 s_{12}\tilde{f}_n, \tag{5.17}$$

$$\Sigma_n^{s_0,s_{12}} \equiv \tilde{\Delta}_n + s_0 \mu_n + s_{12}\tilde{\mu}_n + s_0 s_{12}\Delta_n, \tag{5.18}$$

where f_n, $\tilde{f}_n$, g_n, $\tilde{g}_n$, $\tilde{\Delta}_n$, Δ_n, μ_n, and $\tilde{\mu}_n$ are the eigenvalues of the corresponding coefficient operators in the nth Landau level state.

The parameters $s_0 = \pm 1$ and $s_{12} = \pm 1$ are the eigenvalues of γ^0 and $is_{\perp}\gamma^1\gamma^2$, respectively. The projectors on the corresponding subspaces are given by

$$\mathscr{P}_{s_0,s_{12}} = \frac{1}{4}(1 + s_0\gamma_0)(1 + s_{12}is_{\perp}\gamma^1\gamma^2), \tag{5.19}$$

with $s_0, s_{12} = \pm 1$. By making use of this complete set of projectors in Dirac space, the translationally invariant part of the Green's function can be rewritten in the following explicit form:[136]

$$
\begin{aligned}
\widetilde{G}(\omega;\mathbf{r}) &= i\frac{e^{-\xi/2}}{2\pi\ell^2}\sum_{n=0}^{\infty}\sum_{\sigma=\pm1}\sum_{s_0=\pm1}\left\{\frac{s_0(\omega+\mu_{n,\sigma})-\tilde{\Delta}_{n,\sigma}}{(\omega+\mu_{n,\sigma})^2-E_{n,\sigma}^2}\left[\delta_{-\sigma}^{s_0}L_n(\xi)+\delta_{+\sigma}^{s_0}L_{n-1}(\xi)\right]\right.\\
&\quad\left.+\frac{i\varepsilon_{\ell}}{\ell}(\gamma\cdot\mathbf{r})\frac{f_{n,\sigma}-s_0 g_{n,\sigma}}{(\omega+\mu_{n,\sigma})^2-E_{n,\sigma}^2}L_{n-1}^1(\xi)\right\}\mathscr{P}_{s_0,s_0\sigma}, \tag{5.20}
\end{aligned}
$$

where $L_n^{\alpha}(\xi)$ are Laguerre polynomials [by definition, $L_n^0(\xi) \equiv L_n(\xi)$], and $\varepsilon_{\ell} \equiv \hbar v_F/\ell$ is the Landau energy scale. We also introduced the following short-hand notations:

$$\xi = \frac{(\mathbf{r}-\mathbf{r}')^2}{2\ell^2}, \tag{5.21}$$

and

$$\mu_{n,\sigma} = \mu_n + \sigma\tilde{\mu}_n, \qquad \tilde{\Delta}_{n,\sigma} = \tilde{\Delta}_n + \sigma\Delta_n, \tag{5.22}$$

$$f_{n,\sigma} = f_n + \sigma\tilde{f}_n, \qquad g_{n,\sigma} = g_n + \sigma\tilde{g}_n. \tag{5.23}$$

Note that, by definition, the Laguerre polynomials $L_n^{\alpha}(\xi)$ with negative n are identically zero. The quasiparticle energies in the lowest and higher Landau levels are determined

81

by

$$E_{0,\sigma} \;=\; \sigma\tilde{\Delta}_{0,\sigma} = \Delta_0 + \sigma\tilde{\Delta}_0, \tag{5.24}$$

$$E_{n,\sigma} \;=\; \sqrt{2n\varepsilon_\ell^2\left[f_{n,\sigma}^2 - g_{n,\sigma}^2\right] + \tilde{\Delta}_{n,\sigma}^2}, \quad (n \geq 1). \tag{5.25}$$

Here $\sigma = \pm 1$ is the eigenvalue of $is_\perp\gamma^0\gamma^1\gamma^2 \equiv s_\perp\gamma_3\gamma_5$, which up to the overall sign $s_\perp$ is the quantum number associated with the valley.

Treating all Landau levels separately, it is convenient to introduce the following spectral representation of the Green's function,

$$\widetilde{G}(i\omega_m,\mathbf{r}) = i\sum_{n=0}^{\infty}\sum_{\sigma=\pm 1}\int_{-\infty}^{\infty}\frac{d\omega}{2\pi}\frac{A_{n,\sigma}(\omega;\mathbf{r})}{i\omega_m + \mu_{n,\sigma} - \omega}. \tag{5.26}$$

where $A_{n,\sigma}(\omega,\mathbf{r}) = \widetilde{G}_{n,\sigma}(\omega + i0;\mathbf{r}) - \widetilde{G}_{n,\sigma}(\omega - i0;\mathbf{r})$ and $\widetilde{G}_{n,\sigma}(\omega + i0;\mathbf{r})$ is the n-σ contribution to the Green's function (5.20), calculated at vanishing $\mu_{n,\sigma}$.

For the Green's function in Eq. (5.20), in which all dynamical parameters are assumed to be real, the spectral functions $A_{n,\sigma}(\omega,\mathbf{r})$ will be given in terms of δ-functions with nonzero values only at exact positions of Landau levels. In real systems, of course, Landau levels have nonzero widths. In order to describe this important property, we will introduce phenomenological width parameters $\Gamma_{n,\sigma}$ which may depend on the frequency ω, the Landau level index n, and the valley index σ. We do this by replacing the δ-functions in the spectral functions with the Lorentzian distributions of nonzero widths $\Gamma_{n,\sigma}$, i.e.,

$$
\begin{aligned}
A_{n,\sigma}(\omega;\mathbf{r}) \;=\; & \frac{e^{-\xi/2}}{2\pi\ell^2}\sum_{s_0=\pm 1}\sum_{\lambda=\pm 1}\sum_{\eta=\pm 1}\frac{i\eta}{2E_{n,\sigma}}\left\{\frac{s_0 E_{n,\sigma} + \lambda\Delta_{n,\sigma}}{\omega + \lambda E_{n,\sigma} + i\eta\Gamma_{n,\sigma}}[\delta_{-\sigma}^{s_0}L_n(\xi)\right. \\
& +\; \delta_{\sigma}^{s_0}L_{n-1}(\xi)] - \frac{i\varepsilon_\ell}{\ell}(\gamma\cdot\mathbf{r})\frac{\lambda(f_{n,\sigma} - s_0 g_{n,\sigma})L_{n-1}^1(\xi)}{\omega + \lambda E_{n,\sigma} + i\eta\Gamma_{n,\sigma}}\left.\right\}\mathscr{P}_{s_0,s_0\sigma}, \tag{5.27}
\end{aligned}
$$

where we introduced an additional sum over λ in order to separate the poles that correspond to negative energy quasiholes and positive energy quasiparticles.

5.3 Calculation of current-current correlation function

In this section, we present the general result for the current-current correlation function in the field-theoretical model of Dirac quasiparticles. We start from the definition in Eq. (5.9) and use the representation of the quasiparticle Green's function in Eq. (5.26) with the spectral functions in Eq. (5.27). After performing the Matsubara summation, we derive the following expression for the current-current correlation function:

$$
\begin{aligned}
\Pi_{ij}(i\Omega_r;0) \;=\;& e^2 v_F^2 \sum_{n,n'} \sum_{\sigma,\sigma'} \int d^2\mathbf{r} \int \frac{d\omega\, d\omega'}{(2\pi)^2} \frac{n_F(\omega - \mu_{n,\sigma}) - n_F(\omega' - \mu_{n',\sigma'})}{\omega - \mu_{n,\sigma} - (\omega' - \mu_{n',\sigma'}) - i\Omega_r} \\
&\times\ \ \mathrm{tr}\left[\gamma^i A_{n,\sigma}(\omega;\mathbf{r})\gamma^j A_{n',\sigma'}(\omega';-\mathbf{r})\right],
\end{aligned}
\tag{5.28}
$$

Then, by calculating the traces and integrating over spatial coordinates, we derive

$$
\begin{aligned}
\Pi_{ij}(i\Omega_r;0) \;=\;& \frac{e^2 \varepsilon_\ell^2}{2\pi} \sum_{n,n'} \sum_{s_0,\sigma} \int \frac{d\omega\, d\omega'}{(2\pi)^2} \frac{n_F(\omega - \mu_{n,\sigma}) - n_F(\omega' - \mu_{n',\sigma})}{\omega - \mu_{n,\sigma} - (\omega' - \mu_{n',\sigma}) - i\Omega_r} \\
&\times\ \sum_{\lambda,\lambda'} \sum_{\eta,\eta'} \frac{\eta\eta'}{4E_{n,\sigma}E_{n',\sigma}} \frac{(E_{n,\sigma} + \lambda s_0 \Delta_{n,\sigma})(E_{n',\sigma} - \lambda' s_0 \Delta_{n',\sigma})}{(\omega + \lambda E_{n,\sigma} + i\eta\Gamma_{n,\sigma})(\omega' + \lambda' E_{n',\sigma} + i\eta'\Gamma_{n',\sigma})} \\
&\times\ \left[(\delta^{ij} + i\varepsilon^{ij})\delta_{-\sigma}^{s_0}\delta_{n,n'-1} + (\delta^{ij} - i\varepsilon^{ij})\delta_{\sigma}^{s_0}\delta_{n-1,n'}\right].
\end{aligned}
\tag{5.29}
$$

(The results for Dirac traces, used in the calculation, are given in Appendix D.) In terms of the tensor structure, this function has only two types of terms,

$$
\Pi_{ij}(i\Omega_r;0) \equiv \delta^{ij}\Pi_{xx}(i\Omega_r;0) + \varepsilon^{ij}\Pi_{xy}(i\Omega_r;0).
\tag{5.30}
$$

The explicit forms of both diagonal and off-diagonal terms are obtained after integrating over the frequencies. The results read

$$
\begin{aligned}
\Pi_{xx}(i\Omega_r;0) \;=\;& \frac{e^2 \varepsilon_\ell^2}{2\pi} \sum_{n=0}^{\infty} \sum_{\sigma=\pm 1} \sum_{\lambda,\lambda'=\pm 1} \frac{(E_{n,\sigma} - \lambda\sigma\Delta_{n,\sigma})(E_{n+1,\sigma} + \lambda'\sigma\Delta_{n+1,\sigma})}{4E_{n,\sigma}E_{n+1,\sigma}} \\
&\times\ \left[\mathscr{I}_{n,n+1}^{\lambda\lambda'}(i\Omega_r) + \mathscr{I}_{n+1,n}^{\lambda'\lambda}(i\Omega_r)\right],
\end{aligned}
\tag{5.31}
$$

$$
\begin{aligned}
\Pi_{xy}(i\Omega_r;0) \;=\;& i\frac{e^2 \varepsilon_\ell^2}{2\pi} \sum_{n=0}^{\infty} \sum_{\sigma=\pm 1} \sum_{\lambda,\lambda'=\pm 1} \frac{(E_{n,\sigma} - \lambda\sigma\Delta_{n,\sigma})(E_{n+1,\sigma} + \lambda'\sigma\Delta_{n+1,\sigma})}{4E_{n,\sigma}E_{n+1,\sigma}} \\
&\times\ \left[\mathscr{I}_{n,n+1}^{\lambda\lambda'}(i\Omega_r) - \mathscr{I}_{n+1,n}^{\lambda'\lambda}(i\Omega_r)\right].
\end{aligned}
\tag{5.32}
$$

In the last two expressions, we made use of the following short-hand notation for the results of integrations:

$$
\begin{aligned}
\mathscr{I}_{n,n'}^{\lambda\lambda'}(i\Omega_r) &= \int \frac{d\omega d\omega'}{(2\pi)^2} \frac{n_F(\omega-\mu_{n,\sigma}) - n_F(\omega'-\mu_{n',\sigma})}{\omega - \mu_{n,\sigma} - (\omega'-\mu_{n',\sigma}) - i\Omega_r} \\
&\times \sum_{\eta,\eta'} \frac{\eta\eta'}{(\omega + \lambda E_{n,\sigma} + i\eta\Gamma_{n,\sigma})(\omega' + \lambda' E_{n',\sigma} + i\eta'\Gamma_{n',\sigma})} \\
&= \frac{S_{nn'}^{\lambda\lambda'}(i\Omega_r)}{\lambda E_{n,\sigma} + \mu_{n,\sigma} - i\Gamma_{n,\sigma} - (\lambda' E_{n',\sigma} + \mu_{n',\sigma} - i\Gamma_{n',\sigma}) + i\Omega_r} \\
&+ \frac{R_{nn'}^{\lambda\lambda'}(i\Omega_r)}{\lambda E_{n,\sigma} + \mu_{n,\sigma} + i\Gamma_{n,\sigma} - (\lambda' E_{n',\sigma} + \mu_{n',\sigma} + i\Gamma_{n',\sigma}) + i\Omega_r} \\
&+ \frac{Z_{nn'}^{\lambda\lambda'}(i\Omega_r)}{\lambda E_{n,\sigma} + \mu_{n,\sigma} + i\Gamma_{n,\sigma} - (\lambda' E_{n',\sigma} + \mu_{n',\sigma} - i\Gamma_{n',\sigma}) + i\Omega_r}, \quad (5.33)
\end{aligned}
$$

where

$$
\begin{aligned}
S_{nn'}^{\lambda\lambda'}(i\Omega_r) &= \frac{i}{2\pi}\left[\psi\left(\frac{1}{2} - \frac{\lambda' E_{n',\sigma} + \mu_{n',\sigma} - i\Gamma_{n',\sigma} - i\Omega_r}{2\pi i T}\right) - \psi\left(\frac{1}{2} - \frac{\lambda E_{n,\sigma} + \mu_{n,\sigma} - i\Gamma_{n,\sigma}}{2\pi i T}\right)\right], \\
R_{nn'}^{\lambda\lambda'}(i\Omega_r) &= \frac{i}{2\pi}\left[\psi\left(\frac{1}{2} + \frac{\lambda E_{n,\sigma} + \mu_{n,\sigma} + i\Gamma_{n,\sigma} + i\Omega_r}{2\pi i T}\right) - \psi\left(\frac{1}{2} + \frac{\lambda' E_{n',\sigma} + \mu_{n',\sigma} + i\Gamma_{n',\sigma}}{2\pi i T}\right)\right], \\
Z_{nn'}^{\lambda\lambda'}(i\Omega_r) &= \frac{i}{2\pi}\left[-\psi\left(\frac{1}{2} + \frac{\lambda E_{n,\sigma} + \mu_{n,\sigma} + i\Gamma_{n,\sigma} + i\Omega_r}{2\pi i T}\right) + \psi\left(\frac{1}{2} + \frac{\lambda E_{n,\sigma} + \mu_{n,\sigma} + i\Gamma_{n,\sigma}}{2\pi i T}\right)\right. \\
&\left. -\psi\left(\frac{1}{2} - \frac{\lambda' E_{n',\sigma} + \mu_{n',\sigma} - i\Gamma_{n',\sigma} - i\Omega_r}{2\pi i T}\right) + \psi\left(\frac{1}{2} - \frac{\lambda' E_{n',\sigma} + \mu_{n',\sigma} - i\Gamma_{n',\sigma}}{2\pi i T}\right)\right].
\end{aligned}
$$

$$(5.34)$$

In the zero temperature limit, in particular, these functions become

$$
S_{nn'}^{\lambda\lambda'}(\Omega) = \frac{i}{2\pi} \ln \frac{\lambda' E_{n',\sigma} + \mu_{n',\sigma} - i\Gamma_{n',\sigma} - \Omega - i\varepsilon}{\lambda E_{n,\sigma} + \mu_{n,\sigma} - i\Gamma_{n,\sigma}}, \quad (5.35)
$$

$$
R_{nn'}^{\lambda\lambda'}(\Omega) = \frac{i}{2\pi} \ln \frac{\lambda E_{n,\sigma} + \mu_{n,\sigma} + i\Gamma_{n,\sigma} + \Omega + i\varepsilon}{\lambda' E_{n',\sigma} + \mu_{n',\sigma} + i\Gamma_{n',\sigma}}, \quad (5.36)
$$

$$
Z_{nn'}^{\lambda\lambda'}(\Omega) = \frac{i}{2\pi}\left[\ln \frac{\lambda E_{n,\sigma} + \mu_{n,\sigma} + i\Gamma_{n,\sigma}}{\lambda E_{n,\sigma} + \mu_{n,\sigma} + i\Gamma_{n,\sigma} + \Omega + i\varepsilon} \right.
$$
$$
\left. + \ln \frac{\lambda' E_{n',\sigma} + \mu_{n',\sigma} - i\Gamma_{n',\sigma}}{\lambda' E_{n',\sigma} + \mu_{n',\sigma} - i\Gamma_{n',\sigma} - \Omega - i\varepsilon}\right]. \quad (5.37)
$$

In the derivation, we used the following asymptote of the ψ-function: $\psi(z) \simeq \ln(z) + O(1/z)$ for $z \to \infty$.

5.4   Numerical result

In this section, we calculate numerical results for the Faraday rotation angle as well as the magneto-optical transmission for several different model parameters. Let us assume that n_0 and $n_s(\Omega)$ are the refractive indices of vacuum and substrate. In general, the refractive index of the substrate is dependent on the frequency of the light Ω. From supplementary information of Ref. [134] we find that n_s can be treated as a constant $n_s(\Omega) \approx 2.6$ at low frequencies, i.e., $0 < \Omega < 60$ Hz. So, we use this approximation in our calculations.

Our numerical results for the transmission ratio $T(B)/T(0)$ at zero temperature are shown in Fig. 5.2 for three different values of the quasiparticle width: $\Gamma = 1$ meV, $\Gamma = 5$ meV, and $\Gamma = 10$ meV. Different lines represent the results for different values of the magnetic field, ranging from $B = 1$ T to $B = 10$ T with the increment of 1 T. The corresponding numerical results for the Faraday rotation angle θ are shown in Fig. 5.3.

As we see, the deviations of the transmission ratio and the Faraday rotation angle from the corresponding zero-field results become larger with increasing the value of the magnetic field. These result agree well with the experiment data when $\Gamma = 5$ meV. This value is less than a naive estimate for the quasiparticle width of 10 meV in Ref. [134]. In our theoretical study we find that the effect of temperature (up to about 300 K) becomes noticeable only when Γ is of the order of, or smaller than about 1 meV. When the best fit value $\Gamma = 5$ meV is used, then, the effect remains very small and the $T = 0$ results give a very good approximation of the experimental data even at room temperature (300 K).

We also find that the sign of the Faraday rotation angle changes from positive to negative at a certain photon frequency, depending on the strength of the magnetic field. As discussed in Ref. [134], this is explained by the classical cyclotron resonance
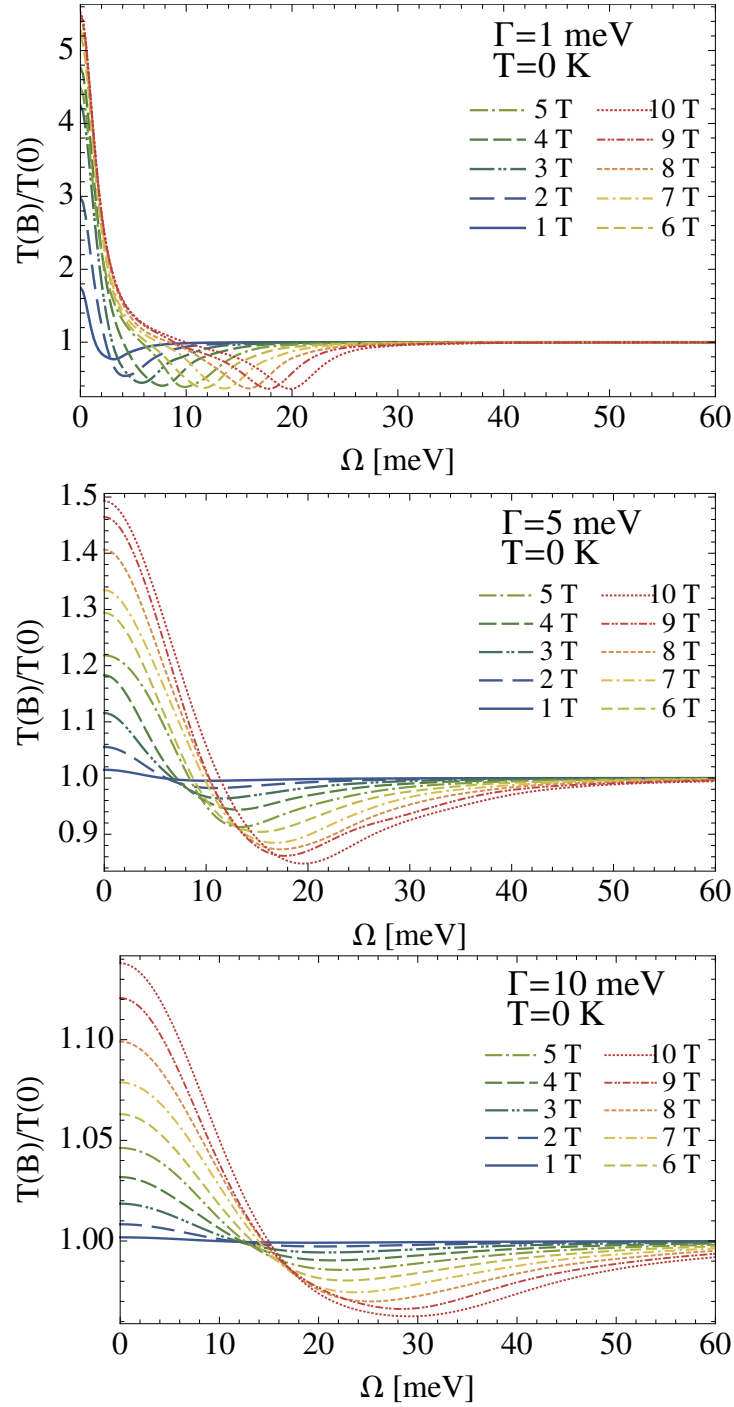
Figure 5.2: Transmission for three different values of the quasiparticle width: $\Gamma = 1$ meV, $\Gamma = 5$ meV, and $\Gamma = 10$ meV, and zero temperature.
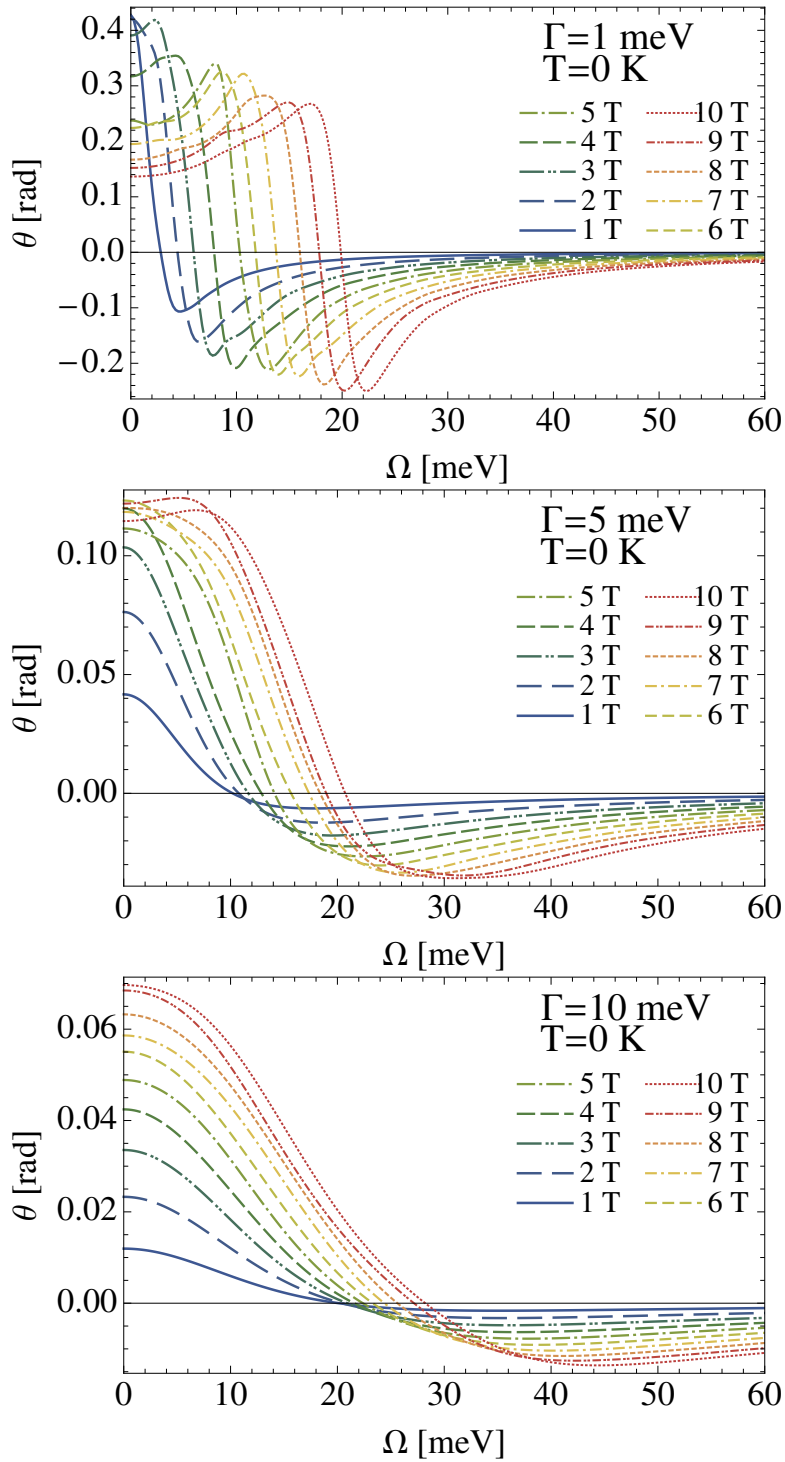
Figure 5.3: Faraday rotation angle for three different values of the quasiparticle width: $\Gamma = 1$ meV, $\Gamma = 5$ meV, and $\Gamma = 10$ meV, and zero temperature.

effect. The classical Drude formulae for the conductivity tensor read:

$$\sigma_{xx}(\Omega, B) = \frac{2D}{\pi} \frac{1/\tau - i\Omega}{\Omega_c^2 - (\Omega + i/\tau)^2},$$ (5.38a)

$$\sigma_{xy}(\Omega, B) = -\frac{2D}{\pi} \frac{\Omega_c}{\Omega_c^2 - (\Omega + i/\tau)^2},$$ (5.38b)

where D is the Drude weight, Ω_c is the cyclotron frequency (which is positive for electrons and negative for holes) and τ is the scattering time. By using this expression in Eq. (5.1) we can find that there is a photon frequency $\Omega_{\star,B}$, where the sign of the Faraday rotation angle should change. This is a universal feature associated with the photon absorbtion near a resonance frequency.

5.5   Discussion

In this chapter we present a detailed derivation of the Faraday effect and the magneto-optical transmission/absorption in the semi-classical and the quantum Hall regimes by using a unified approach [137]. We obtained the dependence of the magneto-optical properties on the light frequency. Our theoretical calculation are in excellent qualitative as well as a good quantitative agreement with the recent experimental results for graphene on a SiC substrate [134, 138]. This is quite remarkable after taking into account that there is only one fit parameter (i.e., the quasiparticle width) in the model. In particular, our simple quantum microscopic model suggests that the width of quantum states in the setup of Ref. [134] must be about $\Gamma = 5$ meV, which is two times smaller than the rough estimate, proposed in the original analysis of the experimental results.

The large magnitude of Faraday angle suggests that there exists a possibility of a strongly pronounced inverse Faraday effect. The effect is seen as a generation of a static magnetic field (or magnetization) when a material is irradiated with a circularly polarized electromagnetic wave [139, 140]. Using general arguments about the free energy in solids, Pershan predicted that the magnetization generated would be related to the same magneto-optical tensor that characterizes the long established Faraday ef-

fect. Further to this, Pershan and his co-workers went on to test these predictions and established experimentally that magnetization could indeed be generated by circularly polarized light. (See Ref. [141] for more details.)

CHAPTER 6

SUMMARY AND OUTLOOK

6.1   Summary

In the introduction we have argued that in order to understand systems of relativistic matter in nature, it might be important to study the properties of relativistic matter under several extreme physics environments. We have introduced two examples where relativistic matter may exist. One is the interior of neutron stars where the density is so high that the corresponding state of matter is necessarily in the relativistic regime. The other is graphene where the quasiparticle can be treated as massless relativistic particles.

In Chapter 2 and 3 we studied the rate of nonleptonic weak processes as well as the bulk viscosity in four transverse spin-one color superconducting phase of strange quark matter. In the calculation of bulk viscosity we took into account the interplay between the nonleptonic and semileptonic week processes. In agreement with previous studies, it is found that the inclusion of the semi-leptonic processes may result in non-negligible corrections to the bulk viscosity in a narrow window of temperatures. The effect is generally more pronounced for pulsars with longer periods. Compared to the normal phase, however, this effect due to the semi-leptonic processes is less pronounced in spin-one color superconductors. Assuming that the critical temperature of the phase transition is much larger than 40 keV, the main effect of spin-one color superconductivity in a wide range of temperatures is an overall increase of the bulk viscosity with respect to the normal phase. The corresponding enhancement factor reaches up to about 9 in the polar and A-phases, about 25 in the planar phase and about 29 in the CSL phase. This factor is determined by the suppression of the nonleptonic rate in color-superconducting matter and, therefore, may be even larger if all quark quasiparticles happen to be gapped.

In Chapter 4, the bulk viscosity of cold, dense three-flavor quark matter was calculated as a function of temperature and the amplitude of density oscillations. The study is also extended to the case of two different types of anharmonic oscillations of density. We pointed several qualitative effects due to the anharmonicity, although quantitatively they appear to be relatively small. We also found that, in most regions of the parameter space, with the exception of the case of a very large amplitude of density oscillations (i.e., 10% and above), nonlinear effects and the anharmonicity have a small effect on the interplay of the nonleptonic and semileptonic processes in the bulk viscosity.

The bulk viscosity calculations in chapters 3 and 4 may give important phenomenological information. By comparing theoretical predictions with the observation data, it can help understanding the equation of state of dense matter present in neutron stars. Firstly, the damping time scale, which depends on the viscosity determines if the r-mode is unstable. The instability of the r-mode can lead to a transient state with large emission of gravitational waves potentially detectable by Advanced LIGO [63]. Secondly, one can use the observational data for the distribution of pulsar in the plane of frequency and temperature. The empty regions in the diagram should point to the forbidden sets of parameters. By comparing these with the theoretically predicted regions of instability will provide the constraint on possible phases of dense matter inside pulsars.

We also studied optical conductivity and screening effects of monolayer graphene in a strong magnetic field responsible for spontaneous symmetry breaking of an approximate flavor symmetry and causing the anomalous quantum Hall effect. We calculated the Faraday angle and transmission coefficients of different types of order parameters, associated with the quantum Hall ferromagnetism and magnetic catalysis. It is found that the qualitative features in the optical conductivity can unambiguously indicate the

91

microscopic nature of the symmetry breaking patterns. Compare with the experimental data, we found the quasiparticle width is somewhat smaller than with the rough estimate in the experimental paper [134].

6.2 Outlook

In the future, the analysis performed in this thesis can be extended to also study the rates of weak processes and the corresponding the bulk viscosity in other spin-one color supercoducting phases. Indeed, there are several studies [52, 53] suggesting other possible spin-one color supercoductors. While all of them have similarities to the spin-one phases studied here, there are often subtle differences that may lead to quantitative and possibly even qualitative differences in the rates.

Also, it is of interest to extend the study of the bulk viscosity to obtain actual quantitative effects that spin-one color superconductivity has on the reduction of the instability window in the pulsar frequency and temperature plane. This can be done along the lines of Refs. [128, 129, 142] in order to get a better understanding of the implications of our results for physics of neutron stars. It would be ideal if the next study is done with the proper analysis of possible anharmonic effects. In the preliminary study in Chapter 4, we considered only a toy model to introduce the anharmonic oscillations. Eventually, it is interesting to study more realistic types of density oscillations that result from the actual nonlinear dynamics of stellar r-modes, produced by the gravitational emission.

In connection to our study of the magneto-optical properties of graphene, the next step will be the use of a more realistic model, in which all subtleties of the frequency and temperature dependence of the quasiparticle width are properly taken into account. While our toy model does a good job of qualitative description of the magneto-optical properties of graphene, it may fall short of being quantitatively reliable in extreme regimes of high temperature and frequency. In order to become truly predictive,

the model should be also generalized to take into account the effects of wave-function

and Fermi-velocity renormalization.

REFERENCES

[1] A. Hewish, S.G. Bell, J.D.H. Pilkington, P.F. Scott, and R.A. Collins, Nature **217**, 709 (1968).

[2] F. Pacini, Nature **219**, 145 (1968).

[3] T. Gold, Nature **218**, 731 (1968).

[4] R. C. Tolman, Phys. Rev. **55**, 364 (1939).

[5] J. R. Oppenheimer and G. M. Volkov, Phys. Rev. **55**, 374 (1939).

[6] J. M. Lattimer and M. Prakash, Phys. Rept. **442**, 109 (2007) [arXiv:astro-ph/0612440].

[7] C. Kouveliotou, S. Dieters, T. Strohmayer, J. van Paradijs, G. J. Fishman, C. A. Meegan, K. Hurley and J. Kommers *et al.*, Nature **393**, 235 (1998).

[8] C. Kouveliotou, T. Strohmayer, K. Hurley, J. van Paradijs, M. H. Finger, S. Dieters, P. Woods and C. Thompson *et al.*, Astrophys. J. **510**, L115 (1999) [astro-ph/9809140].

[9] R. C. Duncan and C. Thompson, Astrophys. J. **392**, L9 (1992).

[10] C. Thompson and R. C. Duncan, Astrophys. J. **408**, 194 (1993).

[11] H. Kamerlingh Onnes, Comm. Leiden **120b** (1911).

[12] J. Bardeen, L.N. Cooper, and J.R. Schrieffer, Phys. Rev. **108**, 1175 (1957).

[13] J.G. Bednorz and K.A. Müller, Z. Physik **B64**, 189 (1986).

[14] K. A. Müller and J. G. Bednorz, Science **237**, 1133 (1987).

[15] C. W. Chu et al. Nature **365**, 323 (1993).

[16] W. Meissner and R. Ochsenfeld, Naturwissenschaften **21**, 787 (1933).

[17] H. Fröhlich, Phys. Rev. **79**, 845 (1950).

[18] V.L. Ginzburg and L.D. Landau, Zh. Eksp. Teor. Fiz. **20**, 1044 (1950).

[19] A.P Mackenzie and Y. Maeno, Rev. Mod. Phys. **75**, 657 (2003).

[20] M. Sigrist and K. Ueda, Rev. Mod. Phys. **63**, 239 (1991).

[21] K. Deguchi, Z.Q. Mao, H. Yaguchi, and Y. Maeno, Phys. Rev. Lett. **92**, 047002 (2004).

[22] P.L. Kapitza, Nature **141**, 47 (1938).

[23] D.D. Osheroff, R.C. Richardson, and D.M. Lee, Phys. Rev. Lett. **28** 885 (1972).

[24] A.J. Leggett, Rev. Mod. Phys. **47**, 331 (1975).

[25] D. Bailin and A. Love, Phys. Lett. B **137**, 348 (1984).

[26] K. Rajagopal and F. Wilczek, In Shifman, M. (ed.): At the frontier of particle physics, vol. 3 2061-2151 [hep-ph/0011333].

[27] M. G. Alford, Ann. Rev. Nucl. Part. Sci. **51**, 131 (2001) [arXiv:hep-ph/0102047].

[28] D. K. Hong, Acta Phys. Polon. B **32**, 1253 (2001) [arXiv:hep-ph/0101025].

[29] D. H. Rischke, Prog. Part. Nucl. Phys. **52**, 197 (2004) [arXiv:nucl-th/0305030].

[30] T. Schäfer, arXiv:hep-ph/0304281.

[31] S. Reddy, Acta Phys. Polon. B **33**, 4101 (2002) [arXiv:nucl-th/0211045].

[32] M. Buballa, Phys. Rept. **407**, 205 (2005) [arXiv:hep-ph/0402234].

[33] I. A. Shovkovy, Found. Phys. **35**, 1309 (2005) [arXiv:nucl-th/0410091].

[34] M. G. Alford, A. Schmitt, K. Rajagopal and T. Schäfer, Rev. Mod. Phys. **80**, 1455 (2008) [arXiv:0709.4635 [hep-ph]].

[35] H.D. Politzer, Phys. Rev. Lett. **30**, 1346 (1973).

[36] D.J. Gross and F. Wilczek, Phys. Rev. D **8**, 3633 (1973).

[37] D.J. Gross and F. Wilczek, Phys. Rev. D **9**, 980 (1974).

[38] S. B. Rüster, V. Werth, M. Buballa, I. A. Shovkovy and D. H. Rischke, Phys. Rev. D **72**, 034004 (2005).

[39] Y. Nambu and G. Jona-Lasinio, Phys. Rev. **122**, 345 (1961).

[40] P. de Forcrand, PoS LAT **2009**, 010 (2009) [arXiv:1005.0539 [hep-lat]].

[41] M. G. Alford, K. Rajagopal and F. Wilczek, Nucl. Phys. B **537**, 443 (1999) [hep-ph/9804403].

[42] I. A. Shovkovy and L. C. R. Wijewardhana, Phys. Lett. B **470**, 189 (1999) [hep-ph/9910225].

[43] T. Schäfer, Nucl. Phys. B **575**, 269 (2000) [hep-ph/9909574].

[44] K. Rajagopal and A. Schmitt, Phys. Rev. D **73**, 045003 (2006) [hep-ph/0512043].

[45] A. Schmitt, Ph.D. thesis, [arXiv:nucl-th/0405076].

[46] D. Bailin and A. Love, Nucl. Phys. **B190**, 175 (1981).

[47] R. D. Pisarski and D. H. Rischke, Phys. Rev. D **61**, 051501 (2000).

[48] M. Iwasaki and T. Iwado, Phys. Lett. B **350**, 163 (1995).

[49] T. Schäfer, Phys. Rev. D **62**, 094007 (2000).

[50] M. G. Alford, J. A. Bowers, J. M. Cheyne, and G. A. Cowan, Phys. Rev. D **67**, 054018 (2003) [arXiv:hep-ph/0210106].

[51] A. Schmitt, Q. Wang, and D. H. Rischke, Phys. Rev. Lett. **91**, 242301 (2003).

[52] A. Schmitt, Phys. Rev. D **71**, 054016 (2005) [arXiv:nucl-th/0412033].

[53] T. Brauner, Phys. Rev. D **78**, 125027 (2008);

[54] T. Brauner, J. Y. Pang and Q. Wang, arXiv:0909.4201 [hep-ph].

[55] T. Schäfer, Phys. Rev. D **62**, 094007 (2000) [arXiv:hep-ph/0006034].

[56] A. Schmitt, I. A. Shovkovy and Q. Wang, Phys. Rev. D **73**, 034012 (2006) [arXiv:hep-ph/0510347].

[57] T. D. Lee and C. N. Yang, Phys. Rev. **104**, 254 (1956).

[58] P. W. Higgs, Phys. Rev. Lett. **13**, 508 (1964).

[59] S. Chandrasekhar, Phys. Rev. Lett. **24**, 611 (1970); Astrophys. J. **161**, 561 (1970).

[60] J. Friedman and B. Schutz, Astrophys. J. **222**, 281 (1978).

[61] N. Andersson, Astrophys. J. **502**, 708 (1998).

[62] J. L. Friedman and S. M. Morsink, Astrophys. J. **502**, 714 (1998).

[63] N. Andersson and K. D. Kokkotas, Int. J. Mod. Phys. D **10**, 381 (2001).

[64] L. Lindblom, [arXiv:astro-ph/0101136].

[65] B. A. Sa'd, I. A. Shovkovy and D. H. Rischke, Phys. Rev. D **75**, 065016 (2007) [arXiv:astro-ph/0607643].

[66] C. Manuel, A. Dobado and F. J. Llanes-Estrada, JHEP **0509**, 076 (2005) [arXiv:hep-ph/0406058].

[67] M. G. Alford, M. Braby, S. Reddy and T. Schafer, Phys. Rev. C **75**, 055209 (2007) [arXiv:nucl-th/0701067].

[68] C. Manuel and F. J. Llanes-Estrada, JCAP **0708**, 001 (2007) [arXiv:0705.3909 [hep-ph]].

[69] M. G. Alford and A. Schmitt, AIP Conf. Proc. **964**, 256 (2007) [arXiv:0709.4251 [nucl-th]].

[70] L. Lindblom, B. J. Owen and S. M. Morsink, Phys. Rev. Lett. **80**, 4843 (1998) [gr-qc/9803053].

[71] Q. D. Wang and T. Lu, Phys. Lett. **148B**, 211 (1984).

[72] R. F. Sawyer, Phys. Lett. B **233**, 412 (1989).

[73] J. Madsen, Phys. Rev. D **46**, 3290 (1992).

[74] Z. Xiaoping, L. Xuewen, K. Miao, and Y. Shuhua, Phys. Rev. C **70**, 015803 (2004).

[75] Z. Xiaoping, K. Miao, L. Xuewen, and Y. Shuhua, Phys. Rev. C **72**, 025809 (2005).

[76] X.-p. Zheng, S.-h. Yang, and J.-r. Li, Phys. Lett. B **548**, 29 (2002).

[77] B. A. Sa'd, I. A. Shovkovy and D. H. Rischke, Phys. Rev. D **75**, 125004 (2007) [arXiv:astro-ph/0703016].

[78] E. Flowers, M. Ruderman and P. Sutherland, Astrophys. J. **205**, 541 (1976).

[79] J. N. Bahcall and R. A. Wolf, Phys. Rev. **140**, B1452 (1965).

[80] C. J. Pethick, Rev. Mod. Phys. **64**, 1133 (1992).

[81] D. G. Yakovlev and C. J. Pethick, Ann. Rev. Astron. Astrophys. **42**, 169 (2004) [astro-ph/0402143].

[82] P. R. Wallace, Phys. Rev. **71**, 622634 (1947).

[83] J. W. McClure, Phys. Rev. **108**, 612618(1957).

[84] P. R. Schroeder, M. S. Dresselhaus, and A. Javan, Phys. Rev. Lett. **20**, 1292 (1968).

[85] Semenoff, G. W., Phys. Rev. Lett.**53**, 2449 (1984).

[86] D. P. DiVincenzo and E. J. Mele, Phys. Rev. B **29**, 1685 (1984).

[87] K. S. Novoselov, A. K. Geim, S. V. Morozov, D. Jiang, Y. Zhang, S. V. Dubonos, I. V. Grigorieva,A. A. Firsov, Science **306**, 666 (2004).

[88] A. K. Geim and K. S. Novoselov, Nature Materials **6**, 183 (2007).

[89] K. S. Novoselov, A. K. Geim, S. V. Morozov, D. Jiang, M. I. Katsnelson, I. V. Grigorieva, S. V. Dubonos, A. A. Firsov, Nature **438**, 197 (2005).

[90] Zhang, Y. et al, Nature (London) **438**, 201 (2005).

[91] V. P. Gusynin and S. G. Sharapov, Phys. Rev. Lett. **95**, 146801 (2005);

[92] V. P. Gusynin and S. G. Sharapov, Phys. Rev. B **73**, 245411 (2006).

[93] Y. Zheng and T. Ando, Phys. Rev. B **65**, 245420 (2002).

[94] Zhang, Y. et al, Phys Rev Lett **96**, 136806 (2006).

[95] Du, X. et al, Nature **462**, 192 (2009).

[96] Bolotin, K. et al, Nature **462**, 196 (2009).

[97] Gerald D. Mahan, *Many Particle Physics, 3rd edition*, Springer, 2010, pp.163-168.

[98] A. Sedrakian and A. E. L. Dieperink, Phys. Rev. D **62**, 083002 (2000).

[99] A. Sedrakian, Phys. Lett. B **607**, 27 (2005).

[100] A. Sedrakian, Prog. Part. Nucl. Phys. **58**, 168 (2007).

[101] M. G. Alford and A. Schmitt, J. Phys. G **34**, 67 (2007) [arXiv:nucl-th/0608019].

[102] L. P. Kadanoff and G. Baym, *Quantum Statistical Mechanics* (Benjamin, New York, 1962).

[103] J. Madsen, Phys. Rev. D **47**, 325 (1993).

[104] For normalized values of the λ-rates, see EPAPS supplementary material at http://link.aps.org/supple-mental/10.1103/PhysRevD.81.045021 .

[105] S. Weinzierl, arXiv:hep-ph/0006269.

[106] X. Wang, H. Malekzadeh and I. A. Shovkovy, Phys. Rev. D **81**, 045021 (2010) [arXiv:0912.3851 [hep-ph]].

[107] J. Madsen, Phys. Rev. Lett. **81**, 3311 (1998).

[108] J. D. Anand, N. Chandrika Devi, V. K. Gupta and S. Singh, Pramana **54**, 737 (2000).

[109] J. R. Ellis, E. Gardi, M. Karliner and M. A. Samuel, Phys. Rev. D **54**, 6986 (1996).

[110] N. Iwamoto, Phys. Rev. Lett. **44**, 1637 (1980).

[111] X. Wang and I. A. Shovkovy, Phys. Rev. D **82**, 085007 (2010) [arXiv:1006.1293 [hep-ph]].

[112] A. Schmitt, Q. Wang and D. H. Rischke, Phys. Rev. D **66**, 114010 (2002).

[113] A. Schmitt, Q. Wang and D. H. Rischke, Phys. Rev. Lett. **91**, 242301 (2003).

[114] F. Marhauser, D. Nickel, M. Buballa and J. Wambach, Phys. Rev. D **75**, 054022 (2007).

[115] N. Andersson, Astrophys. J. **502**, 708 (1998).

[116] T. Van Hoolst, Astron. Astrophys. **308**, 66 (1996).

[117] N. Stergioulas and J. A. Font, Phys. Rev. Lett. **86**, 1148 (2001).

[118] L. Lindblom, J. E. Tohline and M. Vallisneri, Phys. Rev. Lett. **86**, 1152 (2001).

[119] A. K. Schenk, P. Arras, E. E. Flanagan, S. A. Teukolsky and I. Wasserman, Phys. Rev. D **65**, 024001 (2002).

[120] P. Arras, E. E. Flanagan, S. M. Morsink, A. K. Schenk, S. A. Teukolsky and I. Wasserman, Astrophys. J. **591**, 1129 (2003).

[121] M. Gabler, U. Sperhake and N. Andersson, Phys. Rev. D **80**, 064012 (2009).

[122] M. G. Alford, S. Mahmoodifar and K. Schwenzer, J. Phys. G **37**, 125202 (2010).

[123] P. Haensel, Astron. Astrophys. **262**, 131 (1992).

[124] A. Reisenegger, Astrophys. J. **442**, 749 (1995).

[125] J. Madsen, Phys. Rev. D **46**, 3290 (1992).

[126] H. Dong, N. Su and Q. Wang, Phys. Rev. D **75**, 074016 (2007).

[127] X.-G. Huang, M. Huang, D. H. Rischke and A. Sedrakian, Phys. Rev. D **81**, 045015 (2010).

[128] J. Madsen, Phys. Rev. Lett. **85**, 10 (2000).

[129] P. Jaikumar, G. Rupak and A. W. Steiner, Phys. Rev. D **78**, 123007 (2008).

[130] H. Heiselberg and C. J. Pethick, Phys. Rev. D **48**, 2916 (1993).

[131] M. G. Alford, M. Braby and S. Mahmoodifar, Phys. Rev. C **81**, 025202 (2010).

[132] I. A. Shovkovy and X. Wang, New J. Phys. **13**, 045018 (2011) [arXiv:1012.0354 [nucl-th]].

[133] T. Morimoto, Y. Hatsugai, and H. Aoki, Phys. Rev. Lett. **103**, 116803 (2009); Physica E **42**, 751 (2010).

[134] I. Crassee, et. al, Nature Physics **7**, 48 (2011).

[135] K. W. Chiu, T. K. Lee, J. J. Quinn, Surface Science **58**, 182 (1976).

[136] E. V. Gorbar, V. P. Gusynin, V. A. Miransky and I. A. Shovkovy, Phys. Scripta T **146**, 014018 (2012) [arXiv:1105.1360 [cond-mat.mes-hall]].

[137] I. A. Shovkovy and X. Wang, "Analysis of Faraday rotation and magneto-optical transmission in monolayer graphene," in preparation.

[138] I. Crassee, et. al, Phys. Rev. B **84**, 035103 (2011).

[139] L. P. Pitaevskii, Sov. Phys. JETP **12**, 1008 (1961).

[140] J.P. van der Ziel, P.S. Pershan, and L.D. Malmstrom Phys. Rev. Lett **15**, 190(1965).

[141] A. H. M. Reid, A. V. Kimei, A. Kirilyuk, J.F Gregg and Th. Rasing Phys. Rev. B**81**, 104404 (2010).

[142] N. Andersson, D. I. Jones and K. D. Kokkotas, Mon. Not. Roy. Astron. Soc. **337**, 1224 (2002).

[143] A. D. Polyanin and V. F. Zaitsev, *Handbook of exact solutions for ordinary differential equations, Second Edition*, (Chapman and Hall, 2002), p. 318.

APPENDIX A

TRACES AND ANGULAR INTEGRATIONS

A.1   Color and Dirac traces

In this appendix, we write down the explicit expressions for the tensor $\mathscr{T}_{\mu\nu}^{rr'}(\hat{\mathbf{p}},\hat{\mathbf{p}}')$, defined by Eq. (2.13). The corresponding results were obtained in Ref. [56]. In general, one finds that

$$\mathscr{T}_{r,r'}^{\mu\nu}(\hat{\mathbf{p}},\hat{\mathbf{p}}') = \mathscr{T}^{\mu\nu}(\hat{\mathbf{p}},\hat{\mathbf{p}}')\omega_{rr'}(\hat{\mathbf{p}},\hat{\mathbf{p}}'), \tag{A.1}$$

where $\omega_{rr'}(\hat{\mathbf{p}},\hat{\mathbf{p}}')$ are the functions determined by a specific color-spin structure of the gap matrix, and

$$\mathscr{T}^{\mu\nu}(\hat{\mathbf{p}},\hat{\mathbf{p}}') \equiv \mathrm{Tr}_D \left[\gamma^\mu (1-\gamma^5)\gamma^0 \Lambda_{\mathbf{p}}^- \gamma^\nu (1-\gamma^5)\gamma^0 \Lambda_{\mathbf{p}'}^- \right]. \tag{A.2}$$

The explicit form of all the components of this tensor can be also found in Ref. [56]. It is more important for us here to note that the following result for the contraction of this tensor with itself is valid:

$$\mathscr{T}^{\mu\nu}(\hat{\mathbf{p}}_4,\hat{\mathbf{p}}_1)\mathscr{T}_{\mu\nu}(\hat{\mathbf{p}}_3,\hat{\mathbf{p}}_2) = 16(1-\hat{\mathbf{p}}_1 \cdot \hat{\mathbf{p}}_2)(1-\hat{\mathbf{p}}_3 \cdot \hat{\mathbf{p}}_4). \tag{A.3}$$

Since an essential information regarding spin-one color-superconducting phases is carried by the $\omega_{rr'}(\hat{\mathbf{p}},\hat{\mathbf{p}}')$ functions, we also quote them here. (For more details, see Ref. [56].)

In the *polar* phase, the $\omega_{rr'}(\hat{\mathbf{p}},\hat{\mathbf{p}}')$ functions do not depend on the quark momenta. They are given by the following expressions:

$$\omega_{11}(\hat{\mathbf{p}},\hat{\mathbf{p}}') = 2, \tag{A.4a}$$

$$\omega_{22}(\hat{\mathbf{p}},\hat{\mathbf{p}}') = 1, \tag{A.4b}$$

$$\omega_{12}(\hat{\mathbf{p}},\hat{\mathbf{p}}') = \omega_{21}(\hat{\mathbf{p}},\hat{\mathbf{p}}') = 0. \tag{A.4c}$$

In the *planar* phase, the explicit form of the $\omega_{rr'}(\hat{\mathbf{p}},\hat{\mathbf{p}}')$ functions reads

$$\omega_{11}(\hat{\mathbf{p}},\hat{\mathbf{p}}') = \frac{1}{2}[3+\eta(\hat{\mathbf{p}},\hat{\mathbf{p}}')], \tag{A.5a}$$

$$\omega_{12}(\hat{\mathbf{p}},\hat{\mathbf{p}}') = \omega_{21}(\hat{\mathbf{p}},\hat{\mathbf{p}}') = \frac{1}{2}[1-\eta(\hat{\mathbf{p}},\hat{\mathbf{p}}')], \tag{A.5b}$$

$$\omega_{22}(\hat{\mathbf{p}},\hat{\mathbf{p}}') = \frac{1}{2}[1+\eta(\hat{\mathbf{p}},\hat{\mathbf{p}}')], \tag{A.5c}$$

where

$$\eta(\hat{\mathbf{p}},\hat{\mathbf{p}}') \equiv \frac{4\hat{p}_z\hat{p}_z' + (\hat{p}_x\hat{p}_x'+\hat{p}_y\hat{p}_y')^2 - (\hat{p}_x\hat{p}_y'-\hat{p}_y\hat{p}_x')^2}{[1+(\hat{p}_z)^2][1+(\hat{p}_z')^2]} . \tag{A.6}$$

In the *A*-phase, there are three different quasiparticle branches ($r = 1,2,3$). Consequently, there are more $\omega_{rr'}(\hat{\mathbf{p}},\hat{\mathbf{p}}')$ functions, i.e.,

$$\omega_{11}(\hat{\mathbf{p}},\hat{\mathbf{p}}') = \frac{1}{2}[1+\mathrm{sgn}(\hat{p}_z)][1+\mathrm{sgn}(\hat{p}_z')], \tag{A.7a}$$

$$\omega_{22}(\hat{\mathbf{p}},\hat{\mathbf{p}}') = \frac{1}{2}[1-\mathrm{sgn}(\hat{p}_z)][1-\mathrm{sgn}(\hat{p}_z')], \tag{A.7b}$$

$$\omega_{12}(\hat{\mathbf{p}},\hat{\mathbf{p}}') = \frac{1}{2}[1+\mathrm{sgn}(\hat{p}_z)][1-\mathrm{sgn}(\hat{p}_z')], \tag{A.7c}$$

$$\omega_{21}(\hat{\mathbf{p}},\hat{\mathbf{p}}') = \frac{1}{2}[1-\mathrm{sgn}(\hat{p}_z)][1+\mathrm{sgn}(\hat{p}_z')], \tag{A.7d}$$

$$\omega_{13}(\hat{\mathbf{p}},\hat{\mathbf{p}}') = \omega_{31}(\hat{\mathbf{p}},\hat{\mathbf{p}}') = 0, \tag{A.7e}$$

$$\omega_{23}(\hat{\mathbf{p}},\hat{\mathbf{p}}') = \omega_{32}(\hat{\mathbf{p}},\hat{\mathbf{p}}') = 0, \tag{A.7f}$$

$$\omega_{33}(\hat{\mathbf{p}},\hat{\mathbf{p}}') = 1. \tag{A.7g}$$

Finally, in the *CSL* phase, the corresponding functions are

$$\omega_{11}(\hat{\mathbf{p}},\hat{\mathbf{p}}') = 1+\frac{1}{4}(1+\hat{\mathbf{p}}\cdot\hat{\mathbf{p}}')^2, \tag{A.8}$$

$$\omega_{12}(\hat{\mathbf{p}},\hat{\mathbf{p}}') = \omega_{21}(\hat{\mathbf{p}},\hat{\mathbf{p}}') = 1-\frac{1}{4}(1+\hat{\mathbf{p}}\cdot\hat{\mathbf{p}}')^2, \tag{A.9}$$

$$\omega_{22}(\hat{\mathbf{p}},\hat{\mathbf{p}}') = \frac{1}{4}(1+\hat{\mathbf{p}}\cdot\hat{\mathbf{p}}')^2. \tag{A.10}$$

A.2   Angular integrations in CSL phase

In the calculation of the λ-rate in the CSL phase, there are four different types of angular integrations over the phase space of quark momenta. Thus, the results for the

$F_{r_1 r_2 r_3 r_4}$ functions, formally defined by Eq. (2.27) in the main text, have the following general structure:

$$F_{1111} = K_0 + K_1 + K_2 + K_3 , \tag{A.11a}$$

$$F_{1112} = K_0 - K_1 + K_2 - K_3 , \tag{A.11b}$$

$$F_{1121} = K_0 + K_1 - K_2 - K_3 , \tag{A.11c}$$

$$F_{1122} = K_0 - K_1 - K_2 + K_3 , \tag{A.11d}$$

$$F_{1211} = K_0 + K_1 - K_2 - K_3 , \tag{A.11e}$$

$$F_{1212} = K_0 - K_1 - K_2 + K_3 , \tag{A.11f}$$

$$F_{1221} = K_2 + K_3 , \tag{A.11g}$$

$$F_{1222} = K_2 - K_3 , \tag{A.11h}$$

$$F_{2111} = K_0 - K_1 + K_2 - K_3 , \tag{A.11i}$$

$$F_{2112} = K_1 + K_3 , \tag{A.11j}$$

$$F_{2121} = K_0 - K_1 - K_2 + K_3 , \tag{A.11k}$$

$$F_{2122} = K_1 - K_3 , \tag{A.11l}$$

$$F_{2211} = K_0 - K_1 - K_2 + K_3 , \tag{A.11m}$$

$$F_{2212} = K_1 - K_3 , \tag{A.11n}$$

$$F_{2221} = K_2 - K_3 , \tag{A.11o}$$

$$F_{2222} = K_3 , \tag{A.11p}$$

where the four types of angular integrals are given by:

$$
\begin{aligned}
K_0 &= \int d\Omega_1 \int d\Omega_2 \int d\Omega_3 \int d\Omega_4 (1 - \hat{\mathbf{p}}_1 \cdot \hat{\mathbf{p}}_2)(1 - \hat{\mathbf{p}}_3 \cdot \hat{\mathbf{p}}_4) \\
&\times \ \delta(\mathbf{p}_1 + \mathbf{p}_2 - \mathbf{p}_3 - \mathbf{p}_4),
\end{aligned}
\tag{A.12}
$$

$$
\begin{aligned}
K_1 &= \frac{1}{4} \int d\Omega_1 \int d\Omega_2 \int d\Omega_3 \int d\Omega_4 (1 - \hat{\mathbf{p}}_1 \cdot \hat{\mathbf{p}}_2)(1 - \hat{\mathbf{p}}_3 \cdot \hat{\mathbf{p}}_4)(1 + \hat{\mathbf{p}}_4 \cdot \hat{\mathbf{p}}_1)^2 \\
&\times \ \delta(\mathbf{p}_1 + \mathbf{p}_2 - \mathbf{p}_3 - \mathbf{p}_4),
\end{aligned}
\tag{A.13}
$$

$$
\begin{aligned}
K_2 &= \frac{1}{4} \int d\Omega_1 \int d\Omega_2 \int d\Omega_3 \int d\Omega_4 (1 - \hat{\mathbf{p}}_1 \cdot \hat{\mathbf{p}}_2)(1 - \hat{\mathbf{p}}_3 \cdot \hat{\mathbf{p}}_4)(1 + \hat{\mathbf{p}}_3 \cdot \hat{\mathbf{p}}_2)^2 \\
&\times \ \delta(\mathbf{p}_1 + \mathbf{p}_2 - \mathbf{p}_3 - \mathbf{p}_4),
\end{aligned}
$$

$$
\begin{aligned}
K_3 &= \frac{1}{16} \int d\Omega_1 \int d\Omega_2 \int d\Omega_3 \int d\Omega_4 (1 - \hat{\mathbf{p}}_1 \cdot \hat{\mathbf{p}}_2)(1 - \hat{\mathbf{p}}_3 \cdot \hat{\mathbf{p}}_4)(1 + \hat{\mathbf{p}}_4 \cdot \hat{\mathbf{p}}_1)^2 \\
&\times \ (1 + \hat{\mathbf{p}}_3 \cdot \hat{\mathbf{p}}_2)^2 \delta(\mathbf{p}_1 + \mathbf{p}_2 - \mathbf{p}_3 - \mathbf{p}_4).
\end{aligned}
\tag{A.14}
$$

The result for K_0 was obtained in Ref. [101]. It reads

$$
K_0 = \frac{4\pi^3}{p_1^2 p_2^2 p_3^2 p_4^2} L_0(p_{12}, P_{12}, p_{34}, P_{34}),
\tag{A.15}
$$

where $p_{ij} \equiv |p_i - p_j|$, $P_{ij} \equiv p_i + p_j$, and

$$
\begin{aligned}
L_0(a,b,c,d) &\equiv \Theta(c-a)\Theta(d-b)\Theta(b-c)J_0(c,b,b,d) \\
&+ \Theta(a-c)\Theta(b-d)\Theta(d-a)J_0(a,d,b,d) \\
&+ \Theta(a-c)\Theta(d-b)J_0(a,b,b,d) + \Theta(c-a)\Theta(b-d)J_0(c,d,b,d)
\end{aligned}
\tag{A.16}
$$

which is given in terms of

$$
\begin{aligned}
J_0(a,b,c,d) &\equiv \int_a^b dP\,(c^2 - P^2)(d^2 - P^2) \\
&= c^2 d^2 (b-a) - \frac{1}{3}(c^2 + d^2)(b^3 - a^3) + \frac{1}{5}(b^5 - a^5).
\end{aligned}
\tag{A.17}
$$

To leading order in powers of large μ, this result simplifies to

$$
L_0(0, 2\mu, 0, 2\mu) = \frac{2^8 \mu^5}{15}.
\tag{A.18}
$$

105

By making use of Eq. (A.15), therefore, we obtain

$$K_0 \simeq \frac{4\pi^3}{\mu^8} L_0(0, 2\mu, 0, 2\mu) = \frac{2^{10}\pi^3}{15\mu^3}. \tag{A.19}$$

Using the same approach, in the following subsections we calculate the results for K_1, K_2, and K_3.

A.2.1 Calculation of K_1

Here we calculate the angular integral K_1. Following the approach of Ref. [101], we obtain

$$
\begin{aligned}
K_1 &= \frac{1}{4} \int d\Omega_1 \int d\Omega_2 \int d\Omega_3 \int d\Omega_4 (1 - \hat{\mathbf{p}}_1 \cdot \hat{\mathbf{p}}_2)(1 - \hat{\mathbf{p}}_3 \cdot \hat{\mathbf{p}}_4)(1 + \hat{\mathbf{p}}_4 \cdot \hat{\mathbf{p}}_1)^2 \\
&\quad \times \ \delta(\mathbf{p}_1 + \mathbf{p}_2 - \mathbf{p}_3 - \mathbf{p}_4) \\
&= \frac{1}{4p_2^2} \int d\Omega_1 \int d\Omega_3 \int d\Omega_4 \left[1 - \frac{1}{p_2}(\hat{\mathbf{p}}_1 \cdot \mathbf{P} - p_1) \right] (1 - \hat{\mathbf{p}}_3 \cdot \hat{\mathbf{p}}_4)(1 + \hat{\mathbf{p}}_4 \cdot \hat{\mathbf{p}}_1)^2 \\
&\quad \times \ \delta(p_2 - |\mathbf{P} - \mathbf{p_1}|) \\
&= \frac{1}{4p_2^2} \int d\Omega_3 \int d\Omega_4 \int_0^{2\pi} d\phi_1 \int_0^{\pi} d\theta_1 \sin\theta_1 \left[1 - \frac{1}{p_2}(P\cos\theta_1 - p_1) \right] \\
&\quad \times \ (1 - \hat{\mathbf{p}}_3 \cdot \hat{\mathbf{p}}_4)\delta(p_2 - |\mathbf{P} - \mathbf{p_1}|) \left[1 + \cos\theta_1\cos\theta_4 + \sin\theta_1\sin\theta_4\cos(\phi_1 - \phi_4) \right]^2,
\end{aligned}
\tag{A.20}
$$

where $\mathbf{P} = \mathbf{p_3} + \mathbf{p_4}$ and $P = |\mathbf{P}|$. In order to integrate over θ_1, we choose the coordinate system so that the z-axis is along the vector $\mathbf{P}$. After making use of the δ-function, we easily integrate over θ_1 and arrive at the following result:

$$
\begin{aligned}
K_1 &= \int d\Omega_3 \int d\Omega_4 \frac{P_{12}^2 - P^2}{8Pp_1^2 p_2^2}(1 - \hat{\mathbf{p}}_3 \cdot \hat{\mathbf{p}}_4)\Theta(P_{12} - P)\Theta(P - p_{12}) \\
&\quad \times \int_0^{2\pi} d\phi_1 [1 + \cos\theta_1^*\cos\theta_4 + \sin\theta_1^*\sin\theta_4\cos(\phi_1 - \phi_4)]^2 \\
&= \pi \int d\Omega_3 \int d\Omega_4 \frac{P_{12}^2 - P^2}{8Pp_1^2 p_2^2}\Theta(P_{12} - P)\Theta(P - p_{12})(1 - \hat{\mathbf{p}}_3 \cdot \hat{\mathbf{p}}_4) \\
&\quad \times \left[2(1 + \cos\theta_1^*\cos\theta_4)^2 + (\sin\theta_1^*\sin\theta_4)^2 \right], \tag{A.21}
\end{aligned}
$$

where $\cos\theta_1^* = (P^2 + p_1^2 - p_2^2)/2Pp_1$ and $\cos\theta_4 = (\hat{\mathbf{p}}_4 \cdot \hat{\mathbf{P}}) = (P^2 + p_4^2 - p_3^2)/2Pp_4$. It may be appropriate to emphasize that the result of the last integration was presented in

106

a form that independent of a specific choice of the coordinate system. As can be easily checked, the integrand in Eq. (A.21) depends only on the relative angle θ_{34} between the vectors $\hat{\mathbf{p}}_3$ and $\hat{\mathbf{p}}_4$ (or equivalently only on the variable P). Therefore, while integrating over Ω_4, we could fix the orientation of $\hat{\mathbf{p}}_3$ arbitrarily. It is convenient to choose $\hat{\mathbf{p}}_3$ as the z-axis and perform the integration over Ω_4. The result is independent of the angular coordinates in Ω_3. Thus, the remaining integration over Ω_3 gives an extra factor 4π. In the end, we arrive at

$$K_1 \;=\; \frac{\pi^3}{2p_1^2 p_2^2 p_3^2 p_4^2} \int_{P_{34}}^{P_{34}} g(P) dP, \tag{A.22}$$

where

$$
\begin{aligned}
g(P) \;=\; & (P_{12}^2 - P^2)(P_{34}^2 - P^2)\Theta(P_{12} - P)\Theta(P - p_{12}) \\
\times\; & \left[2\left(1 + \frac{(P^2 + p_1^2 - p_2^2)(P^2 + p_4^2 - p_3^2)}{4P^2 p_1 p_4}\right)^2 + \left(1 - \frac{(P^2 + p_1^2 - p_2^2)^2}{4P^2 p_1^2}\right) \right. \\
\times\; & \left. \left(1 - \frac{(P^2 + p_4^2 - p_3^2)^2}{4P^2 p_4^2}\right) \right].
\end{aligned}
\tag{A.23}
$$

Note that we changed the integration variable from θ_{34} to $P = \sqrt{p_3^2 + p_4^2 + 2p_3 p_4 \cos\theta_{34}}$.

The final result for K_1 can be conveniently given in the same form as K_0 in the previous section, i.e.,

$$K_1 = \frac{\pi^3}{2p_1^2 p_2^2 p_3^2 p_4^2} L_1(p_{12}, P_{12}, p_{34}, P_{34}), \tag{A.24}$$

where, by definition,

$$
\begin{aligned}
L_1(a,b,c,d) \;\equiv\; & \Theta(c-a)\Theta(d-b)\Theta(b-c)J_1(c,b,b,d) \\
+\; & \Theta(a-c)\Theta(b-d)\Theta(d-a)J_1(a,d,b,d) \\
+\; & \Theta(a-c)\Theta(d-b)J_1(a,b,b,d) + \Theta(c-a)\Theta(b-d)J_1(c,d,b,d),
\end{aligned}
\tag{A.25}
$$

and

$$J_1(a,b,c,d) = \int_a^b dP(c^2 - P^2)(d^2 - P^2)\left[2\left(1 + \frac{(P^2 + p_1^2 - p_2^2)(P^2 + p_4^2 - p_3^2)}{4P^2 p_1 p_4}\right)^2\right.$$
$$\left. + \left(1 - \frac{(P^2 + p_1^2 - p_2^2)^2}{4P^2 p_1^2}\right)\left(1 - \frac{(P^2 + p_4^2 - p_3^2)^2}{4P^2 p_4^2}\right)\right]. \tag{A.26}$$

To leading order in powers of large μ, this result reduces to

$$L_1(0, 2\mu, 0, 2\mu) = \frac{2^{11}\mu^5}{35}. \tag{A.27}$$

This, in turn, gives

$$K_1 \simeq \frac{\pi^3}{2\mu^8} L_1(0, 2\mu, 0, 2\mu) = \frac{2^{10}\pi^3}{35\mu^3}. \tag{A.28}$$

A.2.2 Calculation of K_2

As is easy to see, the expression for K_2 can be obtained from K_1 by the following exchange of variables: $p_1 \leftrightarrow p_2$ and $p_3 \leftrightarrow p_4$. Thus, the result reads

$$K_2 = \frac{\pi^3}{2p_1^2 p_2^2 p_3^2 p_4^2} L_2(p_{12}, P_{12}, p_{34}, P_{34}), \tag{A.29}$$

where

$$L_2(a,b,c,d) \equiv \Theta(c-a)\Theta(d-b)\Theta(b-c)J_2(c,b,b,d)$$
$$+ \Theta(a-c)\Theta(b-d)\Theta(d-a)J_2(a,d,b,d)$$
$$+ \Theta(c-a)\Theta(b-d)J_2(c,d,b,d) + \Theta(a-c)\Theta(d-b)J_2(a,b,b,d),$$
$$\tag{A.30}$$

and

$$J_2(a,b,c,d) = \int_a^b dP(c^2 - P^2)(d^2 - P^2)\left[2\left(1 + \frac{(P^2 + p_2^2 - p_1^2)(P^2 + p_3^2 - p_4^2)}{4P^2 p_2 p_3}\right)^2\right.$$
$$\left. + \left(1 - \frac{(P^2 + p_2^2 - p_1^2)^2}{4P^2 p_2^2}\right)\left(1 - \frac{(P^2 + p_3^2 - p_4^2)^2}{4P^2 p_3^2}\right)\right]. \tag{A.31}$$

We also find that K_2 is identical to K_1 to leading order in powers of large μ, i.e.,

$$K_2 \simeq \frac{2^{10}\pi^3}{35\mu^3}. \tag{A.32}$$

A.2.3   Calculation of K_3

Now we calculate the angular integral K_3. We start by using the same approach as in the calculation of K_1,

$$
\begin{aligned}
K_3 &= \frac{1}{16p_2^2} \int d\Omega_1 \int d\Omega_3 \int d\Omega_4 \left[1 - \frac{1}{p_2}(\hat{\mathbf{p}}_1 \cdot \mathbf{P} - p_1) \right] (1 - \hat{\mathbf{p}}_3 \cdot \hat{\mathbf{p}}_4)(1 + \hat{\mathbf{p}}_4 \cdot \hat{\mathbf{p}}_1)^2 \\
&\times \left[1 + \frac{1}{p_2 p_3}(\mathbf{p}_3 \cdot \mathbf{P} - \mathbf{p}_1 \cdot \mathbf{P} + \mathbf{p}_1 \cdot \mathbf{p}_4) \right]^2 \delta(p_2 - |\mathbf{P} - \mathbf{p_1}|).
\end{aligned} \tag{A.33}
$$

To calculate the integral over Ω_1, we fix the coordinate system so that the z-axis coincides with the direction of $\mathbf{P}$. After integration, we obtain

$$
\begin{aligned}
K_3 &= \int d\Omega_3 \int d\Omega_4 \frac{P_{12}^2 - P^2}{32 P p_1^2 p_2^2} \Theta(P_{12} - P)\Theta(P - p_{12})(1 - \hat{\mathbf{p}}_3 \cdot \hat{\mathbf{p}}_4) \\
&\times \int_0^{2\pi} d\phi_1 [1 + \cos\theta_1^* \cos\theta_4 + \sin\theta_1^* \sin\theta_4 \cos(\phi_1 - \phi_4)]^2 \\
&\times \left[1 + \frac{p_2^2 - p_1^2 + p_3^2 - p_4^2}{2 p_2 p_3} + \frac{p_1 p_4}{p_2 p_3}(\cos\theta_1^* \cos\theta_4 + \sin\theta_1^* \sin\theta_4 \cos(\phi_1 - \phi_4)) \right]^2,
\end{aligned} \tag{A.34}
$$

where $\cos\theta_1^* = (P^2 + p_1^2 - p_2^2)/2Pp_1$ and $\cos\theta_4 = (\hat{\mathbf{p}}_4 \cdot \hat{\mathbf{P}}) = (P^2 + p_4^2 - p_3^2)/2Pp_4$. In the derivation, we also used the following relation:

$$
\mathbf{p}_3 \cdot \mathbf{P} = \frac{P^2 + p_3^2 - p_4^2}{2}. \tag{A.35}
$$

By performing the integration over ϕ_1, we derive

$$
K_3 = \pi \int d\Omega_3 \int d\Omega_4 \frac{(P_{12}^2 - P^2)(P_{34}^2 - P^2)}{256 P p_1^2 p_2^2 p_3^3 p_4^3} \Theta(P_{12} - P)\Theta(P - p_{12}) \Bigg\{ \left(P_{14}^2 - P_{23}^2\right)^2
$$

$$
\times \left[2\left(1 + \frac{(P^2 + p_1^2 - p_2^2)(P^2 + p_4^2 - p_3^2)}{4P^2 p_1 p_4}\right)^2 + \left(1 - \frac{(P^2 + p_1^2 - p_2^2)^2}{4P^2 p_1^2}\right) \right.
$$

$$
\times \left. \left(1 - \frac{(P^2 + p_4^2 - p_3^2)^2}{4P^2 p_4^2}\right) \right] - 4 p_1 p_4 \left(P_{14}^2 - P_{23}^2\right)\left(1 + \frac{(P^2 + p_1^2 - p_2^2)(P^2 + p_4^2 - p_3^2)}{4P^2 p_1 p_4}\right)
$$

$$
\times \left[2\left(1 + \frac{(P^2 + p_1^2 - p_2^2)(P^2 + p_4^2 - p_3^2)}{4P^2 p_1 p_4}\right)^2 + 3\left(1 - \frac{(P^2 + p_1^2 - p_2^2)^2}{4P^2 p_1^2}\right) \right.
$$

$$
\left. \left(1 - \frac{(P^2 + p_4^2 - p_3^2)^2}{4P^2 p_4^2}\right) \right] + p_1^2 p_4^2 \left[8\left(1 + \frac{(P^2 + p_1^2 - p_2^2)(P^2 + p_4^2 - p_3^2)}{4P^2 p_1 p_4}\right)^4 \right.
$$

$$
+ \; 3\left(1 - \frac{(P^2 + p_1^2 - p_2^2)^2}{4P^2 p_1^2}\right)^2 \left(1 - \frac{(P^2 + p_4^2 - p_3^2)^2}{4P^2 p_4^2}\right)^2 + 24\left(1 - \frac{(P^2 + p_1^2 - p_2^2)^2}{4P^2 p_1^2}\right)
$$

$$
\times \; \left(1 + \frac{(P^2 + p_1^2 - p_2^2)(P^2 + p_4^2 - p_3^2)}{4P^2 p_1 p_4}\right)^2 \left(1 - \frac{(P^2 + p_4^2 - p_3^2)^2}{4P^2 p_4^2}\right) \Bigg] \Bigg\},
$$

$$
\text{(A.36)}
$$

Finally, in order to integrating over Ω_4, we use the coordinate system with the z-axis along $\hat{\mathbf{p}}_3$. Then, we get

$$
K_3 = \frac{\pi^3}{32 p_1^2 p_2^2 p_3^4 p_4^4} \int_{p_{34}}^{P_{34}} h(P) dP,
\tag{A.37}
$$

where

$$
\begin{aligned}
h(P) \;=\;& (P_{12}^2 - P^2)(P_{34}^2 - P^2)\Theta(P_{12} - P)\Theta(P - p_{12}) \\
&\times\; \left\{ (P_{14}^2 - P_{23}^2)^2 \left[2\left(1 + \frac{(P^2 + p_1^2 - p_2^2)(P^2 + p_4^2 - p_3^2)}{4P^2 p_1 p_4}\right)^2 \right.\right. \\
&\;+\; \left.\left(1 - \frac{(P^2 + p_1^2 - p_2^2)^2}{4P^2 p_1^2}\right)\left(1 - \frac{(P^2 + p_4^2 - p_3^2)^2}{4P^2 p_4^2}\right)\right] \\
&\;-\; 4 p_1 p_4 \left(P_{14}^2 - P_{23}^2\right)\left(1 + \frac{(P^2 + p_1^2 - p_2^2)(P^2 + p_4^2 - p_3^2)}{4P^2 p_1 p_4}\right) \\
&\times\; \left[2\left(1 + \frac{(P^2 + p_1^2 - p_2^2)(P^2 + p_4^2 - p_3^2)}{4P^2 p_1 p_4}\right)^2 \right. \\
&\;+\; \left. 3\left(1 - \frac{(P^2 + p_1^2 - p_2^2)^2}{4P^2 p_1^2}\right)\left(1 - \frac{(P^2 + p_4^2 - p_3^2)^2}{4P^2 p_4^2}\right)\right] \\
&\;+\; p_1^2 p_4^2 \left[8\left(1 + \frac{(P^2 + p_1^2 - p_2^2)(P^2 + p_4^2 - p_3^2)}{4P^2 p_1 p_4}\right)^4 \right. \\
&\;+\; 3\left(1 - \frac{(P^2 + p_1^2 - p_2^2)^2}{4P^2 p_1^2}\right)^2\left(1 - \frac{(P^2 + p_4^2 - p_3^2)^2}{4P^2 p_4^2}\right)^2 \\
&\;+ 24\left(1 + \frac{(P^2 + p_1^2 - p_2^2)(P^2 + p_4^2 - p_3^2)}{4P^2 p_1 p_4}\right)^2 \\
&\times\; \left.\left.\left(1 - \frac{(P^2 + p_1^2 - p_2^2)^2}{4P^2 p_1^2}\right)\left(1 - \frac{(P^2 + p_4^2 - p_3^2)^2}{4P^2 p_4^2}\right)\right] \right\}.
\end{aligned} \tag{A.38}
$$

The result can be given in the same form as the other integrals in the previous subsections, i.e.,

$$
K_3 = \frac{\pi^3}{32\, p_1^2 p_2^2 p_3^4 p_4^4}\, L_3(p_{12}, P_{12}, p_{34}, P_{34}), \tag{A.39}
$$

where

$$
\begin{aligned}
L_3(a,b,c,d) \;\equiv\;& \Theta(c - a)\Theta(d - b)\Theta(b - c)J_3(c,b,b,d) \\
&+\; \Theta(a - c)\Theta(d - b)J_3(a,b,b,d) \\
&+\; \Theta(a - c)\Theta(b - d)\Theta(d - a)J_3(a,d,b,d) \\
&+\; \Theta(c - a)\Theta(b - d)J_3(c,d,b,d), \tag{A.40}
\end{aligned}
$$

and

$$J_3(a,b,c,d) = \int_a^b dP\,(c^2 - P^2)(d^2 - P^2)\left\{ (P_{14}^2 - P_{23}^2)^2 \right.$$

$$\times\ \left[2\left(1 + \frac{(P^2 + p_1^2 - p_2^2)(P^2 + p_4^2 - p_3^2)}{4P^2 p_1 p_4}\right)^2 + \left(1 - \frac{(P^2 + p_1^2 - p_2^2)^2}{4P^2 p_1^2}\right) \right.$$

$$\times\ \left.\left(1 - \frac{(P^2 + p_4^2 - p_3^2)^2}{4P^2 p_4^2}\right) \right] - (P_{14}^2 - P_{23}^2)\left(1 + \frac{(P^2 + p_1^2 - p_2^2)(P^2 + p_4^2 - p_3^2)}{4P^2 p_1 p_4}\right)$$

$$\times\ 4p_1 p_4\left[2\left(1 + \frac{(P^2 + p_1^2 - p_2^2)(P^2 + p_4^2 - p_3^2)}{4P^2 p_1 p_4}\right)^2 + 3\left(1 - \frac{(P^2 + p_1^2 - p_2^2)^2}{4P^2 p_1^2}\right) \right.$$

$$\times\ \left.\left(1 - \frac{(P^2 + p_4^2 - p_3^2)^2}{4P^2 p_4^2}\right) \right] + p_1^2 p_4^2\left[8\left(1 + \frac{(P^2 + p_1^2 - p_2^2)(P^2 + p_4^2 - p_3^2)}{4P^2 p_1 p_4}\right)^4 \right.$$

$$+\ 3\left(1 - \frac{(P^2 + p_1^2 - p_2^2)^2}{4P^2 p_1^2}\right)^2\left(1 - \frac{(P^2 + p_4^2 - p_3^2)^2}{4P^2 p_4^2}\right)^2$$

$$+\ 24\left(1 + \frac{(P^2 + p_1^2 - p_2^2)(P^2 + p_4^2 - p_3^2)}{4P^2 p_1 p_4}\right)^2$$

$$\times\ \left.\left.\left(1 - \frac{(P^2 + p_1^2 - p_2^2)^2}{4P^2 p_1^2}\right)\left(1 - \frac{(P^2 + p_4^2 - p_3^2)^2}{4P^2 p_4^2}\right) \right] \right\}. \tag{A.41}$$

To leading order in powers of large μ, the result reduces to

$$L_3(0, 2\mu, 0, 2\mu) = \frac{29 \times 2^{20}\mu^9}{45045}. \tag{A.42}$$

Then, by making use of the relation in Eq. (A.39), we derive

$$K_3 \simeq \frac{\pi^3}{2\mu^{12}} L_3(0, 2\mu, 0, 2\mu) = \frac{29 \times 2^{15}\pi^3}{45045\mu^3}. \tag{A.43}$$

A.2.4 $F_{r_1 r_2 r_3 r_4}$ to leading order in inverse powers of μ

By making use of the leading order results for K_i ($i = 1, 2, 3$) obtained in the previous subsections, here we write down the explicit results for the functions $F_{r_1 r_2 r_3 r_4}$ in the same approximation:

$$F_{1111} = \frac{1301 \times 2^{10}\pi^3}{9009\mu^3}, \tag{A.44a}$$

$$F_{1221} = F_{2112} = \frac{443 \times 2^{10}\pi^3}{9009\mu^3}, \tag{A.44b}$$

$$F_{1112} = F_{1121} = F_{1211} = F_{2111} = \frac{415 \times 2^{10}\pi^3}{9009\mu^3}, \tag{A.44c}$$

$$F_{1122} = F_{1212} = F_{2121} = F_{2211} = \frac{1357 \times 2^{10}\pi^3}{45045\mu^3}, \tag{A.44d}$$

$$F_{1222} = F_{2122} = F_{2212} = F_{2221} = \frac{359 \times 2^{10}\pi^3}{45045\mu^3}, \tag{A.44e}$$

$$F_{2222} = \frac{29 \times 2^{15}\pi^3}{45045\mu^3}. \tag{A.44f}$$

Note that

$$\sum_{r_1,r_2,r_3,r_4} F_{r_1 r_2 r_3 r_4} = \frac{3 \times 2^{10}\pi^3}{5\mu^3}. \tag{A.45}$$

APPENDIX B

λ-RATES OF WEAK PROCESSES

B.1 λ-rates of semi-leptonic (Urca) processes

The rates of the semi-leptonic processes in spin-one color superconducting quark matter were calculated in Ref. [65]. The general expression for the rate takes the following form:

$$\lambda_i = \lambda_i^{(0)} \left[\frac{1}{3} + \frac{2}{3} H \left(\frac{\phi}{T} \right) \right] \quad \text{for} \quad i = 2, 3, \tag{B.1}$$

where $\lambda_i^{(0)}$ is the corresponding rate in the normal phase of quark matter and $H(\phi/T)$ is a phase-specific suppression factor. By construction, it satisfies the constraint $H(0) = 1$, which corresponds to the case of the normal phase. We used the numerical data of Ref. [65] to obtain the following fits for the suppression factors as functions of the dimensionless ratio $\varphi \equiv \phi/T$ in the four spin-one color superconducting phases of quark matter:

$$H^A (\varphi) = \frac{a_1 \varphi^4 + b_1 \varphi^3 + c_1 \varphi^2 + d_1}{\varphi^5 + e_1 \varphi^3 + f_1 \varphi^2 + d_1}, \tag{B.2}$$

where $a_1 = 1.069$, $b_1 = -0.2187$, $c_1 = 3.666$, $d_1 = 21.50$, $e_1 = 1.333$ and $f_1 = 9.349$,

$$H^{\text{polar}} (\varphi) = \frac{a_2 \varphi^3 + b_2 \varphi^2 + c_2}{\varphi^5 + d_2 \varphi^4 + e_2 \varphi^3 + f_2 \varphi^2 + c_2}, \tag{B.3}$$

where $a_2 = \pi$, $b_2 = 21.94$, $c_2 = 1386$, $d_2 = 6.994$, $e_2 = 11.20$ and $f_2 = 214.0$,

$$H^{\text{planar}} (\varphi) = \frac{a_3 \varphi^{3.5} + b_3 \varphi^3 + c_3 \varphi^2 + d_3 (1 + \varphi)}{\varphi^3 + e_3 \varphi^2 + d_3} e^{-\varphi}, \tag{B.4}$$

where $a_3 = 0.917$, $b_3 = 0.456$, $c_3 = 11.69$, $d_3 = 34.0$ and $e_3 = 4.221$,

$$H^{\text{CSL}} (\varphi) = \frac{a_4 \varphi^4 + b_4 \varphi^3 + c_4 \varphi^2 + d_4 (1 + \sqrt{2}\varphi)}{\varphi^3 + e_4 \varphi^2 + d_4} e^{-\sqrt{2}\varphi}, \tag{B.5}$$

where $a_4 = 1.034$, $b_4 = 1.001$, $c_4 = 9.735$, $d_4 = 13.81$ and $e_4 = 1.684$.

B.2 λ-rates of nonleptonic processes

The λ-rate of the nonleptonic processes in spin-one color superconducting quark matter was calculated in Ref. [106]. The general expression for the rate takes the following

form:

$$\lambda_1 = \lambda_1^{(0)} \left[\mathcal{N} + (1 - \mathcal{N})\tilde{H}\left(\frac{\phi}{T}\right) \right], \tag{B.6}$$

where $\lambda_1^{(0)}$ is the corresponding rate in the normal phase of quark matter, $\mathcal{N}$ is a constant that determines the relative contribution of ungapped quasiparticles to the rate, and $\tilde{H}(\phi/T)$ is a phase-specific suppression factor due to gapped quasiparticles. The normal phase corresponds to $\phi = 0$, in which case there is no suppression and $\tilde{H}(0) = 1$. The value of $\mathcal{N}$ for each phase reads

$$\mathcal{N}^A = \frac{1}{9}, \tag{B.7a}$$

$$\mathcal{N}^{\text{polar}} = \frac{1}{9}, \tag{B.7b}$$

$$\mathcal{N}^{\text{planar}} \approx 0.0393, \tag{B.7c}$$

$$\mathcal{N}^{\text{CSL}} = \frac{928}{27027}. \tag{B.7d}$$

For this study we used the numerical data of Ref. [106] to obtain the following fits for the suppression factors as functions of the dimensionless ratio $\varphi \equiv \phi/T$:

$$\tilde{H}^A(\varphi) = \frac{\alpha_1 \varphi^2 + \beta_1}{\varphi^3 + \gamma_1 \varphi^2 + \beta_1}, \tag{B.8}$$

where $\alpha_1 = 0.1247$, $\beta_1 = 12.60$ and $\gamma_1 = 5.042$,

$$\tilde{H}^{\text{polar}}(\varphi) = \frac{\alpha_2 \varphi^2 + \beta_2}{\varphi^4 + \gamma_2 \varphi^2 + \beta_2}, \tag{B.9}$$

where $\alpha_2 = 0.0271$, $\beta_2 = 65.45$ and $\gamma_2 = 13.35$,

$$\tilde{H}^{\text{planar}}(\varphi) = \frac{\alpha_3 \varphi^4 + \beta_3 \varphi^3 + \gamma_3 \varphi^2 + \delta_3(1 + \varphi)}{\varphi^2 + \delta_3} e^{-\varphi}, \tag{B.10}$$

where $\alpha_3 = 0.0717$, $\beta_3 = -0.2663$, $\gamma_3 = 1.108$ and $\delta_3 = 4.561$,

$$\tilde{H}^{\text{CSL}}(\varphi) = \frac{\alpha_4 \varphi^4 + \beta_4 \varphi^2 + \gamma_4(1 + \sqrt{2}\varphi)}{\varphi^3 + \delta_4 \varphi^2 + \gamma_4} e^{-\sqrt{2}\varphi}, \tag{B.11}$$

where $\alpha_4 = 0.6981$, $\beta_4 = -2.045$, $\gamma_4 = 4.482$ and $\delta_4 = -1.217$.

APPENDIX C

ANHARMONIC OSCILLATOR

C.1 Anharmonic oscillator with a cubic potential (Type I)

The anharmonic oscillator with cubic potential $U(x) = m\omega_0^2 \left(\frac{x^2}{2} + \alpha \frac{x^3}{3} \right)$ is described by the following equation of motion:

$$\ddot{x} + \omega_0^2 x (1 + \alpha x) = 0. \tag{C.1}$$

By making use of the known parametric solution to the above differential equation [143] and assuming that $x_0 > 0$ is the maximum deviation from the equilibrium point $x = 0$ in the positive x-direction, we find that the periodic solution exists for $-1 < \alpha x_0 < 1/2$. (The apparent asymmetry between positive and negative values of αx_0 is a result of the assumption that x_0 is the maximum deviation from the equilibrium point in the *positive* x-direction.) It is given in terms of the Jacobi elliptic function $\mathrm{sn}\,(u|m)$ as follows:

$$x(t) = x_0 \left[1 - \frac{3a_-}{2\alpha^*} \mathrm{sn} \left(\frac{(t-t_0)\omega_0\sqrt{a_+}}{2} \bigg| \frac{a_-}{a_+} \right)^2 \right], \tag{C.2}$$

where $a_\pm = \frac{1}{2} \left(1 + 2\alpha^* \pm \sqrt{(1 + \frac{2}{3}\alpha^*)(1 - 2\alpha^*)} \right)$ and $\alpha^* \equiv \alpha x_0$ is a dimensionless parameter that measures the maximum deviation of the solution from the harmonic regime. Note that $x(t)$ is periodic with the period given by

$$
\begin{aligned}
\tau_\alpha &= \frac{4}{\omega_0\sqrt{a_+}} K \left(\frac{a_-}{a_+} \right) \\
&\simeq \frac{2\pi}{\omega_0} \left(1 + \frac{5}{12}(\alpha x_0)^2 + \frac{5}{18}(\alpha x_0)^3 + O\left[(\alpha x_0)^4\right] \right), \quad \text{for } \alpha x_0 \to 0, \quad \text{(C.3)}
\end{aligned}
$$

where $K\,(a_-/a_+)$ is the complete elliptic integral of the first kind. Two representative solutions are shown in Fig. C.1. For anharmonic solutions of this type, the average kinetic energy is given by

$$\langle E_{\mathrm{kin}} \rangle = \frac{1}{\tau_\alpha} \int_0^{\tau_\alpha} \frac{m\dot{x}^2}{2} dt = \frac{m\omega_0^2 x_0^2}{4} \mathscr{F}, \tag{C.4}$$
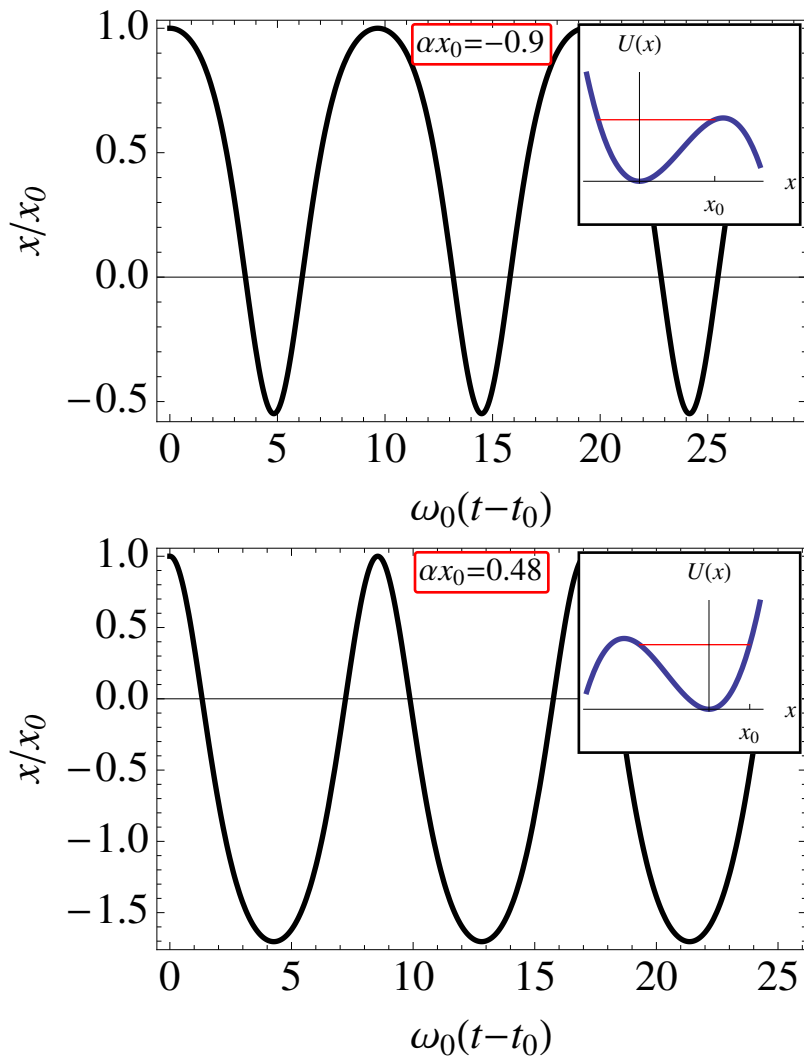
118

Figure C.1: Solutions to the equation of motion of the anharmonic oscillator with a cubic potential for two values of the coupling constant. The inserts show the corresponding shapes of the potentials.

where the analytical expression for constant $\mathscr{F}$ reads

$$\mathscr{F} = \frac{4(1+\alpha^*)}{5\alpha^* a_-} \left\{ \frac{E\left(\frac{a_-}{a_+}\right)}{K\left(\frac{a_-}{a_+}\right)} - (a_+ - a_-)\left(a_+ - \frac{1}{2}a_-\right) \right\}. \qquad \text{(C.5)}$$

Here $E\left(a_-/a_+\right)$ is the complete elliptic integral of the second kind.

C.2   Anharmonic oscillator with a quartic potential (Type II)

The anharmonic oscillator with quartic potential $U(x) = m\omega_0^2 \left(\frac{x^2}{2} + \beta\frac{x^4}{4}\right)$ is described by the following equation of motion:

$$\ddot{x} + \omega_0^2 x\left(1 + \beta x^2\right) = 0, \qquad \text{(Type II)}. \qquad \text{(C.6)}$$

Using the known parametric solution to the above differential equation [143] and assuming that x_0 is the maximum deviation from the equilibrium point $x = 0$, we find that the periodic solution exists for $\beta^* \equiv \beta x_0^2 > -1$. The solution is given in terms of the Jacobi elliptic function,

$$x(t) \;=\; x_0 \frac{\sqrt{1+(1/2)\beta^*}}{\sqrt{1+\beta^*}}\,\mathrm{sd}\left(\omega_0(t-t_0)\sqrt{1+\beta^*}\,\Big|\,\frac{\beta^*}{2(1+\beta^*)}\right). \qquad \text{(C.7)}$$

This is a periodic solution with the period equal

$$\begin{aligned} \tau_\beta \;&=\; \frac{4}{\omega_0\sqrt{1+\beta^*}}K\left(\frac{\beta^*}{2(1+\beta^*)}\right) \\ &\simeq\; \frac{2\pi}{\omega_0}\left(1 - \frac{3}{8}\beta x_0^2 + \frac{57}{256}\beta^2 x_0^4 + O\left(\beta^3 x_0^6\right)\right), \quad \text{for} \quad \beta x_0^2 \to 0. \qquad \text{(C.8)} \end{aligned}$$

Two representative solutions are shown in Fig. C.2. For solutions of this type, the average kinetic can be given in the same form as in Eq. (C.4), but the value of the corresponding constant $\mathscr{F}$ is different,

$$\mathscr{F} = \frac{4(1+\beta^*)}{3\beta^*}\left\{1 + \frac{\beta^*}{2} - \frac{E\left(\frac{\beta^*}{2(1+\beta^*)}\right)}{K\left(\frac{\beta^*}{2(1+\beta^*)}\right)}\right\}. \qquad \text{(C.9)}$$
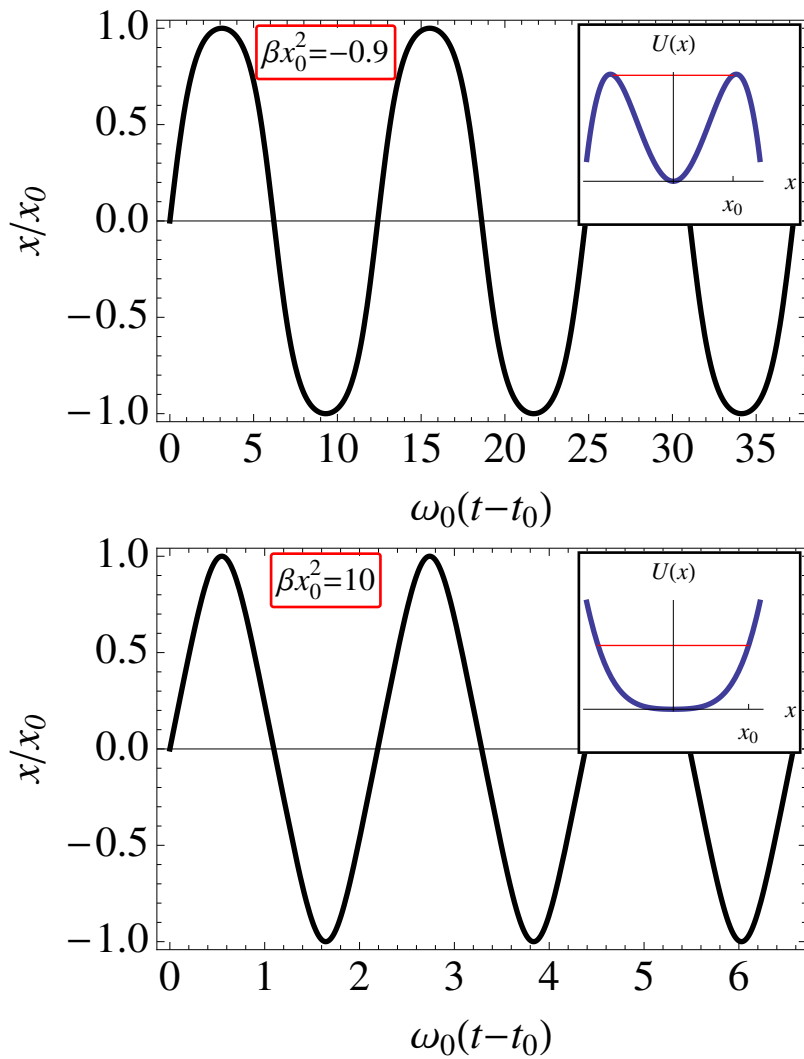
120

Figure C.2: Solutions to the equation of motion of the anharmonic oscillator with a quartic potential for two values of the coupling constant. The inserts show the corresponding shapes of the potentials.

APPENDIX D

DIRAC TRACES

This Appendix contains the results for Dirac traces used in the calculation of the current-current correlation function in Sec. 5.3.

There are two types of Dirac traces. The traces of first type are

$$\text{Tr}[\gamma^0 \mathscr{P}_{s_0,\sigma s_0} \gamma^0 \mathscr{P}_{s_0',\sigma' s_0'}] = \delta_{s_0}^{s_0'} \delta_{\sigma}^{\sigma'}, \tag{D.1}$$

$$\text{Tr}[\gamma^1 \mathscr{P}_{s_0,\sigma s_0} \gamma^1 \mathscr{P}_{s_0',\sigma' s_0'}] = -\delta_{s_0}^{-s_0'} \delta_{\sigma}^{\sigma'}, \tag{D.2}$$

$$\text{Tr}[\gamma^1 \mathscr{P}_{s_0,\sigma s_0} \gamma^2 \mathscr{P}_{s_0',\sigma' s_0'}] = i s_0 \sigma \delta_{s_0}^{-s_0'} \delta_{\sigma}^{\sigma'}, \tag{D.3}$$

$$\text{Tr}[\gamma^2 \mathscr{P}_{s_0,\sigma s_0} \gamma^2 \mathscr{P}_{s_0',\sigma' s_0'}] = -\delta_{s_0}^{-s_0'} \delta_{\sigma}^{\sigma'}, \tag{D.4}$$

The traces of the second type are

$$\text{Tr}[\gamma^0 \mathscr{P}_{s_0,\sigma s_0} (\mathbf{r} \cdot \boldsymbol{\gamma}) \gamma^0 \mathscr{P}_{s_0',\sigma' s_0'} (-\mathbf{r} \cdot \boldsymbol{\gamma})] = -(x^2 + y^2) \delta_{s_0}^{-s_0'} \delta_{\sigma}^{\sigma'}, \tag{D.5}$$

$$\text{Tr}[\gamma^1 \mathscr{P}_{s_0,\sigma s_0} (\mathbf{r} \cdot \boldsymbol{\gamma}) \gamma^1 \mathscr{P}_{s_0',\sigma' s_0'} (-\mathbf{r} \cdot \boldsymbol{\gamma})] = -\delta_{s_0}^{s_0'} \delta_{\sigma}^{\sigma'} [x^2 - y^2 - 2i s_0 \sigma (x^2 - y^2)],$$

$$\tag{D.6}$$

$$\text{Tr}[\gamma^1 \mathscr{P}_{s_0,\sigma s_0} (\mathbf{r} \cdot \boldsymbol{\gamma}) \gamma^2 \mathscr{P}_{s_0',\sigma' s_0'} (-\mathbf{r} \cdot \boldsymbol{\gamma})] = -\delta_{s_0}^{s_0'} \delta_{\sigma}^{\sigma'} [2xy + i s_0 \sigma (x^2 - y^2)], \tag{D.7}$$

$$\text{Tr}[\gamma^2 \mathscr{P}_{s_0,\sigma s_0} (\mathbf{r} \cdot \boldsymbol{\gamma}) \gamma^2 \mathscr{P}_{s_0',\sigma' s_0'} (-\mathbf{r} \cdot \boldsymbol{\gamma})] = \delta_{s_0}^{s_0'} \delta_{\sigma}^{\sigma'} (x^2 - y^2 - 2ixy s_0 \sigma). \tag{D.8}$$